

# Scanning Tunneling Microscopy using Superconducting Tips to Probe Absolute Spin Polarization

Thèse

Présentée à la Faculté Sciences de Base  
Laboratoire de Science à l'Échelle Nanométrique  
Programme Doctoral en Physique

École Polytechnique Fédérale de Lausanne

pour l'obtention du grade de Docteur ès Sciences

par

Matthias Eltschka

acceptée sur proposition du jury:

Prof. V. Savona, président du jury

Prof. K. Kern, directeur de thèse

PD Dr. A. Thomas, rapporteur

Prof. W. Wulfhchel, rapporteur

Prof. O. Yazyev, rapporteur



Suisse  
2015



# Acknowledgements

My PhD project at the Max Planck Institute for Solid State Research has been a wonderful experience and I would like to express my gratitude to all colleagues and friends who have made this thesis possible.

First and foremost, I would like to thank **Prof. Klaus Kern** for the exciting project and for his continuous support of my work. I deeply appreciate his guidance as well as for giving freedom for scientific exploration. I felt quite privileged to work on a system as unique as the mK-STM and enjoyed the modern laboratory facilities with exceptional equipment.

I would like to express my gratitude to **Prof. Vincenzo Savona** for chairing the PhD exam as well as to **Dr. Andy Thomas**, **Prof. Wulf Wulfhekkel** and **Prof. Oleg Yazyev** for reviewing my thesis.

I want to express very special thanks to **Dr. Markus Etzkorn** for his everyday guidance. I am very thankful for his physical and technical advice, for the many stimulating discussions of science and for his proofreading of this thesis. My PhD project has greatly benefited from his analytical and structured approach to scientific questions.

I also feel grateful to **Dr. Christian R. Ast** for his frequent advice ranging from fundamental physical questions to applied technical problems. I would especially like to thank him for his great help with various fitting routines, the numerical solution of the Usadel equation and also for proofreading this thesis.

I want to thank **Berthold Jäck** for the productive teamwork and friendly working atmosphere at the mK-STM. His high motivation for solving daily tasks in the lab and his fundamental interest in physical questions enabled the successful realization of many time-consuming experiments.

I would like to thank **Dr. Maximilian Assig** for his efforts in the construction process of the mK-STM and for his initial measurements with superconducting tips. His work paved the way for the experimental results presented in this thesis.

Thanks go to **Prof. Mikhail A. Skortsov** and **Oleg V. Kondrashov** for providing the theoretical description of the superconducting cones and the enlightening discussions about theoretical models.

Grateful acknowledgments go to **Dr. Thomas White** for his thorough proofreading and polishing of this work.

## Acknowledgements

---

Many thanks to my office mates **Dr. Carola Straßer, Dr. Steffen Kahle, Sven Aeschlimann** and **Trevor Clarke** for our tidy office and the productive atmosphere.

I would like to warmly thank all colleagues and friends at the Max Planck Institute, **Sabine Abb, Christian Dette, Dr. Tobias Herden, Alexander Kölker, Sebastian Koslowski, Dr. Sören Krotzky, Claudius Morchutt, Ivan Pentegov, Daniel Rosenblatt, Dr. Eike Oliver Schäfer-Nolte, Verena Schendel, Lukas Schlipf, Jacob Senkpiel, Andreas Topp** and **Benjamin Wurster**.

Very special thanks to **Dr. Jagadeesh S. Moodera, Dr. Karthik V. Raman** and **Sander Kamerbeek** for stimulating discussions and wonderful adventures in India.

I feel very grateful for the friendly technical support by **Peter Andler, Rafail Chaikovitch, Marko Memmler, Martin Siemers** and **Wolfgang Stiepany**, especially during the relocation of the mK-STM to the new laboratory building.

Thanks to our secretary **Sabine Birtel** for her friendly and reliable help with paperwork.

Last but not least, I wish to express my gratitude to my parents for their continuous support and for always encouraging my interest in physics.

# Abstract

The interplay of superconductivity and magnetism is investigated for systems with dimensions ranging from the mesoscopic to the atomic scale by scanning tunneling microscopy (STM) at millikelvin temperatures and by numerical calculations. Based on geometrically confined superconductors in magnetic fields, a novel STM approach is introduced to quantitatively probe the spin polarization of tunneling electrons.

In the first part of this work, the effects of magnetic fields and geometrical confinement are probed for superconducting vanadium STM tips. Due to the unique confinement ranging from the atomic to the mesoscopic scale, the superconducting properties of the STM tips vary considerably from their bulk counterparts. To analyze the experimentally determined magnetic field dependence of several V tips, the superconductivity is numerically calculated for modeled cone geometries with various opening angles. The numerical approach based on a one-dimensional Usadel equation leads to a direct correlation between the opening angle  $\alpha$  and the order of the superconducting phase transition. First order phase transitions occur when the opening angle is smaller than a critical value ( $\alpha < \alpha_c$ ), whilst larger opening angles ( $\alpha > \alpha_c$ ) result in second order phase transitions. The comparison of experimental findings and numerical results reveals the existence of first and second order quantum phase transitions in the V STM tips. In addition, the numerical calculations also explain experimentally observed broadening effects of the superconducting spectra by the specific tip geometry.

In the second part, the superconducting V tips are employed in a novel approach to quantitatively probe the spin polarization of tunneling electrons on the nanoscale. For this purpose, the Meservey-Tedrow-Fulde technique is transferred to STM in order to combine their virtues, such as the quantitative probing capability of the spin polarization, the precise control at the atomic scale and the well-defined vacuum tunnel barrier. To demonstrate the capabilities of the new technique, the local spin structure is resolved for a magnetic Co nanoisland, where spin polarizations ranging from -56 % up to 65 % were found, depending on the local position. Furthermore, the spin polarization  $P$  strongly varies with the tip-to-sample distance  $z$  ( $dP/dz \approx 10 \text{ \%}/\text{\AA}$ ), which is described by the different decays of the spin-up and spin-down wave functions into the vacuum tunnel barrier.

The final part describes the local interaction between isolated magnetic moments and the superconducting ground state. Copper phthalocyanine molecules on the superconducting V(100) surface induce bound states within the superconducting gap due to the magnetic coupling and the Coulomb potentials. Spatially resolved measurements reveal the non-isotropic structure of the spectral weights that is explained by the adsorption site on the  $5 \times 1$  recon-

## Acknowledgements

---

struction of the V(100) surface. The quasi-particle excitations are not only observed on the magnetic molecule but also occur in its close vicinity. With increasing distance from the molecular structure, the intensities of the bound states decay within the distance  $x \approx \pm 30 \text{ \AA}$  and show periodic oscillations at the same time. Comparing the experimental findings to a one-dimensional model suggests the presence of a complicated scattering potential, which can be simplified by assuming two point scatterers within the molecular structure.

The investigations presented in this thesis provide a better fundamental understanding of superconductivity in the presence of magnetic fields, enabling a novel approach for quantitatively probing the spin polarization in STM. Furthermore, the interplay of superconductivity with isolated magnetic moments is probed on the atomic scale and the distance dependence of the induced bound states indicates the spatial extension of the magnetic interaction.

### Keywords:

Scanning Tunneling Microscopy

Meservey-Tedrow-Fulde Technique

Spin-dependent Tunneling

Spin Polarization

Superconductivity in Confined Geometries

Superconducting Phase Transition in Magnetic Fields

Impurity Induced Bound States

Local Quasi-Particle Excitations

# Kurzfassung

Die vorliegende Arbeit studiert das Wechselspiel zwischen Supraleitung und Magnetismus mittels Rastertunnelmikroskopie und numerischer Berechnungen. Es werden Systeme untersucht, deren räumliche Ausdehnung von einigen wenigen Atomen bis hin zu mesoskopischen Größen reicht. Dabei wird ein neues Verfahren der Rastertunnelmikroskopie vorgestellt, welches auf räumlich eingegrenzten Supraleitern in magnetischen Feldern als Sonden zur quantitativen Messung der Spinpolarisation von tunnelnden Elektronen basiert.

Die Effekte räumlicher Eingrenzung und hoher Magnetfelder werden zunächst an supraleitenden Vanadiumspitzen für die Rastertunnelmikroskopie untersucht. Die supraleitenden Eigenschaften der Rastertunnelmikroskopiespitzen weichen aufgrund der besonderen Geometrie, welche den Supraleiter sowohl auf atomarer als auch auf mesoskopischer Längenskala räumlich begrenzt, erheblich von makroskopischen Proben ab. Zur Analyse der experimentell bestimmten Magnetfeldabhängigkeiten verschiedener, supraleitender Spitzen wird die Supraleitung für kegelförmige Modelle unterschiedlicher Öffnungswinkel numerisch berechnet. Basierend auf einer eindimensionalen Usadel Gleichung führt die numerische Berechnung zu einer direkten Beziehung zwischen dem Öffnungswinkel  $\alpha$  und der Ordnung des supraleitenden Phasenübergangs. Während für Öffnungswinkel unterhalb eines kritischen Wertes ( $\alpha < \alpha_c$ ) Phasenübergänge erster Ordnung auftreten, erzeugen größere Winkel ( $\alpha > \alpha_c$ ) Phasenübergänge zweiter Ordnung. Der Vergleich von experimentellen Befunden und numerischen Berechnungen bestätigt die Existenz von Phasenübergängen sowohl erster als auch zweiter Ordnung in den Vanadiumspitzen.

Zur Anwendung kommen die supraleitenden Vanadiumspitzen anschließend in einem neuen Verfahren zur quantitativen Bestimmung der Spinpolarisation von tunnelnden Elektronen mit atomarer räumlicher Auflösung. Mit dem Transfer der Meservey-Tedrow-Fulde Technik in die Rastertunnelmikroskopie werden die Vorzüge beider Verfahren kombiniert, welche quantitatives Messen der Spinpolarisation, präzise Kontrolle auf atomarer Skala und eine wohldefinierte Vakuumtunnelbarriere beinhalten. Zur Demonstration des Leistungsvermögens der neuen Messtechnik werden die lokalen Spinstrukturen einer magnetischen Nanostruktur aus Cobalt räumlich aufgelöst und, abhängig von der Messposition, Spinpolarisationen von -56 % bis 65 % nachgewiesen. Darüber hinaus zeigt die Spinpolarisation  $P$  eine signifikante Abhängigkeit von dem Abstand  $z$  zwischen Spitze und Probe ( $dP/dz \approx 10\%/Å$ ), welche sich durch das unterschiedliche Abklingen der Wellenfunktionen verschiedener Spinorientierungen in der Vakuumtunnelbarriere erklären lässt.

Abschließend wird die lokale Wechselwirkung zwischen einzelnen magnetischen Momenten

## Acknowledgements

---

und dem supraleitenden Grundzustand untersucht. Auf der Oberfläche eines supraleitenden V(100) Einkristalls induzieren einzelne Kupferphthalocyaninmoleküle gebundene Zustände, welche durch die lokale magnetische Kopplung und Coulomb-Potentiale innerhalb der supraleitenden Bandlücke entstehen. Messungen mittels Rastertunnelmikroskopie veranschaulichen die anisotrope Ausbreitung der induzierten Zustände in Folge des Adsorbierens auf der  $5 \times 1$  Rekonstruktion der V(100) Oberfläche. Die Anregungen von Quasiteilchenzuständen beschränken sich jedoch nicht nur auf die räumliche Ausdehnung der molekularen Strukturen, sondern lassen sich auch in deren unmittelbarer Umgebung nachweisen. Mit zunehmender Distanz  $x \approx \pm 30 \text{ \AA}$  von den Molekülen verschwindet die spektrale Intensität der induzierten Zustände, wobei während des Abklingvorgangs noch zusätzliche Oszillationen zu beobachten sind. Im Vergleich mit einem eindimensionalen Modell finden sich Hinweise auf die Existenz eines komplexen Streupotentials, welches sich in einer vereinfachten Betrachtung mittels zweier punktförmiger magnetischer Momente innerhalb eines einzelnen Moleküls beschreiben lässt.

Die hier präsentierten Studien verbessern das Grundlagenverständnis von Supraleitung in Gegenwart von magnetischen Feldern und ermöglichen ein neues Messverfahren in der Rastertunnelmikroskopie zur quantitativen Bestimmung der Spinpolarisation. Die Untersuchung der Wechselwirkung zwischen Supraleitung und einzelnen magnetischen Momenten zeigt die räumliche Ausdehnung der magnetischen Kopplung.

### Schlagwörter:

Rastertunnelmikroskopie  
Meservey-Tedrow-Fulde Technik  
Spinabhängiges Tunneln  
Spinpolarisation  
Supraleitung in räumlich begrenzten Geometrien  
Supraleitender Phasenübergang in Magnetfeldern  
Störstelleninduzierte gebundene Zustände  
Lokale Quasiteilchen Anregungen



# Contents

<b>Acknowledgements</b>	<b>iii</b>
<b>Abstract (English / Deutsch)</b>	<b>v</b>
<b>List of figures</b>	<b>xiii</b>
<b>1 Introduction</b>	<b>1</b>
<b>2 Theoretical Background</b>	<b>5</b>
2.1 Superconductivity . . . . .	5
2.1.1 Superconducting Phenomena . . . . .	6
2.1.2 Bardeen-Cooper-Schrieffer Theory . . . . .	9
2.1.3 Characteristic Superconducting Parameters . . . . .	13
2.1.4 Superconducting Phase Transition in Magnetic Field . . . . .	15
2.1.5 First and Second Order Phase Transitions . . . . .	18
2.1.6 Maki Model . . . . .	22
2.1.7 Usadel Equations . . . . .	23
2.2 Magnetism and Spin-dependent Transport . . . . .	24
2.2.1 Magnetic Energies . . . . .	24
2.2.2 Spin Polarization . . . . .	26
2.2.3 Spin-dependent Transport . . . . .	27
2.3 Local Spin Moments Interacting with Superconductors . . . . .	28
2.3.1 Magnetic Impurity-induced Bound States in Superconductors . . . . .	29
2.3.2 Spatial Distribution of Quasi-particle Bound States . . . . .	31
<b>3 Experimental Techniques</b>	<b>33</b>
3.1 Scanning Tunneling Microscopy . . . . .	33
3.1.1 Working Principle . . . . .	33
3.1.2 Theoretical Description of Electron Tunneling . . . . .	35
3.1.3 Scanning Tunneling Spectroscopy . . . . .	38
3.2 Millikelvin Scanning Tunneling Microscope . . . . .	39
3.2.1 Overview of the System . . . . .	39
3.2.2 STM Unit . . . . .	41
3.2.3 Dilution Refrigeration . . . . .	42

## Contents

---

3.2.4	Energy Resolution . . . . .	42
3.3	Meservey-Tedrow-Fulde Technique . . . . .	44
3.3.1	Spin-dependent Tunneling . . . . .	44
3.3.2	Extended Maki Model . . . . .	47
<b>4</b>	<b>Geometrically Confined Superconductors in Magnetic Fields</b>	<b>51</b>
4.1	Overview and Motivation . . . . .	51
4.2	Magnetic Field Dependence of Vanadium STM Tips . . . . .	52
4.3	Usadel Equation for Superconducting Cones in Magnetic Fields . . . . .	60
4.4	Magnetic Field Dependence of Superconducting Cones . . . . .	61
4.5	Order of the Superconducting Phase Transition . . . . .	66
<b>5</b>	<b>Probing Absolute Spin Polarization at the Nanoscale</b>	<b>71</b>
5.1	Overview and Motivation . . . . .	71
5.2	Cobalt Nanoislands on Copper . . . . .	72
5.3	Meservey-Tedrow-Fulde Scanning Tunneling Microscopy . . . . .	73
5.4	Spin-filtering by Vacuum . . . . .	82
5.5	Alternatives for Probing Spin Polarization at the Nanoscale . . . . .	88
<b>6</b>	<b>Probing Local Magnetic Moments Interacting with a Superconductor</b>	<b>93</b>
6.1	Overview and Motivation . . . . .	93
6.2	Copper Phthalocyanine on V(100) . . . . .	94
6.3	Observation of Local Bound States . . . . .	96
6.4	Spatial Distribution of Locally Induced Bound States . . . . .	97
6.5	Distance Dependence of Bound States . . . . .	99
<b>7</b>	<b>Summary and Outlook</b>	<b>107</b>
7.1	Geometrically Confined Superconductors in Magnetic Fields . . . . .	107
7.2	Probing Absolute Spin Polarization at the Nanoscale . . . . .	108
7.3	Probing Local Magnetic Moments Interacting with a Superconductor . . . . .	110
	<b>Bibliography</b>	<b>120</b>
	<b>Curriculum Vitae</b>	<b>121</b>
	<b>List of Publications</b>	<b>123</b>

# List of Figures

2.1	Expulsion of magnetic fields from superconductors by the Meissner effect . . .	7
2.2	Formation of Cooper pairs due to an attractive interaction between electrons .	10
2.3	The superconducting quasi-particle DOS derived by BCS theory . . . . .	12
2.4	Phase diagrams for type I and type II superconductors . . . . .	16
2.5	Magnetic flux penetration in type I and type II superconductors . . . . .	17
2.6	Order of the phase transition and thermodynamic potential . . . . .	19
2.7	Superconducting gap of thin Al films as a function of external magnetic field . .	21
2.8	The magnetic field dependence of thin Al films . . . . .	21
2.9	Schematic of the spin alignment due to magnetic interactions . . . . .	25
2.10	The spin-polarized DOS for free electrons in an external magnetic field (Pauli paramagnetism) . . . . .	27
2.11	Schematic for spin-dependent transport . . . . .	28
2.12	Energies and spectral weights of quasi-particle bound states for exchange inter- action . . . . .	30
2.13	Energies and spectral weights of quasi-particle bound states for Coulomb inter- action . . . . .	31
3.1	Schematic of the STM working principle . . . . .	34
3.2	Schematic of quantum tunneling in a 1D potential barrier . . . . .	36
3.3	Probing the electronic properties by scanning tunneling spectroscopy . . . . .	37
3.4	Design of the mK-STM . . . . .	40
3.5	Design of the STM unit . . . . .	41
3.6	The dilution refrigerator of the mK-STM . . . . .	43
3.7	Differential conductance measured between a superconducting Al tip and a Cu(111) surface . . . . .	44
3.8	Origin of the differential conductance spectra used in the MTF technique . . . .	45
3.9	Differential conductance spectra calculated by the Maki model to demonstrate depairing and spin-orbit scattering . . . . .	48
3.10	Differential conductance spectra calculated by the Maki model to demonstrate the influence of the broadening parameter and temperature . . . . .	49
4.1	Magnetic field dependence of superconducting V tip with sharp spectral features	52
4.2	Comparison between experimental data and several fit models . . . . .	53

## List of Figures

---

4.3	Magnetic field dependence of superconducting V tip with broadened spectral features . . . . .	54
4.4	Superconducting gaps and Zeeman splitting of V tips . . . . .	55
4.5	The reduced parameter $\tilde{\Gamma} = \Gamma/\Delta$ for spectral broadening . . . . .	56
4.6	Magnetic field dependence for the spin-orbit scattering $b$ and the orbital depairing $\zeta$ . . . . .	57
4.7	Continuous measurement of the differential conductance while ramping the magnetic field . . . . .	58
4.8	Differential conductance spectra and Maki fits for the dynamic measurement method . . . . .	59
4.9	Comparison of zero-bias differential conductance and the superconducting gap	60
4.10	Numerical precision of the Usadel approach . . . . .	62
4.11	Calculated superconductivity of cones with opening angle $\alpha$ in an external magnetic field . . . . .	63
4.12	Superconducting quasi-particle DOS of a sharp tip ( $\alpha/\alpha_c = 0.4$ ) . . . . .	64
4.13	Superconducting quasi-particle DOS of a blunt tip ( $\alpha/\alpha_c = 3.2$ ) . . . . .	64
4.14	Superconducting gaps extracted by the extended Maki Model fit from the Usadel spectra . . . . .	65
4.15	Broadening parameters extracted by the extended Maki Model fit from the Usadel spectra . . . . .	65
4.16	Comparison of the superconducting gaps obtained by the Usadel calculations and the Maki fits . . . . .	66
4.17	The extended Maki model as a link between Usadel calculations and experimental results . . . . .	67
4.18	Comparison of the Usadel calculations and the experimentally obtained superconducting gaps . . . . .	68
4.19	Comparison of the Usadel calculations and the experimentally obtained broadening parameters . . . . .	68
5.1	STM image of Co nanoislands on Cu(111) . . . . .	72
5.2	$dI/dV$ spectra measured on the center region of a Co nanoisland with a superconducting V tip . . . . .	74
5.3	$dI/dV$ spectra measured on the bare Cu surface . . . . .	74
5.4	Superconducting gaps and Zeeman splitting of a V tip measured on a Co nanoisland and on the Cu(111) surface . . . . .	76
5.5	Contributions of spin-up and spin-down electrons to the tunnel current . . . . .	77
5.6	$dI/dV$ spectra obtained on Cu and Co for larger voltage ranges . . . . .	78
5.7	Probing absolute values of spin polarization at the nanoscale . . . . .	79
5.8	Error estimation for the fitting routine performed by varying the superconducting gap . . . . .	80
5.9	Error estimation for the fitting routine performed by varying the broadening parameter . . . . .	80

5.10 Resulting spin polarization when varying the superconducting gap or the broadening parameter . . . . .	82
5.11 Schematic illustrations of the basic influences on the spin polarization of tunneling electrons . . . . .	83
5.12 Differential conductance measured at two different tip-to-sample distances on a Co island . . . . .	84
5.13 Distance dependence of the spin polarization of tunneling electrons . . . . .	84
5.14 1D model for the distance dependence of the spin polarization . . . . .	85
5.15 Alternative 1D model for distance dependence of the spin polarization . . . . .	86
5.16 Distance dependence of the tunnel current . . . . .	87
6.1 CuPc on the $5 \times 1$ reconstruction of the V(100) surface . . . . .	95
6.2 $dI/dV$ spectra measured on three different positions of a CuPc molecule . . . . .	96
6.3 Locally resolved bound states observed on an isolated CuPc molecule and its close surroundings . . . . .	98
6.4 Differential conductance measurements for the distance dependence of the quasi-particle excitations . . . . .	100
6.5 Spatially resolved distance dependence of the energies for impurity induced bound states . . . . .	102
6.6 Spatially resolved distance dependence of the intensities for impurity induced bound states . . . . .	103
6.7 Distance dependence of quasi-particle excitations modeled by two magnetic impurities ( $V > 0$ ) . . . . .	104
6.8 Distance dependence of quasi-particle excitations modeled by two magnetic impurities ( $V < 0$ ) . . . . .	104



# 1 Introduction

Superconductivity and magnetism are often considered as competing phenomena arising from different interactions of electrons on the microscopic scale. In this context, the electron spin plays an important role with its intrinsic angular momentum as an additional degree of freedom. In conventional superconductors, electrons form so-called Cooper pairs with opposing spin moments at low temperature [1, 2]. Since these Cooper pairs move through superconducting materials without any electric resistance, superconductors provide great potential for energy efficient applications, for example, in the generation and distribution of electric power. The attractive force of the pairing mechanism stems from the electron interaction with phonons of the crystal lattice and, as a result, the coupling is long ranged up to the order of several micrometers [3]. Since the total spin of Cooper pairs is an integer and, hence, of bosonic character, the resulting superconducting ground state greatly differs from the normal conducting phase. In magnetic materials, by contrast, the electrons as fermions obey the Pauli exclusion principle. It is directly related to the ferromagnetic exchange interaction, which is normally short-ranged between neighboring atoms. Here, the electron spins align in the same direction in order to produce a total net magnetization. Magnetic materials are also important in a wide field of applications ranging from electromobility to sensing and logic devices.

The opposing character of superconductivity and magnetism becomes obvious when a magnetic field is applied to a superconductor. In high fields, the superconducting phase ceases to exist and the superconductor undergoes a phase transition to the normal conducting state. Studying the phase transition not only provides a better understanding of the fundamental superconducting processes, e. g. the underlying pairing mechanism of the Cooper pairs, but is also essential for modern applications, such as the superconducting magnets used for the Large Hadron Collider at CERN. In weaker magnetic fields below the phase transition, the complex interplay of superconductivity and magnetism can already manifest in the so-called Meissner phase. Here, the magnetic field only penetrates a small portion of the superconductor, which expels the field from its interior with the majority of the Cooper pairs remaining in field free conditions [4, 5]. In this context, the geometry of the superconductor represents an essential factor, which can directly change the amount of affected Cooper pairs and, thus, can

greatly alter the behavior of superconductors in magnetic fields. The effects of geometrical confinement have extensively been studied on superconducting thin films. To this end, tunneling experiments have been carried out on planar tunnel junctions, where the superconducting films and a metal counter electrode are separated by an isolating tunnel barrier [6–9]. These studies have revealed the unique properties of geometrically confined superconductors, in which the majority of the Cooper pairs are exposed to the magnetic field. More importantly, R. Meservey, P. M. Tedrow and P. Fulde demonstrated in their pioneering work that thin film superconductors can be employed in a detection scheme to measure the spin orientation of electrons [6–10]. Over the years, the Meservey-Tedrow-Fulde (MTF) technique has emerged as a well-established standard for probing the spin polarization of tunneling conduction electrons in various magnetic materials and compounds [8–10]. In fact, their spin-dependent tunneling experiments based on geometrically confined superconductors laid the foundation for a new field of research aimed at the control of the electron spin as an additional degree of freedom. However, it became clear in later years that spin transport already responds to variations on the atomic scale and, thus, the lack of local resolution in planar tunnel junctions poses a major limitation. Whereas tunneling experiments with atomic scale resolution are feasible in scanning tunneling microscopy (STM), it has not been successfully combined with the spin-polarized MTF technique, so far. Besides technical aspects, the main physical question arises from the superconducting geometry required for STM, which considerably differs from the thin films usually employed in the MTF approach, or as R. Meservey put it [10]: *“What is the best way to apply the techniques of spin-polarized electron tunneling to scanning tunneling microscopy? The answer is not clear at this time (...).”*

In contrast to magnetic fields, which usually effect a large number of Cooper pairs in conventional superconductors, isolated magnetic impurities only act as local perturbations to the superconducting state. While frequently regarded as distracting obstacles, single impurities can reveal elemental physical mechanisms of the system under investigation, which are not accessible in perfectly pure bulk materials [11]. Moreover, impurities play an important role in many applications, for example as dopants in the semiconductor electronics industry. For superconductors, single magnetic moments are employed as experimental probes on the atomic scale. As a result, the superconducting order parameter is locally reduced and leads to excitations within the superconducting state [11–14]. The states created by impurities reveal the underlying physics and the origin of the superconducting phase [11]. In this context, STM represents an important tool for experimentally resolving the electronic structure on the atomic scale in close vicinity of the impurities [11, 15–18].

This thesis starts with a brief theoretical introduction to superconductivity and magnetism in Chap. 2. The interaction of superconductivity with external magnetic fields is described by a phenomenological approach and the main concepts are presented for a microscopic description. A short overview of the fundamental properties of magnetic systems and spin-dependent transport is followed by a description of the local effects of isolated magnetic impurities on superconducting surfaces. In Chap. 3, the basic concepts are explained for the experimental techniques used in this thesis, namely STM and the MTF technique. The scientific results



---

are discussed from Chap. 4 to Chap. 6. Starting with Chap. 4, the influence of geometrical confinement on superconductivity in the presence of magnetic fields is investigated by STM. The main focus lies on the experimental and theoretical investigation of the superconducting phase transition in magnetic fields. In Chap. 5, the results achieved in the previous chapter are applied in a novel approach for quantitatively probing the spin polarization at the nanoscale. Chap. 6 deals with the interaction of superconductivity and magnetism on the atomic scale. Here, the local excitations of the superconducting quasi-particle density of states (DOS) induced by isolated magnetic moments are probed by STM.



## 2 Theoretical Background

This chapter introduces the theoretical background required to analyze and understand the experimental results presented in Chap. 4-6. In the first part, the interaction of superconductivity with external magnetic fields is discussed by a phenomenological approach, which is later justified in the framework of a microscopic theory. The second part deals with the basic properties of magnetic system as well as a brief introduction into spin-dependent transport. In the third part of the chapter, the local effects of isolated magnetic impurities on superconductivity are discussed with respect to the resulting spectral properties for experimental investigations.

### 2.1 Superconductivity

In 1911, superconductivity was discovered by H. K. Onnes at Leiden university [19]. He observed that the electrical resistance of mercury vanished below a characteristic critical temperature. The foundations for his great discovery were laid three years earlier, when he liquefied helium for the first time and was able to achieve temperatures close to 1.5 K [20]. For his work, H. K. Onnes received the Physics Nobel Prize in 1913.

While the great potential of superconductors was immediately recognized, for example in applications generating or distributing electric power, deriving a fundamental understanding of superconductivity has been an ongoing challenge for more than one hundred years. In 1935, the brothers F. and H. London developed the London equations, providing a phenomenological description of the electrodynamics in superconductors [5]. The first commonly accepted microscopic theory about superconductivity was presented by J. Bardeen, L. Cooper, and J. Schrieffer in 1957 — almost half a century after the first experimental observation [2]. Their so-called BCS theory describes the superconducting state by the formation of Cooper pairs due to an attractive interaction between two electrons. It correctly predicts experimental observations such as the characteristic critical temperatures and the superconducting gap at the Fermi level. Over the years, BCS theory has been extended by various modifications, considerably increasing its range of applications. For example, Maki's model adds spin-flip

scattering of Cooper pairs on magnetic impurities and the Usadel approach describes diffusive transport in systems where elastic scattering is dominant.

In this work, superconducting vanadium plays an important role. Since it belongs to the conventional superconductors, its properties are well-described by the London equations and BCS theory. While a complete discussion goes beyond the scope of this thesis, the detailed theories are the subject of many modern textbooks [21–23]. This section represents a summary of Refs 21, 22, 24 focusing on the relevant topics for the experimental results (Chap. 4-6).

### 2.1.1 Superconducting Phenomena

The first characteristic phenomenon of superconductivity is the perfect electric conductivity, which was already described by H. K. Onnes [19]. For example, when cooled down below the critical temperature  $T_c$ , persistent currents in superconducting rings have been demonstrated to flow without any external power source for more than a year without any measurable decrease [22].  $T_c$  marks the transition from the normal conducting to the superconducting phase and depends on the material. It is rather low for conventional superconductors, such as aluminum  $T_c(\text{Al}) = 1.18 \text{ K}$  [25] or vanadium  $T_c(\text{V}) = 5.43 \text{ K}$  [26], and increases for high  $T_c$  superconductors, for which values up to 133 K have been reported [27].

The second characteristic of superconductors is their perfect diamagnetism. In 1933, W. Meißner and R. Ochsenfeld described the expulsion of a magnetic field from a superconductor, later called the Meissner effect [4]. They investigated superconducting cylinders in external magnetic fields and observed that the field distribution around the superconductor resembled an ideal diamagnet with susceptibility  $\chi = -1$ . More importantly, this effect is also observed even when a superconductor is first brought into a magnetic field and then cooled down below  $T_c$ . In Fig. 2.1(a), a metallic sample in an external magnetic field is schematically shown for the normal conducting state at  $T > T_c$ . The magnetic field penetrating the sample is almost unchanged except for small negligible paramagnetic effects. After cooling the sample below  $T_c$ , the magnetic field is excluded from the superconducting material as shown in Fig. 2.1(b). While the exclusion of the magnetic field from the superconductor could also be attributed to the perfect conductivity, the expulsion below  $T_c$  is an unique effect of superconductivity. It contradicts the behavior of a perfect conductor, which would trap in the magnetic flux.

The two most important phenomena of a superconductor — perfect conductivity and perfect diamagnetism — are described by the London equations [5]. They phenomenologically express the response of a superconductor to external electromagnetic fields [21]:

$$\frac{\partial \mathbf{j}}{\partial t} = \frac{nq^2}{m} \mathbf{E}, \quad (2.1)$$

$$\nabla \times \mathbf{j} = -\frac{nq^2}{m} \mathbf{B}, \quad (2.2)$$

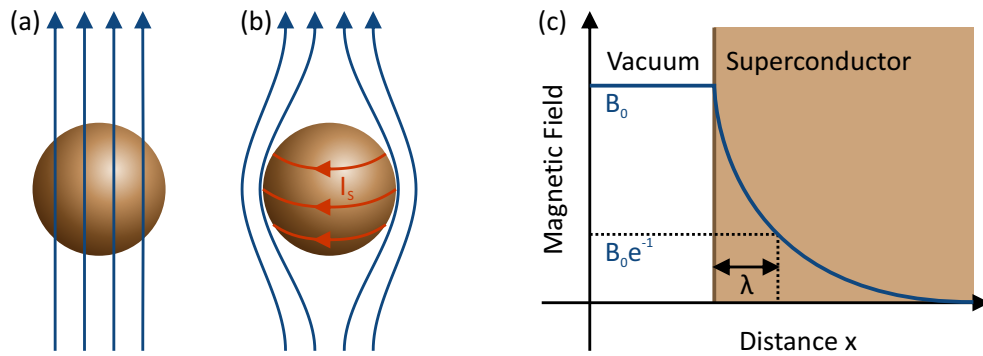


Figure 2.1: Expulsion of magnetic fields from superconductors by the Meissner effect. (a) For  $T > T_c$ , the normal conducting metal is penetrated by the external magnetic field, which is only slightly effected by small paramagnetic effects. (b) For  $T < T_c$ , the superconducting metal expels the magnetic field. The field free condition is realized by the formation of shielding currents  $I_s$ . (c) The expulsion of the magnetic field from a superconductor is calculated by the second London equation. The magnetic field decays exponentially within the superconducting bulk, where the decay is given by the London penetration depth  $\lambda$ .

where  $\mathbf{j}$  is the superconducting current density,  $\mathbf{B}$  and  $\mathbf{E}$  are the magnetic and the electric field, respectively.  $m$  represents the electron mass and  $n$  is the density of the charge carriers with the charge  $q$ . The first London equation (Eq. 2.1) is derived for non-dissipative transport, in which the charge carriers are continuously accelerated by an electric field.<sup>1</sup> Thus, this equation replaces Ohm's law and describes perfect conductivity for superconductors.

The second London equation (Eq. 2.2) provides a phenomenological description for the behavior of superconductors in magnetic fields.<sup>2</sup> It is transformed by the Maxwell equation

<sup>1</sup> In Sec. 2.1.3, the first London equation is derived from the microscopic BCS theory. A simpler approach starts from Newton's second law in the form

$$\mathbf{F} = m \frac{\partial \mathbf{v}}{\partial t}$$

with the force  $\mathbf{F} = q\mathbf{E}$  on a particle with mass  $m$  and charge  $q$  in the electric field  $\mathbf{E}$ . In combination with the current density

$$\mathbf{j} = nq\mathbf{v}$$

the first London equation (Eq. 2.1) is obtained with the density of charge carriers  $n$ . However, the detailed correlation of  $n$  and the density of Cooper pairs formed in a superconductor is only obtained from the BCS approach.

<sup>2</sup>The second London equation (Eq. 2.2) is also derived from BCS theory in Sec. 2.1.3. For now, Faraday's law is applied on the curl of first London equation leading to:

$$\frac{\partial}{\partial t} \left( \nabla \times \mathbf{j} + \frac{nq^2}{m} \mathbf{B} \right) = 0.$$

This equation is solved by constant as well as exponentially decaying functions for  $\mathbf{j}$  and  $\mathbf{B}$ . The phenomenological London approach neglects the constant solution, which is justified by BCS theory (Sec. 2.1.3).

$\nabla \times \mathbf{B} = \mu_0 \mathbf{j}$  (with the vacuum permeability  $\mu_0$ ) that leads to the differential equation

$$\nabla^2 \times \mathbf{B} = \frac{1}{\lambda^2} \mathbf{B}. \quad (2.3)$$

Since the solution yields an exponential decay of the magnetic field in the superconductor, Eq. 2.3 represents the electrodynamic description of the Meissner effect. In Fig. 2.1(c), the simple case of a semi-infinite superconductor is shown for a homogeneous magnetic field  $\mathbf{B} = (0, 0, B_0)$  pointing parallel to the superconducting surface into  $z$ -direction (Fig. 2.1(c)). For this geometry, the solution of Eq. 2.3 reads

$$B_z(x) = B_0 e^{-x/\lambda}, \quad (2.4)$$

where  $x$  points perpendicular from the surface towards the interior of the superconductor (Fig. 2.1(c)). Due to the special geometry, the magnetic field is not effected outside the superconductor. From its surface, the magnetic field exponentially decays due to the formation of shielding currents within the bulk of the superconductor. The decay length is called the London penetration depth  $\lambda$ , which is given by

$$\lambda = \sqrt{\frac{m}{\mu_0 n q^2}}. \quad (2.5)$$

For most superconducting materials,  $\lambda$  is in the order of 100 nm, for example  $\lambda(\text{Al}) = 45$  nm [25] and  $\lambda(\text{V}) = 267$  nm [28]. In addition,  $\lambda$  is found to show a strong temperature dependence, which is empirically described by  $\lambda(T) \approx \lambda(0) (1 - (T/T_c)^4)^{-1/2}$  [22].

The suppression of the magnetic field is microscopically explained by the formation of shielding currents. In the small region given by  $\lambda$ , these shielding currents compensate for the external magnetic field, so that the interior of the superconductor remains field free (Fig. 2.1(b)). For the geometry shown in Fig. 2.1(c), the shielding current density  $j_y$  is given by

$$j_y(x) = \frac{B_0}{\mu_0 \lambda} e^{-x/\lambda}. \quad (2.6)$$

The shielding currents flow perpendicular to the external magnetic field in the thin surface layer defined by  $\lambda$ . They induce the reverse magnetization to compensate the external field, which, as a result, is completely ejected from the superconductor. The exponential decay of the magnetic field suppression also weakens the perfect diamagnetism attributed to superconductors. While the argument still holds true for bulk superconductors, the behavior for geometrically confined superconductors may be different when at least one dimension becomes similar to the London penetration depth. However, understanding such systems in detail requires a more fundamental description for the microscopic origin of superconductivity.

### 2.1.2 Bardeen-Cooper-Schrieffer Theory

Introduced in 1957, the BCS theory [2] represents the first microscopic description and “revolutionized the quality of our understanding of superconductivity” [22]. It not only provides the capability to calculate phenomenological parameters such as the London penetration depth, but also explains the origin of superconducting phenomena such as the energy gap at zero-bias or the coherence length. The basic concept is that electrons are bound to each other by an attractive interaction. The new bound state is energetically favored and forms the superconducting phase, as demonstrated below. The approach shown here follows the presentation in Ref. 21.

The fundamental mechanism presented by J. Cooper in 1956 [1] describes the formation of the superconducting energy state. At zero-temperature, the ground state is the Fermi sea, where electrons are non-interacting except for Pauli’s exclusion principle.<sup>3</sup> All electron states are occupied for energies  $E \leq E_F = \hbar^2 k_F^2 / (2m)$  with the reduced Planck constant  $\hbar$ , the Fermi energy  $E_F$ , the Fermi wave vector  $k_F$  and the electron mass  $m$ . Two extra electrons are added to this system, where they can interact with each other but not with other electrons in the Fermi sea (except for Pauli’s principle). This interaction is described by elastic scattering processes, where the two additional electrons maintain their total momentum

$$\mathbf{k}_1 + \mathbf{k}_2 = \mathbf{k}'_1 + \mathbf{k}'_2 = \mathbf{K}. \quad (2.7)$$

As the underlying mechanism for the attractive electron interaction, H. Fröhlich in 1950 had already suggested electron-phonon scattering [3]. In a simplified picture, the first electron interacts with the positively charged ions of the medium due to the Coulomb force. The polarized lattice forms an attractive potential for the second electron so that the two electrons are effectively coupled by a weak attractive interaction. Compared to normal scattering processes in the electron transport, this indirect phonon coupling represents a much weaker interaction of second order. When moving through the potential landscape formed by the atomic ions, the electrons continuously emit and absorb phonons which keeps the two extra electrons coupled. Due to the conservation of energy, the phonons only exist for a short time, which is limited by the uncertainty relation  $\tau \leq 2\pi/\omega$ . In  $k$ -space, the interaction is limited by the Debye energy  $E_D = \hbar\omega_D$  with the Debye frequency  $\omega_D$ , which is the theoretical upper limit for lattice vibrations in this model. The amount of electron-phonon interaction processes reaches its maximum for  $\mathbf{K} = 0$ , which means  $\mathbf{k}_1 = -\mathbf{k}_2 = \mathbf{k}$  opposite wave vectors for the two coupled electrons (Fig. 2.2).

The two-body system is described by the Schrödinger equation for the interaction potential  $V(\mathbf{r}_1, \mathbf{r}_2)$  [21]:

$$-\frac{\hbar^2}{2m} (\Delta_1 + \Delta_2) \psi(\mathbf{r}_1, \mathbf{r}_2) + V(\mathbf{r}_1, \mathbf{r}_2) \psi(\mathbf{r}_1, \mathbf{r}_2) = E\psi(\mathbf{r}_1, \mathbf{r}_2), \quad (2.8)$$

<sup>3</sup>Pauli’s exclusion principle states that two identical fermions cannot have identical quantum numbers. As a result, the many-body wave function is anti-symmetric with respect to exchanging two of the electrons.

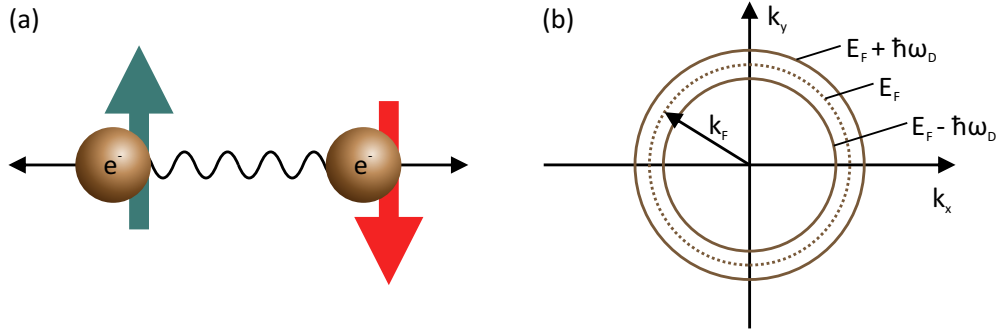


Figure 2.2: Formation of Cooper pairs due to an attractive interaction between electrons. The figure is based on Ref. 21. (a) Cooper pairs consist of two electrons with opposite momentum and spin orientation. (b) In the simplest case, the attractive interaction between the two electrons is considered constant for the energy range  $E_F - \hbar\omega_D < \frac{\hbar^2 k^2}{2m} < E_F + \hbar\omega_D$ .

where  $E = \epsilon + 2E_F$ . Due to their interaction, the two extra electrons possess the energy  $\epsilon$  compared to the non-interactive state with  $E = E_F$ . The resulting wave function  $\psi$  for interacting electrons is given by

$$\psi(\mathbf{r}_1 - \mathbf{r}_2) = \frac{1}{L^3} \sum_{\mathbf{k}} g(\mathbf{k}) e^{i\mathbf{k}(\mathbf{r}_1 - \mathbf{r}_2)}. \quad (2.9)$$

In this formalism, the relative coordinate  $\mathbf{r} = \mathbf{r}_1 - \mathbf{r}_2$  replaces the single electron coordinates.  $|g(\mathbf{k})|$  is the probability to find the electron pair at  $(\mathbf{k}, -\mathbf{k})$  which means that the first electron is in  $\mathbf{k}_1$  and the second electron is in  $\mathbf{k}_2$ . Due to the Debye limit of the interaction energy and due to Pauli's principle, the probability to find such a pair of electrons is expressed by  $g(\mathbf{k}) = 0$  for  $k < k_F$  and  $g(\mathbf{k}) = 0$  for  $k > \sqrt{2m(E_F + \hbar\omega_D) / \hbar^2}$ . For simplicity, the spin orientation of the electron states is not included in the Schrödinger equation or in the wave function (Eq. 2.8 and Eq. 2.9). According to the Pauli principle, the total wave function for the two electrons is anti-symmetric with respect to exchanging the particles. The electrons forming the Cooper pair have not only opposite momentum but also opposite spins ( $\mathbf{k} \uparrow, -\mathbf{k} \downarrow$ ). Therefore, the electrons in Eq. 2.9 form a singlet state. In general, triplet states can result from more complex electron-electron interactions, which are not considered in this simplified model.

The Schrödinger equation (Eq. 2.8) is solved by the planar wave expansion for the many-body problem (Eq. 2.9) as demonstrated in Ref. 21. The resulting equation for  $\epsilon$  yields the following expression:

$$\epsilon = \frac{2\hbar\omega_D}{1 - \exp[4 / (V_0 \rho(E_F))]}, \quad (2.10)$$

where  $V_0$  are the interaction matrix elements for electron scattering and  $\rho(E_F)$  represents the DOS at the Fermi level. Due to the indirect coupling mechanism by phonons, the attractive electron interaction is only weak ( $V_0 \rho(E_F) / 2 \ll 1$ ). In this weak coupling limit, Eq. 2.10



becomes

$$\epsilon \approx -2\hbar\omega_D \exp[-4/(V_0\rho(E_F))] . \quad (2.11)$$

Therefore, the attractive interaction between the two extra electrons results in a bound state whose energy is lowered by  $\epsilon = E - 2E_F < 0$ . In the superconducting regime, the Fermi sea of non-interacting electrons becomes unstable and a new ground state exists. While the interaction is only discussed between two electrons for simplicity, in reality, the majority of electrons form Cooper pairs. Since Cooper pairs consist of two electrons whose opposite spin moments compensate each other, they follow, in a good approximation, bosonic behavior. This means that the Pauli principle does not apply and all Cooper pairs occupy the same BCS ground state. The resulting new state represents the microscopic origin of superconductivity.

However, for real systems, the total energy of the new ground state is not simply the sum of the separate contributions from all Cooper pairs because the interaction between all electrons has to be considered. In the second quantization, the interaction between the electrons is expressed by the annihilation of the Cooper pair with  $(\mathbf{k} \uparrow, -\mathbf{k} \downarrow)$  and the creation of the Cooper pair with  $(\mathbf{k}' \uparrow, -\mathbf{k}' \downarrow)$ . The many-body wave function is given by [21]:

$$|\phi_{\text{BCS}}\rangle \cong \prod_{\mathbf{k}} (u_{\mathbf{k}}|0\rangle_{\mathbf{k}} + v_{\mathbf{k}}|1\rangle_{\mathbf{k}}) . \quad (2.12)$$

Here, the scattering process is expressed by the two orthogonal states  $|0\rangle_{\mathbf{k}}$  and  $|1\rangle_{\mathbf{k}}$ . In this notation,  $|0\rangle_{\mathbf{k}}$  means that the state  $(\mathbf{k} \uparrow, -\mathbf{k} \downarrow)$  is unoccupied and, accordingly,  $|1\rangle_{\mathbf{k}}$  is the occupied state.  $w_k = v_k^2$  gives the probability that the state is occupied whereas  $1 - w_k = u_k^2$  is the probability that it is unoccupied.

As demonstrated in Ref. 21, the total energy of the many-body system consists of the kinetic energy ( $E_{\text{kin}} = 2\sum_{\mathbf{k}} w_{\mathbf{k}}\xi_{\mathbf{k}}$ ) and the interaction potential:

$$E_{\text{BCS}} = 2\sum_{\mathbf{k}} v_{\mathbf{k}}^2 \xi_{\mathbf{k}} - \frac{V_0}{L^3} \sum_{\mathbf{k}\mathbf{k}'} v_{\mathbf{k}} u_{\mathbf{k}} v_{\mathbf{k}'} u_{\mathbf{k}'} . \quad (2.13)$$

Since the ground state is the state with the lowest energy, it is found by minimizing Eq. 2.13 with respect to  $v_{\mathbf{k}}$  and  $u_{\mathbf{k}}$  [21]. The result reads

$$E_{\text{BCS}}^0 = \sum_{\mathbf{k}} \xi_{\mathbf{k}} (1 - \xi_{\mathbf{k}}/E_{\mathbf{k}}) - L^3 \frac{\Delta^2}{V_0} , \quad (2.14)$$

with the important parameter

$$\Delta = \frac{V_0}{L^3} \sum_{\mathbf{k}'} u_{\mathbf{k}'} v_{\mathbf{k}'} . \quad (2.15)$$

$\Delta$  indicates the energy, which the system gains by the transition into the superconducting state. Starting from the normal conducting state, electrons from the energy range  $E_F - \Delta \leq E \leq E_F$

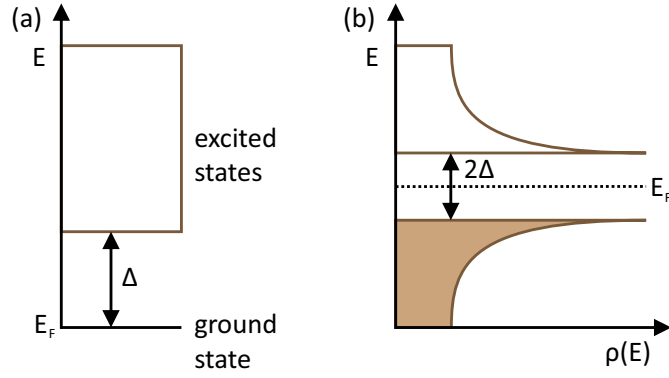


Figure 2.3: The superconducting quasi-particle DOS derived by BCS theory. The figure is based on Ref. 21. (a) Due to their bosonic behavior, Cooper pairs can occupy the same BCS ground state. Excited single electron states require at least the additional energy  $\Delta$ . (b) The superconducting quasi-particle DOS exhibits the characteristic gap  $E_g = 2\Delta$  and two coherence peaks at  $E = \pm\Delta$ .

condense into the superconducting state with the energy  $E = E_F - \Delta$ . On average, the system gains  $\Delta/2$  during the condensation process.

For a more detailed calculation of the excitation energy, the BCS ground state is written in the form

$$E_{\text{BCS}}^0 = -2 \sum_{\mathbf{k}} E_{\mathbf{k}} v_{\mathbf{k}}^4. \quad (2.16)$$

The first excited state requires breaking of a Cooper pair with  $(\mathbf{k}' \uparrow, -\mathbf{k}' \downarrow)$ , which is equivalent to  $v_{\mathbf{k}'}^2 = 0$ :

$$E_{\text{BCS}}^1 = -2 \sum_{\mathbf{k} \neq \mathbf{k}'} E_{\mathbf{k}} v_{\mathbf{k}}^4. \quad (2.17)$$

The excitation energy is the difference of the ground state and the first excited state

$$\Delta E = E_{\text{BCS}}^1 - E_{\text{BCS}}^0 = 2E_{\mathbf{k}'} = 2\sqrt{\xi_{\mathbf{k}'}^2 + \Delta^2}. \quad (2.18)$$

Since  $\xi_{\mathbf{k}'}$  is the kinetic energy of the electrons that formed a Cooper pair in the ground state before the excitation, the energy required to excite the system is given by

$$\Delta E \geq 2\Delta. \quad (2.19)$$

As a result, the superconducting excitation spectrum exhibits the characteristic energy gap  $2\Delta$ , as shown in Fig. 2.3(a). It requires at least  $E = \Delta$  to add an additional free electron to the superconducting state. Of course, it can also occupy higher energetic states if the kinetic energy is large enough. In the limit of  $\xi_{\mathbf{k}}^2 \gg \Delta^2$ , the continuous spectrum of states becomes

available, which is similar to the normal conducting phase (Fig. 2.3(a)):

$$E_{\mathbf{k}} = \sqrt{\xi_{\mathbf{k}}^2 + \Delta^2} \approx \frac{\hbar^2 k^2}{2m} - E_F. \quad (2.20)$$

In the superconducting phase, the DOS around the Fermi level is obtained from

$$\rho_s(E_{\mathbf{k}}) / \rho_n(E_F) = \frac{d\xi_{\mathbf{k}}}{dE_{\mathbf{k}}} = \begin{cases} \frac{E_{\mathbf{k}}}{\sqrt{E_{\mathbf{k}}^2 - \Delta^2}} & \text{for } E_{\mathbf{k}} > \Delta, \\ 0 & \text{for } E_{\mathbf{k}} < \Delta, \end{cases} \quad (2.21)$$

under the assumption that the amount of states is the same for the normal conducting and superconducting phase. In vicinity of the Fermi level, the superconducting DOS diverges for  $E = \pm\Delta$  (Fig. 2.3(b)). For higher energies  $E_{\mathbf{k}} \gg \Delta$ , the superconducting DOS is similar to the normal conducting phase. Exciting the single electron state  $\mathbf{k}$  means that it cannot be occupied by a Cooper pair and, therefore, the state  $-\mathbf{k}$  remains unoccupied. Since single electron excitations of the superconducting state are neither of pure electron nor of pure hole character, they are usually referred to as quasi-particle states.

For simplicity, the model discussed here describes superconductivity at zero-temperature. Since the superconducting gap is the direct result of the attractive interaction, it is reduced when the binding energy is weakened by thermal excitations. The BCS theory also predicts the temperature dependence of the superconducting gap  $\Delta(T)$  which is given for bulk superconductors by:

$$\Delta(T) \approx \Delta_0 \sqrt{1 - T/T_c}, \quad (2.22)$$

with  $\Delta_0$  the superconducting gap at zero-temperature [22].  $\Delta_0$  is directly correlated to the critical temperature  $T_c$  by  $\Delta_0 \approx 1.764 k_B T_c$  with the Boltzman constant  $k_B$ . Thus, it depends on the superconducting material, for example  $\Delta_0(\text{Al}) = 179 \mu\text{eV}$  and  $\Delta_0(\text{V}) = 814 \mu\text{eV}$  [25].

### 2.1.3 Characteristic Superconducting Parameters

The main purpose of BCS theory is to microscopically explain the fundamental hallmarks of superconductivity, which are perfect conductivity and perfect diamagnetism. To this end, one needs to understand how the BCS ground state is effected by the flow of electric current. In a superconductor, the Cooper pairs act as charge carriers when their momentum is increased, e. g. by an external electric field. The density of the supercurrent  $\mathbf{j}_s$  is

$$\mathbf{j}_s = -n_s e \mathbf{v} = -n_s e \hbar \mathbf{k} / m, \quad (2.23)$$

## Chapter 2. Theoretical Background

---

with the electron density  $n_s$ . Due to the current flow, each electron of the Cooper pair undergoes a change of momentum according to

$$(\mathbf{k} \uparrow, -\mathbf{k} \downarrow) \rightarrow \left( \mathbf{k} \uparrow + \frac{1}{2} \mathbf{K} \uparrow, \mathbf{k} \downarrow - \frac{1}{2} \mathbf{K} \right). \quad (2.24)$$

Every single Cooper pair gains the momentum  $\mathbf{P} = \hbar \mathbf{K}$ . The many-body wave function (Eq. 2.12) is adapted to the new momentum state:

$$\psi_{(\mathbf{K} \neq 0)}(\mathbf{r}_1, \mathbf{r}_2) = e^{i\mathbf{K}\mathbf{R}} \frac{1}{L^3} \sum_{\mathbf{k}} g(\mathbf{k}) e^{i\mathbf{k}\mathbf{r}} = e^{i\mathbf{K}\mathbf{R}} \psi_{(\mathbf{K}=0)}(\mathbf{r}_1, \mathbf{r}_2). \quad (2.25)$$

Due to the electric current flow the phase of the superconducting wave function is changed by  $e^{i\mathbf{K}\mathbf{R}}$ . However, this phase change does not effect the probability amplitude  $|\psi|^2$  and, therefore, the electric current flow can be illustrated by shifting the  $k$ -space. The superconducting gap  $\Delta$  is invariant with respect to this  $k$ -shift. This means that inelastic electron scattering (which would lead to electrical resistance) is still suppressed for small excitation energies  $E < 2\Delta$ . Thus, there is no electrical resistance as long as the change of the total momentum  $\mathbf{P}$  is not correlated with excitation energies larger than the superconducting gap. In the case  $E > 2\Delta$ , the superconducting state breaks down and the material becomes normal conducting. This occurs at the critical current density, which is estimated from Eq. 2.23:

$$\mathbf{j}_c \approx \frac{en_s}{\hbar k_F} \Delta. \quad (2.26)$$

The critical current density depends on the Fermi wave vector  $k_F$  and on the superconducting gap  $\Delta$ .

So far, perfect conductivity has been derived for the superconducting state by BCS theory. The second characteristic property of superconductors is ideal diamagnetism; the repulsion of the magnetic field from the interior of the superconductor. The electrodynamics of the phenomenon are described by the second London equation, which is derived by BCS theory. The current density is given by the quantum mechanical momentum operator and the BCS many-body wave function [21]:

$$\mathbf{j} = -\frac{e}{2m} (\psi (-i\hbar\nabla + 2eN\mathbf{A})^* \psi^* + \psi^* (-i\hbar\nabla + 2eN\mathbf{A}) \psi), \quad (2.27)$$

where  $\mathbf{A}$  represents the vector potential,  $2eN$  is the total charge with  $N$  the number of Cooper pairs and  $e$  the electron charge. Neglecting spatial variations of the Cooper pair densities, the expression in Eq. 2.27 is simplified to

$$\nabla \times \mathbf{j} = -\frac{2e^2}{m} N |\psi|^2 \nabla \times \mathbf{A}. \quad (2.28)$$

With the relation  $\mathbf{B} = \nabla \times \mathbf{A}$ , the magnetic field  $\mathbf{B}$  is correlated with the current density  $\mathbf{j}$ :

$$\nabla \times \mathbf{j} = -\frac{ne^2}{m}\mathbf{B}, \quad (2.29)$$

where  $n = 2N/L^3$  is the density of the electrons bound in Cooper pairs. The expression (Eq. 2.29) represents the second London equation (Eq. 2.2) correctly describing the electrodynamics of a superconductor in an external magnetic field.

In the simplified approach presented here, the assumption is made that the spatial distribution of the Cooper pair density is constant. Variations in the Cooper pair density are depicted by the superconducting coherence length  $\xi$ , which is an important parameter for the classification of superconductors. The superconducting gap defines the energy uncertainty  $\delta E$  for the electrons forming Cooper pairs. It is expressed in terms of the momentum uncertainty  $\delta p$ :

$$2\Delta \propto \delta \left( \frac{p^2}{2m} \right) \cong \frac{p_F}{m} \delta p. \quad (2.30)$$

The uncertainty principle correlates  $\delta p$  to the spatial distribution of the Cooper pair wave function  $\delta x$ , which is given by:

$$\xi = \delta x \propto \frac{\hbar}{\delta p} \approx \frac{\hbar p_F}{2m\Delta} = \frac{\hbar^2 k_F}{2m\Delta}, \quad (2.31)$$

$\xi$  is the superconducting coherence length, which describes the spatial variations of the superconducting wave function. It is effected by temperature  $\xi(T) \propto 1/(1 - T/T_c)$  and depends on the superconducting material, for example,  $\xi(\text{Al}) = 1600 \text{ nm}$  [25] and  $\xi(\text{V}) = 44 \text{ nm}$  [26, 29] at zero-temperature.

### 2.1.4 Superconducting Phase Transition in Magnetic Field

So far, the behavior of superconductors in magnetic fields has been described by the Meissner effect and the second London equation (Sec. 2.1.1). However, the London approach does not consider the influence of the magnetic field on the superconducting state as it was derived by BCS theory (2.1.2). In this context, the superconducting phase is only stable as long as expelling the magnetic field requires less energy than the energy gained by the condensation of electrons into the BCS ground state. When increasing the external field, the superconducting ground state inevitably collapses and the superconductor becomes normal conducting. The phase transition into the normal conducting state occurs at the critical magnetic field  $B_c$ . It is calculated from the critical current density (Eq. 2.26) by the Maxwell equation

$$\nabla \times \mathbf{B} = \mu_0 \mathbf{j}, \quad (2.32)$$

$$\int \nabla \times \mathbf{B} d\mathbf{f} = \mu_0 \int \mathbf{j} d\mathbf{f}. \quad (2.33)$$

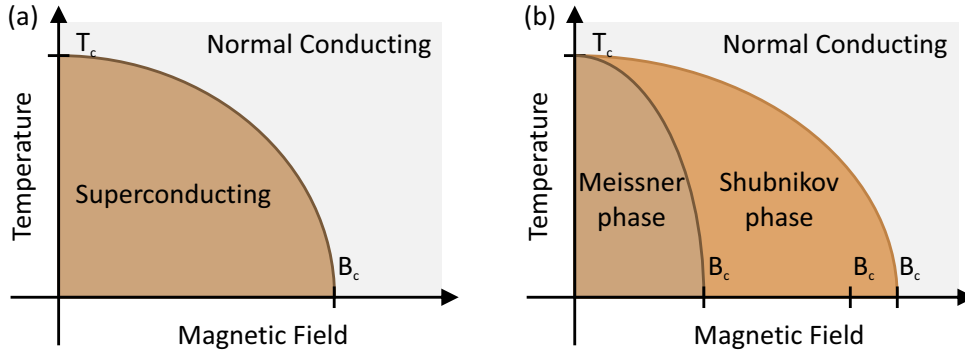


Figure 2.4: Phase diagrams for type I and type II superconductors. Superconductivity is suppressed by temperature and external magnetic fields. (a) Type I superconductors become normal conducting at the critical field  $B_c$  and the critical temperature  $T_c$ . (b) Superconductors of type II exhibit two superconducting phases, which are characterized by the lower ( $B_{c1}$ ) and the upper ( $B_{c2}$ ) critical fields. For  $B < B_{c1}$ , type II superconductors form the Meissner phase similar to type I superconductors. When increasing the magnetic field to  $B_{c1} < B < B_{c2}$ , type II superconductors enter the Shubnikov phase where the superconductor is penetrated by magnetic flux tubes. At higher fields  $B < B_{c2}$ , the metal is in the normal conducting state.

The integral is solved for the simple geometry of a cylindrical superconductor with the radius  $r$  and the length  $l$  in an external magnetic field  $B$ :

$$2\pi r \mu_0 B = \int \mathbf{j} d\mathbf{f}, \quad (2.34)$$

with the geometric simplification  $l \gg r$ . In the cylinder, the supercurrent is confined to a small region close to the surface given by the London penetration depth  $\lambda$  (Sec. 2.1.1). Inserting the exponentially decaying current (Eq. 2.26) in Eq. 2.34 yields the critical magnetic field  $B_c$ :

$$B_c \approx \mu_0 \lambda \frac{en\Delta}{\hbar k_F}. \quad (2.35)$$

For external fields  $B > B_c$ , the superconducting state breaks down and the material becomes normal conducting. Since the superconducting gap  $\Delta$  depends on temperature (Eq. 2.22), a similar relation is valid for the critical field  $B_c$  and the critical current:

$$B_c(T) \propto \lambda j_c(T) \propto \sqrt{1 - T/T_c}. \quad (2.36)$$

In Fig. 2.4(a), the superconducting phase diagram is presented for temperature and magnetic field. The critical fields are rather small for bulk superconductors, for example in bulk Al  $B_c(\text{Al}) = 10.5 \text{ mT}$  and in bulk V  $B_c(\text{V}) = 142 \text{ mT}$  [30].

While the Meissner effect correctly predicts the behavior of most elemental superconductors in magnetic field, a different magnetic field dependence is observed in niobium, vanadium and most superconducting compounds. In 1957, A. A. Abrikosov demonstrated that the ratio  $\kappa$  of the two characteristic length scales — the London penetration depth  $\lambda$  and the

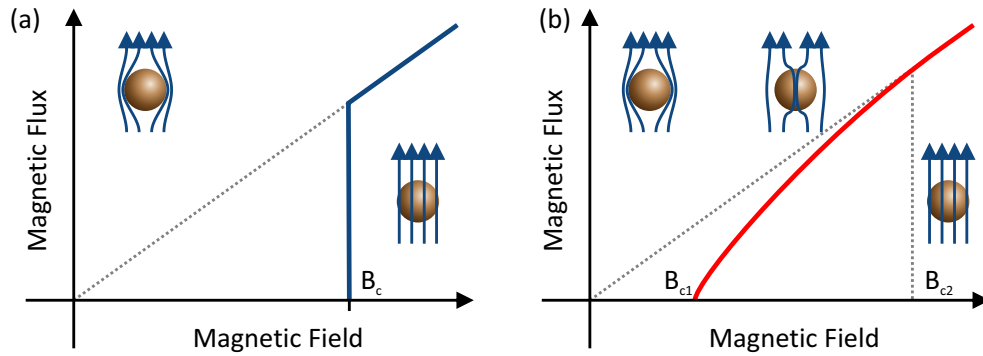


Figure 2.5: Magnetic flux penetration in type I and type II superconductors. (a) In type I superconductors, the magnetic flux is expelled by the Meissner effect. The superconducting state is abruptly suppressed by a first order phase transition at  $B_c$ . (b) In type II superconductors, the magnetic field is only expelled in the Meissner phase, which is limited by the lower critical field  $B_{c1}$ . Increasing the magnetic field to  $B_{c1} < B < B_{c2}$  results in the formation of magnetic flux tubes. Their amount increases with increasing magnetic field until the normal conducting state is reached by a second order phase transition at the upper critical field  $B_{c2}$ .

superconducting coherence length  $\xi$

$$\kappa = \frac{\lambda}{\xi} \quad (2.37)$$

governs the superconducting response to the magnetic field.<sup>4</sup> For superconductors with  $\kappa = \lambda/\xi < 1/\sqrt{2}$ , the Meissner effect is observed up to the critical field  $B_c$ , where the superconducting phase becomes unstable and the superconductor turns normal conducting (Fig. 2.5(a)). Materials of such behavior are referred to as type I superconductors. In these superconductors, the magnetic flux is expelled up to the critical field (except for the regions within the London penetration length).

In Fig. 2.4(b), the phase diagram is presented for superconductors of type II with  $\kappa = \lambda/\xi > 1/\sqrt{2}$ . The Meissner effect is only observed up to the lower critical field ( $B < B_{c1}$ ). For higher fields the flux penetrates the superconductor in the form of flux tubes, resulting in the so-called Shubnikov phase [33]. These flux tubes form a regular array where each flux tube carries the magnetic flux quantum  $\Phi_0 = h/(2e)$ . The existence of the Shubnikov phase has been experimentally observed, for example by scanning tunneling microscopy (STM) [34, 35]. Within the flux tubes, the material is normal conducting while the superconductivity continues to exist in the surrounding regions. For  $B_{c1} \leq B \leq B_{c2}$ , the magnetic flux increases, which is achieved by the formation of additional flux tubes. At  $B = B_{c2}$ , the magnetic flux reaches the vacuum value and, as a result, the superconductivity completely vanishes. For  $\xi \ll \lambda$ , the upper critical field  $B_{c2} = \sqrt{2}\kappa B_c$  greatly surpasses the thermodynamic critical field  $B_c$ . Thus,

<sup>4</sup>The parameter  $\kappa$  was originally introduced in the framework of the Landau-Ginzburg theory [31]. The approach employs the order parameter  $\psi$ , which is correlated to the density of superconducting electrons  $n_s = |\psi|^2$ . When introduced the correlation appeared rather phenomenological but L. P. Gor'kov demonstrated in 1959 that the Ginzburg-Landau formalism is a special form of BCS theory [22, 32].

type II superconductors do not completely fulfill the perfect diamagnetic characteristic in the Shubnikov phase (Fig. 2.5(b)). In addition, the first hallmark — perfect conductivity — is also effected due to the formation of the flux tubes. When current flows through a type II superconductor in the Shubnikov phase, the flux tubes move due to the Lorentz force. The detailed behavior is still subject to ongoing research, but an increase of resistance in the Shubnikov phase is expected according to  $R_s = R_n B / B_{c2}$  where  $R_n$  is the resistance of the normal conducting state [22, 36].

In general, the classification into type I and type II also depends on the purity of the superconducting material. While  $\kappa < 1/\sqrt{2}$  for most elemental superconductors, the ratio is significantly changed by the introduction of impurities. As a result, elemental superconductors of type I containing a certain amount of impurities show similar properties to superconductors of type II. The London equations (Eq. 2.29), as well as the coherence length (Eq. 2.31), are derived for the case of an ideal superconductor, which consists of a perfect crystal lattice. Introducing impurities drastically effects the electron transport because the mean free path  $l$  is shortened. In the dirty limit  $\xi \gg l$ , the effective coherence length  $\xi_{\text{eff}}$  is defined by:

$$\frac{1}{\xi_{\text{eff}}} = \frac{1}{\xi} + \frac{1}{l}. \quad (2.38)$$

Therefore, the effective coherence length is reduced to  $\xi_{\text{eff}} \rightarrow l$  in the dirty limit and  $\kappa$  is significantly increased due to the impurities.

### 2.1.5 First and Second Order Phase Transitions

P. Ehrenfest introduced the earliest formal classification for phase transitions. It is based on the Landau theory, which describes equilibrium states as the minimum of the thermodynamic potential, e. g. the Gibbs energy. To classify the order of the phase transition, the response of the potential is analyzed for fluctuations of the thermodynamic variables, such as temperature  $T$  or magnetic field  $B$  [24]. The phase transition is labeled by the order  $n$ , if  $n$  is the lowest partial derivative of the potential, which is discontinuous at the transition. For example, if the first partial derivative of the Gibbs energy exhibits a jump when changing a thermodynamic variable, the phase transition is first order. However, the approach does not consider divergent derivatives of the thermodynamic potential. Furthermore, the classification into higher orders proves to be meaningless, because the physical differences between the phases become smaller and smaller with increasing order. Therefore, the modern classification scheme only distinguishes between first and second order phase transitions. First order phase transitions release or absorb energy, which is called the latent heat. Second order phase transitions are characterized by continuous first partial derivatives of the Gibbs energy. Their susceptibilities diverge and the coherence length increases to infinity ( $\xi \rightarrow \infty$ ) at the transition.

In Fig. 2.6, the difference between first and second order phase transitions is visualized by the thermodynamic potential. In the Landau theory, an order parameter is identified that usually



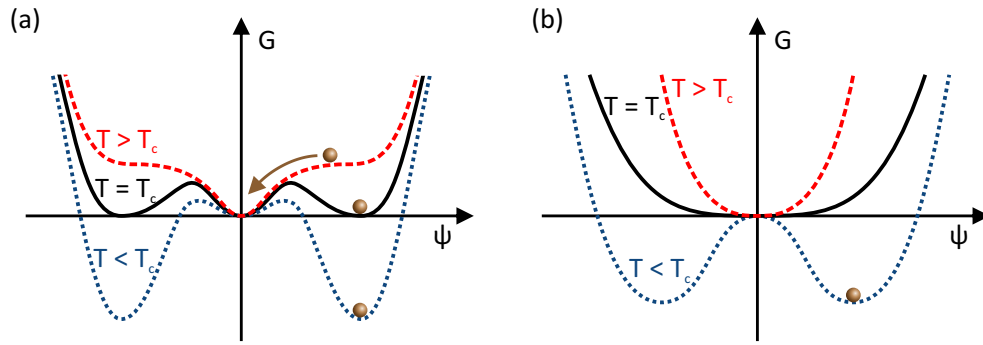


Figure 2.6: Order of the phase transition and thermodynamic potential. (a) For first order phase transitions, the order parameter jumps from the minimum at  $\psi \neq 0$  to the minimum at  $\psi = 0$  when the thermodynamic variable (such as the temperature  $T$ ) reaches its critical value (critical temperature  $T_c$ ). (b) For second order phase transitions, the minima gradually move from  $\psi \neq 0$  to  $\psi = 0$ .

measures the degree of order in the system. For example, it is related to the density of Cooper pairs in superconductors. The approach expands the thermodynamic potential in powers of the order parameter  $\psi$ . Near the first order phase transition, the Gibbs energy  $G$  is given as a function of the order parameter  $\psi$ :

$$G = \frac{1}{2}\alpha\psi^2 + \frac{1}{4}\beta\psi^4 + \frac{1}{6}\gamma\psi^6, \quad (2.39)$$

where  $\alpha$ ,  $\beta$  and  $\gamma$  are functions of the thermodynamic variables, for example  $\alpha = \alpha(B, T)$ . The conditions  $\partial G/\partial\psi = 0$  and  $\partial^2 G/\partial\psi^2 > 0$  reveal existing solutions and physical phases, respectively. When multiple solutions  $\psi_{\min,i}$  exist, the stable phase is identified by the lowest energy  $G_{\min}$ . The other states are called metastable, which is observed, for example, in supercooled or superheated phases. In Fig. 2.6(a), the first order potential has three minima for  $T < T_c$ , where the solutions are only stable for  $\psi \neq 0$ . With increasing temperature, the metastable state  $\psi = 0$  becomes equally probable, which implies phase coexistence. At the transition, the equilibrium state switches from the minimum at  $\psi \neq 0$  to the minimum at  $\psi = 0$ . The jump in the order parameter is accompanied by a discontinuity in the first derivative of the Gibbs energy. This behavior is typical for first order phase transitions [24, 37, 38].

In Fig. 2.6(b), the Gibbs energy for a second order phase transition is shown as a function of the order parameter:

$$G = \frac{1}{2}\alpha\psi^2 + \frac{1}{4}\beta\psi^4. \quad (2.40)$$

In this case, there is always a true equilibrium state for  $\beta > 0$ . Below the critical temperature  $T < T_c$ , the minima at  $\psi^2 = -\alpha/\beta$  represent the stable phase for  $\alpha < 0$ . When increasing the temperature,  $\alpha$  increases and, as a result, changes its sign. Therefore, the minimum gradually moves in a second order phase transition to  $\psi = 0$ , which corresponds to the normal conducting state for  $T > T_c$ . In this example, the temperature is used as a thermodynamic

## Chapter 2. Theoretical Background

---

parameter, whereas in real systems such as superconductors, there are additional parameters, for example the external magnetic field.

In general, type I superconductors exhibit a first order phase transition at the critical field  $B_c$ . Experimentally, first order phase transitions are indicated by an abrupt disappearance of the superconducting gap when the external magnetic field reaches the critical value  $B = B_c$ . For  $B = 0$ , type I superconductors exhibit a second order phase transition in temperature at  $T_c$ . With increasing temperature, the superconductivity continuously decreases until it is completely suppressed for  $T = T_c$ . For superconductors of type II, the superconducting phase transition is second order at  $T_c$  for both the Meissner and the Shubnikov phases.

In addition to the type of the superconductor, the phase transition is also governed by the detailed geometry of the superconductor. When geometrically confined to dimensions smaller than the London penetration depth, superconductors in a magnetic field exhibit properties that can significantly differ from their bulk counterparts. In this context, the pioneering experiments were carried out mostly on superconducting thin films in standard sandwich tunnel junctions [6, 39–41]. These devices are formed by a superconducting and a normal conducting electrode that are separated by a thin oxide barrier (Fig. 2.7). In tunnel experiments, the superconducting gap is extracted as a function of external parameters, such as the magnetic field or the temperature. The superconducting gap  $\Delta$  of thin Al films is presented as a function of the external magnetic field  $B$  at the reduced temperature  $\tilde{T} = T/T_c \approx 0.87$  in Fig. 2.7 [39]. Compared to bulk Al, the critical magnetic fields, at which the films become normal conducting, are considerably enhanced due to the geometrical confinement. The effect is ascribed to the suppression of shielding currents, which cannot be formed efficiently. Therefore, the critical current density  $j_c$  is only reached at higher critical fields  $B_c$ , where the superconducting phase transition occurs [6, 39]. In Fig. 2.8, the magnetic field dependence is presented for a superconducting thin film for the temperature regime  $0.74 \leq \tilde{T} \leq 0.973$ . At lower temperature, the superconducting gap remains almost constant and then abruptly vanishes at the critical field. The measurements at higher temperature reveal a more continuous transition, where the superconducting gap slowly decreases until the critical field is reached. While this behavior is reminiscent of first and second order phase transitions, direct conclusions are difficult for the geometrically confined systems, where the superconducting gap does not directly represent the superconducting order parameter. However, it can be shown for those systems that the order of the superconducting phase transition depends not only on temperature but also on geometrical factors such as the film thickness [6, 39].

In addition to thin films, various other geometries have been studied experimentally and theoretically [42–46]. Similar behavior has been observed, for example, in superconducting cylinders, which are placed in magnetic field aligned parallel to the cylinder axis [47]. In these cylinders with the radius  $r$  and the thickness  $d$ , first order phase transitions are observed for  $rd \geq \lambda^2$  and second order transitions for  $rd \leq \lambda^2$  [47].

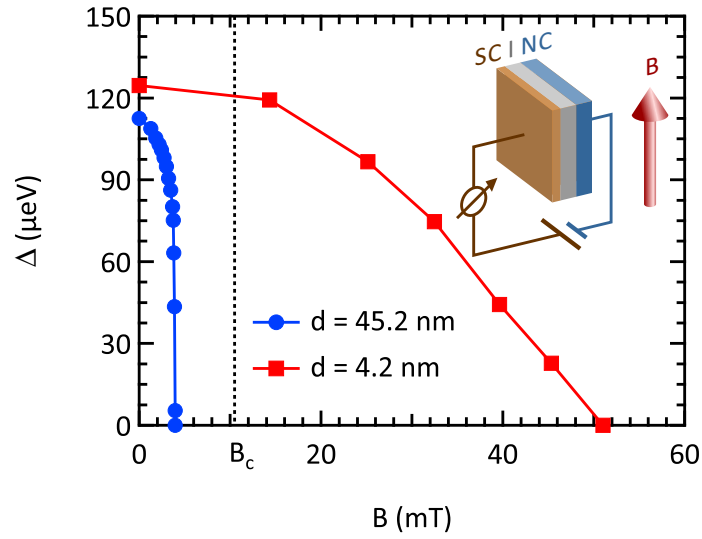


Figure 2.7: Superconducting gap of thin Al films with the thickness  $d$  as a function of external magnetic field  $B$ . When the geometrical confinement of the Al film is in the order of the London penetration depth, the critical field is considerably enhanced. The figure is adapted from Ref. 39.

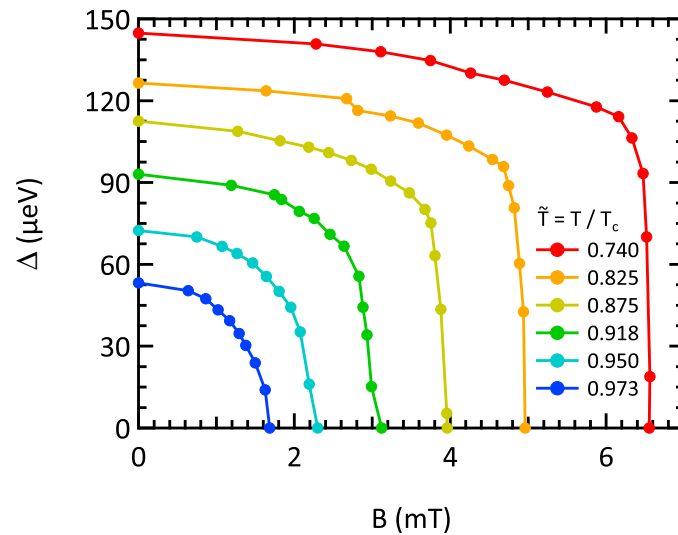


Figure 2.8: The magnetic field dependence of thin Al films (thickness  $d = 452$  nm) at the reduced temperature  $\tilde{T} = T/T_c$ . For lower temperatures, the superconducting gap  $\Delta$  abruptly vanishes at the critical field indicating a first order phase transition. For higher temperatures, the superconducting gap decreases more continuously as predicted for second order phase transitions. The figure is adapted from Ref. 39.

### 2.1.6 Maki Model

The original BCS theory describes the pairing mechanism of Cooper pairs by the interaction of electrons and phonons (Sec. 2.1.2). In practice, the experimental results differ from the original BCS superconducting quasi-particle DOS (Eq. 2.21). Much better agreement is obtained by including depairing effects, which hamper the formation of Cooper pairs in most superconducting materials. In particular, the combination of external magnetic fields and magnetic impurities effects the electron orbital motion and the electron spin due to spin-orbit coupling [48, 49]. In external magnetic fields, depairing effects are mostly induced by paramagnetic impurities, which break the time-reversal symmetry [50]. As a result, the superconducting order parameter, as well as the lifetime of Cooper pairs, is locally decreased, which is manifested in a smaller superconducting gap in close vicinity of the magnetic impurities. Furthermore, the symmetry of electron states is also effected in geometrically confined systems, such as thin film superconductors. In this case, the depairing parameter  $\zeta$  is directly related to the film thickness  $d$  by  $\zeta \propto \tau_\zeta (ev_F d \mu_0 B)^2 / \Delta$ , where  $\tau_\zeta$  is the time between scattering events,  $v_F$  is the Fermi velocity,  $e$  the electron charge,  $\mu_0$  the vacuum permeability,  $B$  the external magnetic field and  $\Delta$  the superconducting gap [51, 52]. In general, the orbital depairing effects are described by a single depairing parameter  $\zeta$  for superconductors, where the mean free path is small ( $l \ll \xi$ ) [48, 51, 53]. In addition, spin-orbit scattering reduces the lifetime of Cooper pairs in superconductors. This effect increases for heavier elements because the spin-orbit scattering potential  $V(r)$  is proportional to  $Z^4$  with the atomic charge  $Z$  in the case of Coulomb interactions.

K. Maki calculated the influence of magnetic and spin-orbit scattering on the superconducting DOS [48]. The Maki model expands Eq. 2.21 by two additional terms. The superconducting quasi-particle DOS is modified to:

$$\rho_{\uparrow\uparrow}(E) = \frac{\rho_0}{2} \operatorname{sgn}(E) \operatorname{Re} \left( \frac{u_{\pm}}{\sqrt{u_{\pm}^2 - 1}} \right), \quad (2.41)$$

where  $u_+$  and  $u_-$  are implicitly defined by

$$u_{\pm} = \frac{E \mp \mu_B B}{\Delta} + \zeta \frac{u_{\pm}}{\sqrt{1 - u_{\pm}^2}} + b \frac{u_{\mp} - u_{\pm}}{\sqrt{1 - u_{\mp}^2}}, \quad (2.42)$$

with  $\rho_0$  the normal conducting DOS,  $E$  the energy,  $\mu_B$  Bohr magneton,  $\Delta$  the superconducting order parameter and  $B$  the external magnetic field. The term  $\zeta \frac{u_{\pm}}{\sqrt{1 - u_{\pm}^2}}$  describes orbital depairing and the spin-orbit scattering results in spin-mixing, which is given by  $b \frac{u_{\mp} - u_{\pm}}{\sqrt{1 - u_{\mp}^2}}$ . The spin-orbit scattering parameter  $b = \hbar / (3\tau_{\text{so}}\Delta)$  depends on the spin-orbit scattering time  $\tau_{\text{so}}$ .

Eq. 2.42 represents a quartic polynomial, which is difficult to solve for  $u_{\pm}$ . The reason for this is

the existence of multiple solutions, which are discussed in Ref. 54. In the case that either  $\zeta = 0$  or  $b = 0$ , the iteration of Eq. 2.42 results in a unequivocal solution for the superconducting quasi-particle DOS. However, the problem is more complicated when both  $\zeta \neq 0$  and  $b \neq 0$ . In this case, there are two non-trivial solutions that result in two different DOS for the Maki model. Detailed analysis reveals that there is one in-phase solution, which correctly reproduces the coherence peaks and is considered the correct physical description. So far, the physical meaning has remained unclear for the second (out-of-phase) solution. Numerically solving the Maki equations (Eq. 2.42) requires that the approach converges to the physically correct solution. To this end, Eq. 2.42 is transformed into four equations for four complex unknowns which are solved by the Newton-Raphson method [55]. The advantage of this approach lies in the fact that the correct physical solution can be identified by the conservation of spectral weight. While  $u_+$  converges to the in-phase solution for  $E > 0$ , it results in the out-of-phase solution for  $E < 0$ . This allows identification of the correct spin-up as well as spin-down DOS for the complete energy range [54, 55].

### 2.1.7 Usadel Equations

Increasing amounts of impurities in a superconductor effect its properties, for example the electronic transport. In the dirty limit, the mean free path of an electron is smaller than the superconducting coherence length ( $l \ll \xi$ ). The theoretical description of superconductors in the dirty limit benefits from negligible electronic anisotropies resulting from the averaging effect of the highly increased scattering rate. The Eilenberger equations of the quasi-classical Green's function formalism [56] can be simplified in the dirty limit because they are nearly isotropic as well [57]. The resulting equations were first obtained by K. Usadel in 1970 [58].

The free energy  $F = TS$  for a superconductor in the dirty limit takes into account the influence of magnetic impurities. For a homogenous magnetic field in the  $z$ -direction, it reads [59]:

$$F = \frac{\pi\rho}{4} T \sum_{\epsilon} \int \text{Re} \left\{ D \left[ (\nabla\theta)^2 + \sin^2\theta (\nabla\phi - 2e\mathbf{A}/c)^2 \right] - 4(\epsilon - ih) \cos\theta - 4\Delta \cos(\phi - \varphi) \sin\theta \right\} d\mathbf{r} + \frac{\rho}{2\lambda} \int \Delta^2 d\mathbf{r}, \quad (2.43)$$

where  $\rho$  is the DOS at the Fermi level per spin channel,  $D$  represent the diffusion constant,  $\mathbf{A}$  is the vector potential and  $\lambda = \ln(2\omega_D/\Delta_0)$  is the Cooper channel interaction constant with the Debye energy  $\omega_D$  [59].  $\theta(\mathbf{r})$  and  $\phi(\mathbf{r})$  are the spectral angles and depend on the Matsubara energy [59]. The Usadel equations for such system are derived by varying the free energy with respect to the spectral angles:

$$\begin{aligned} \frac{D}{2} \left[ -\nabla^2\theta + \sin\theta \cos\theta (\nabla\phi - 2e\mathbf{A}/c)^2 \right] + (\epsilon - ih) \sin\theta - \Delta \cos(\phi - \varphi) \cos\theta &= 0 \\ -\frac{D}{2} \nabla (\sin^2\theta (\nabla\phi - 2e\mathbf{A}/c)) + \Delta \sin(\phi - \varphi) \sin\theta &= 0. \end{aligned} \quad (2.44)$$

The order parameter  $\Delta$  is calculated by the self-consistency condition [59]:

$$\Delta(\mathbf{r}) e^{i\varphi(\mathbf{r})} = \lambda 2\pi T \sum_{\epsilon > 0} \text{Re} \sin \theta_{\epsilon}(\mathbf{r}) e^{i\phi_{\epsilon}(\mathbf{r})}. \quad (2.45)$$

The Usadel equations represent a powerful approach that can be solved either analytically or numerically for various experimental situations, for example for the description of superconducting cones (Chap. 4).

## 2.2 Magnetism and Spin-dependent Transport

In 1915, A. Einstein and W. J. de Haas demonstrated the correlation between magnetism and the spin or the orbital angular momentum of electrons, respectively [60]. While the existence of the electron spin alone already creates a magnetic moment, most magnetic phenomena are the result of many-electron interactions, where the individual spins are coupled into collective order. As a result, the DOS of such materials is spin-dependent and, most importantly, the amount of states differs for spin-up and spin-down electrons at the Fermi level. Since most electronic transport occurs at this energy, great efforts are directed towards creating, processing and detecting spin-polarized currents through an imbalance of spin-up and spin-down electrons [61]. Spintronics is an emerging field of modern applications, which employ both the charge as well as the spin of the electron. Magnetic read-and-write heads of magnetic hard drives represent one of the most prominent examples, which either rely on the giant [62, 63] or the tunnel magnetoresistance effect [64–66]. In this section, the underlying physical models are introduced for the description of magnetic systems. This section presents the relevant magnetic phenomena for this work, mainly summarizing Refs 21, 67, 68.

### 2.2.1 Magnetic Energies

The total magnetic moments of electrons stems from its spin and orbital angular momentum. The intrinsic contribution of the electron spin with the spin moment  $\mathbf{S}$  is given by

$$\boldsymbol{\mu}_s = -g_s \frac{e}{2m_e} \mathbf{S} = -g_s \mu_B \frac{\mathbf{S}}{\hbar}, \quad (2.46)$$

where  $\mu_B$  is the Bohr magneton and  $m_e$  represents the electron mass. The g-factor  $g_s$  was originally derived from the Dirac equation [69] and today represents one of the most precisely known fundamental parameters in physics [70, 71]. In the framework of this thesis, the common approximation  $g \approx 2$  leads for electrons with the spin  $s = 1/2$  to

$$\boldsymbol{\mu}_s \approx \mu_B \cdot \quad (2.47)$$

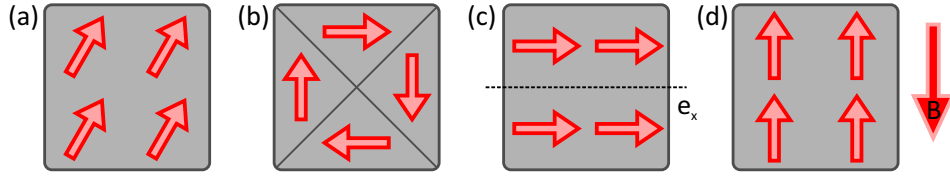


Figure 2.9: Schematic of the spin alignment due to magnetic interactions. (a) The magnetic exchange interaction favors parallel (or anti-parallel) orientation of neighboring spins. (b) The dipole-dipole interaction is long ranged and aims for aligning spin moments parallel to surfaces. (c) In magnetic materials with magneto-crystalline anisotropy, the spins point along the preferred crystal axis ( $e_x$ ). (d) Due to the Zeeman energy, the electron spins align anti-parallel to an external magnetic field.

The orbital contribution of the magnetic moment results from the motion of the electron around the nucleus:

$$\boldsymbol{\mu}_l = -g_l \frac{e}{2m_e} \mathbf{L} = -g_l \mu_B \frac{\mathbf{L}}{\hbar}, \quad (2.48)$$

with the  $g_l$  the electron orbital g-factor. For  $L \neq 0$ , the total magnetic moment depends on the interaction between the quantum numbers for spin  $\mathbf{S}$  and orbital momentum  $\mathbf{L}$ .

The interaction of the individual magnetic moments determines the overall magnetic configuration. In this context, the stable orientation of the magnetic moments has to consider short and long range interactions, the influence of the crystal lattice and the coupling to external magnetic fields. In ferromagnetic materials such as iron, cobalt and nickel, the spontaneous order of the magnetic moments arises from the exchange interaction. In quantum mechanics, the effect is correlated with the symmetry of the many-body wave functions with respect to particle exchange and, thus, it is related to Pauli's exclusion principle for electrons. Besides the symmetry of the wave function, the quantum mechanical approach takes into account the repulsion between electrons as well as the attraction between electrons and positive ions due to the Coulomb potential. As a result, the exchange constant  $J$  determines the orientation of neighboring spin moments. It is employed in the classical Heisenberg model, which describes the ordering mechanism between spin moments:

$$H_{\text{ex}} = -J \sum_{\langle i,j \rangle} \mathbf{S}_i \cdot \mathbf{S}_j, \quad (2.49)$$

with the classical three-dimensional vectors  $\mathbf{S}_{i,j}$  of unit length. The sign of the exchange constant determines the resulting magnetic order; ferromagnetic order is observed for  $J > 0$ , anti-ferromagnetic order stems from  $J < 0$ . The exchange constant  $J$  depends on the overlap of wave functions, which rapidly decays with increasing distance. Therefore, most ferromagnetic systems are well-described by considering only nearest neighbor interactions [67].

In addition to the exchange interaction, magnetic moments are coupled by long ranged

## Chapter 2. Theoretical Background

---

dipole-dipole interactions. The magnetic coupling depends on the distance  $r_{i,j}$  between two moments  $\mathbf{S}_{i,j}$ :

$$H_{\text{dip}} = -\frac{w}{2} \sum_{i \neq j} \frac{3(\mathbf{S}_i \cdot \mathbf{e}_{i,j})(\mathbf{e}_{i,j} \cdot \mathbf{S}_j) - \mathbf{S}_i \cdot \mathbf{S}_j}{r_{i,j}^3}, \quad (2.50)$$

with the strength of dipole-dipole interactions  $w = \mu_0 \mu_s^2 / 4\pi a^3$ , the vacuum permeability  $\mu$  and the lattice constant  $a$ .  $\mathbf{e}_{i,j}$  is the corresponding unit vector to the space vector  $\mathbf{r}_{i,j}$  pointing from  $\mathbf{S}_i$  to  $\mathbf{S}_j$ . Compared to the exchange coupling, the dipole-dipole interactions are much weaker. However, their relative contribution to the magnetic energy increases with the size of the system due to its long range, which can also produce stray fields. The dipole energy is the reason that the magnetic configuration depends on the geometry of the magnetic body and, therefore, it is also referred to as the magnetic shape anisotropy.

In many magnetic systems, the magnetization is aligned along a certain crystal orientation. The ordering is ascribed to the so-called magneto-crystalline anisotropy whose primary origin is the spin-orbit coupling. The preferred direction is called the easy axis. For the simple case of uniaxial magneto-crystalline anisotropy, the corresponding Hamiltonian reads for an easy  $x$ -axis in the classical case:

$$H_{\text{ani}} = -d_x \sum_i S_{x,i}^2, \quad (2.51)$$

where  $d_x$  is the anisotropy constant for the easy  $x$ -axis.

In an external magnetic field, the magnetic moments align parallel to the field direction. The energy is given by the Zeeman term:

$$H_z = -\mu_s \mathbf{B} \cdot \sum_i \mathbf{S}_i, \quad (2.52)$$

where  $\mathbf{B}$  represents the external magnetic field. Depending on the orientation of the magnetic moment, the energy of the corresponding state is either raised or lowered in energy.

### 2.2.2 Spin Polarization

In ferromagnetic materials, the alignment of spins into a well-defined direction is called the spin polarization. For electronic states, spin polarization means that the spin-degeneracy is lifted for the DOS and, as a result, different amounts of spin-up and spin-down states occur at a given energy. The underlying mechanism can easily be discussed for free electrons in a Fermi gas, where it is also referred to as Pauli paramagnetism [67].



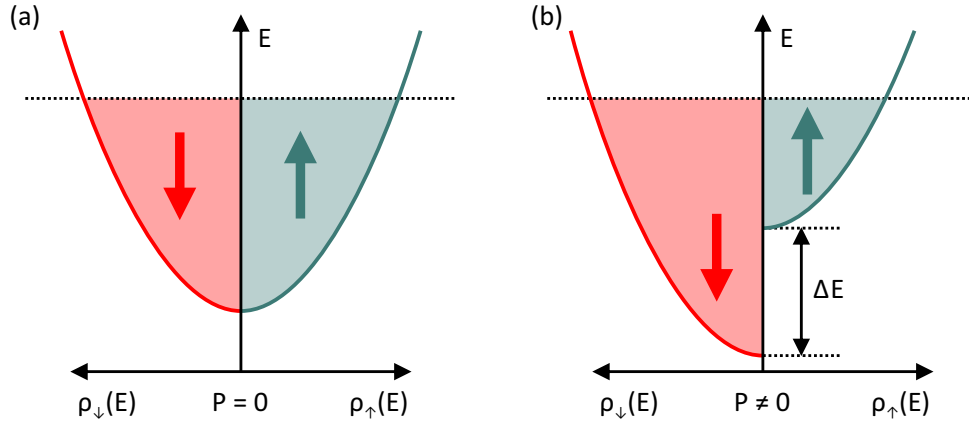


Figure 2.10: Schematic of the spin-polarized DOS for free electrons in an external magnetic field (Pauli paramagnetism). (a) The DOS ( $\rho$ ) corresponds to free electrons in a Fermi gas where the spin-up and spin-down states are degenerate. (b) Due to the Zeeman energy, the DOS is split into two shifted parabola that results in an overall magnetization oriented parallel to the external field. As a result, an imbalance between spin-up and spin-down states is created at the Fermi level.

In Fig. 2.10(a), the DOS for free electrons in a Fermi gas is shown, which follows the relation  $\rho(E) \propto \sqrt{E}$ . In the case of  $B = 0$ , the states are equivalent for both electron polarities. When a magnetic field interacts with the electrons, the spin-degeneracy is lifted due to the Zeeman energy (Eq. 2.52). The energy states of spins oriented parallel to the field is raised by  $E = \mu_B B$  (for the electrons spin  $s = 1/2$ ). Accordingly, the spin orientation anti-parallel to the field is lowered in energy by  $E = -\mu_B B$ . As a result, the DOS for spin-up and spin-down electrons is shifted with respect to the opposite polarity (Fig. 2.10(b)). The resulting equilibrium state creates an imbalance of spin-up and spin-down electrons. In real ferromagnetic systems, the spin-polarized DOS arises from the complex interplay of several magnetic coupling interactions (Sec. 2.2.1).

Due to the shifted DOS, the electron spins are spin-polarized at a given energy  $E$ . The spin polarization  $P$  is calculated by

$$P(E) = \frac{\rho_{\uparrow}(E) - \rho_{\downarrow}(E)}{\rho_{\uparrow}(E) + \rho_{\downarrow}(E)}. \quad (2.53)$$

For electronic transport, the spin polarization at the Fermi level is particularly important. The imbalance of spin-up and spin-down electrons generates spin-polarized currents, which can be exploited in many spintronic applications.

### 2.2.3 Spin-dependent Transport

Most conventional electronic devices utilize the electron charge manipulated by electric fields. However, the electron provides an additional degree of freedom — the spin (Sec. 2.2.1). In spin-

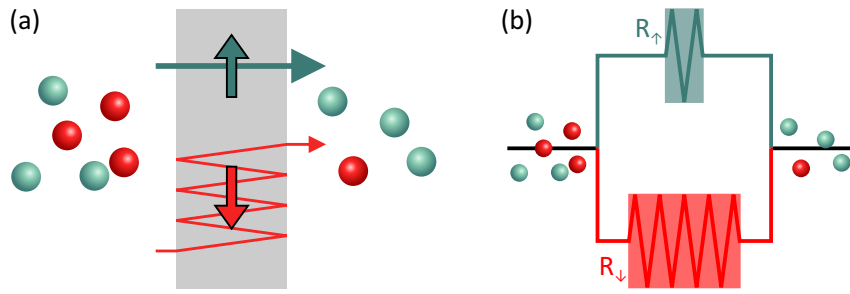


Figure 2.11: Schematic for spin-dependent transport. (a) The transmission probability depends on the spin-orientation of the electrons. (b) The equivalent circuit consists of two channels with different resistances for each spin orientation.

tronics, the electron spin is controlled by external electric and magnetic fields. Spin-dependent transport requires the generation of spin-polarized electrons by creating an imbalance in the spin-up and the spin-down occupation. In their pioneering work, R. Meservey and P. M. Tedrow lifted the spin degeneracy using Zeeman splitting in magnetic fields [7–9]. Later, ferromagnetic films were employed to create and detect spin-polarized currents [62–64]. In this context, electron tunneling (Sec. 3.1.2) plays an important role in magnetic tunnel junctions, where the spin-dependent transport is not only determined by the spin-polarization but also by thin insulating layers (Chap. 5) [65, 66]. The working principle of spin-dependent transport is schematically shown in Fig. 2.11(a). In this case, the transport is favored for spin-up electrons, for example due to less scattering events in ferromagnetic metals or higher tunneling probabilities in ferromagnetic semiconductors. The equivalent circuit consists of two channels for each spin orientation, for which the overall resistance is controlled by external parameters such as the magnetization direction (Fig. 2.11(b)). In principle, several such spin-selective components can be combined into a single device enabling various applications for sensing and logic.

### 2.3 Local Spin Moments Interacting with Superconductors

In the 1960s, L. Yu, H. Shiba and A. I. Rusinov discussed the interaction of an isolated magnetic moment with a superconductor [72–74]. In contrast to the influence of external magnetic fields discussed in Sec. 2.1.4, the single classical spin moments are much more localized and directly interact with the conduction electrons of the superconductor. The underlying physical mechanisms as well as the local effects on the superconducting quasi-particle DOS are theoretically described in this section. This discussion represents an introductory summary of Ref. 11–13, 16, which are recommended for a more detailed description.

### 2.3.1 Magnetic Impurity-induced Bound States in Superconductors

Superconductivity is the result of electrons forming Cooper pairs. At magnetic impurities, the pairing is disturbed due to the interaction with the Coulomb potential and ferromagnetic exchange coupling. The local Coulomb potential arises from the simple fact that the electronic configuration of the impurity is different from its superconducting surrounding. In addition, the exchange energy couples the conduction electrons of the superconducting material and the local spin of the impurity. As a result of the pair breaking, bound quasi-particle states are formed in the superconducting gap, which is free of electronic states in the classic BCS theory.<sup>5</sup> Contrary to the superconducting properties typically defined on length scales in the order of the coherence length, these bound states only appear in the close vicinity of the magnetic impurity. They are spin-polarized and their local distribution can be strongly anisotropic depending on the superconducting wave function. Furthermore, the bound states are expected to modify the properties of the superconducting ground state [12, 13, 15, 75].

For the theoretical description, a localized magnetic spin moment  $\mathbf{S}$  is considered at the position  $\mathbf{r}$  in a two-dimensional lattice [12]. The starting point is the effective Hamiltonian  $H = H_0 + H_{\text{imp}}$ , where  $H_0$  is the unperturbed BCS Hamiltonian and  $H_{\text{imp}}$  describes the interaction with the magnetic impurity. The spin of the magnetic moment interacts with the conduction electrons of the superconductor due to the exchange coupling (Sec. 2.2.1) and the Coulomb potential:

$$H_{\text{imp}} = J\mathbf{S} \cdot \mathbf{s}(\mathbf{0}) + Un(\mathbf{0}), \quad (2.54)$$

with the operators

$$\mathbf{s}(\mathbf{r}) = \frac{1}{2} \sum_{\sigma\nu} \psi_{\sigma}^{\dagger}(\mathbf{r}) \hat{\tau}_{\sigma\nu} \psi_{\nu}(\mathbf{r}), \quad (2.55)$$

$$n(\mathbf{r}) = \sum_{\sigma} \psi_{\sigma}^{\dagger}(\mathbf{r}) \psi_{\sigma}(\mathbf{r}), \quad (2.56)$$

which give the spin and number densities of the conduction electrons [12].  $\hat{\tau}$  describes the particle-hole transformation,  $J$  is the exchange coupling constant (Sec. 2.2.1) and  $U$  represents the local Coulomb potential. The coordinate system is chosen in such a way that  $\mathbf{w} \equiv 1/2J\mathbf{S}$  points into the  $z$ -direction. While the exchange coupling maintains the particle-hole symmetry, it is broken by the Coulomb interaction [12].

For a uniform order parameter, the bound states are induced within the superconducting gap. The spectral density per site is given by [12]:

$$A_{\sigma}(\mathbf{r}, \omega) = -\frac{1}{\pi} \text{Im} G_{\sigma\sigma}(\mathbf{r}, \mathbf{r}, \omega) \quad (2.57)$$

$$= Z_{\sigma}^{(+)}(\mathbf{r}) \delta(\omega - \Omega_0) + Z_{\sigma}^{(-)}(\mathbf{r}) \delta(\omega + \Omega_0). \quad (2.58)$$

---

<sup>5</sup>In tribute to L. Yu, H. Shiba and A. I. Rusinov, the bound quasi-particle states are also referred to as YSR states in the literature.

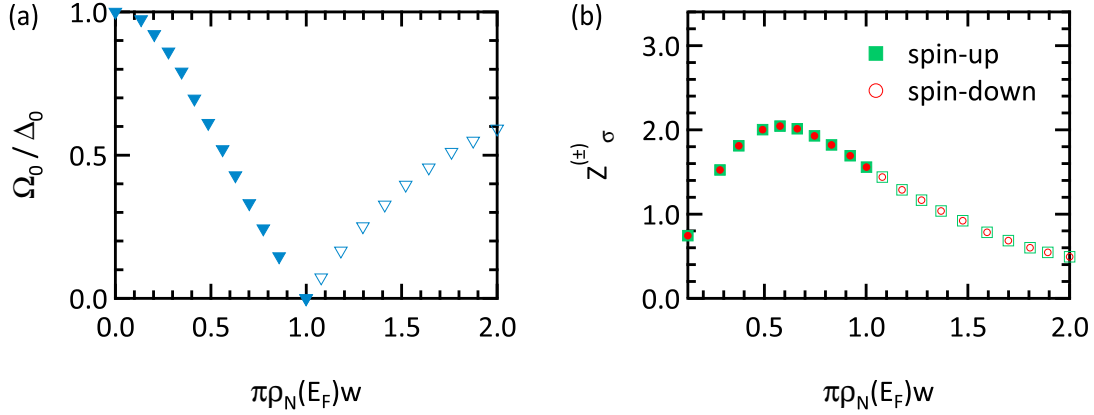


Figure 2.12: Energies and spectral weights of quasi-particle bound states for exchange coupling. The figure is adapted from Ref. 12. (a) When increasing the magnetic interaction  $w$ , the quasi-particle excitation energy  $\Omega$  decreases until the spin character of the bound state changes at  $w_c(U)$ . (b) In the absence of the Coulomb interaction, the spectral weights are similar for spin-up and spin-down bound states. Solid (open) symbols refer to the regime of  $w < w_c$  ( $w > w_c$ ).

The expression includes the single particle Green's function

$$\hat{G}(\mathbf{r}, \mathbf{r}', \omega) = \hat{G}^{(0)}(\mathbf{r} - \mathbf{r}', \omega) + \hat{G}^{(0)}(\mathbf{r}, \omega) \hat{T}(\omega) \hat{G}^{(0)}(-\mathbf{r}', \omega), \quad (2.59)$$

where the scattering processes on the magnetic impurity are described by the matrix

$$\hat{T}(\mathbf{r}, \mathbf{r}', \omega) = \hat{T}(\omega) \delta_{\mathbf{r}0} \delta_{\mathbf{r}'0}. \quad (2.60)$$

In the equilibrium, the energies of the bound states are calculated from

$$\Omega_0 = \text{sgn}(c_+ c_-) \Delta_0 \frac{c_+ c_- - 1}{\sqrt{(c_+^2 + 1)(c_-^2 + 1)}}. \quad (2.61)$$

For  $w < w_c(U) = \sqrt{\pi\rho_N(E_F)^{-2} + U^2}$ , the bound state energy is given by  $\Omega_< = -\Omega_0$ , for  $w > w_c(U)$  the sign is reversed  $\Omega_> = \Omega_0$ . The parameters  $c_\pm = c_w \mp c_u$  describe the exchange coupling

$$c_w = (w/\pi\rho_N(E_F)) / (w^2 - U^2) \quad (2.62)$$

and the Coulomb interaction

$$c_u = (U/\pi\rho_N(E_F)) / (w^2 - U^2). \quad (2.63)$$

The resulting bound states are of quasi-particle character. In this context, the quasi-particle

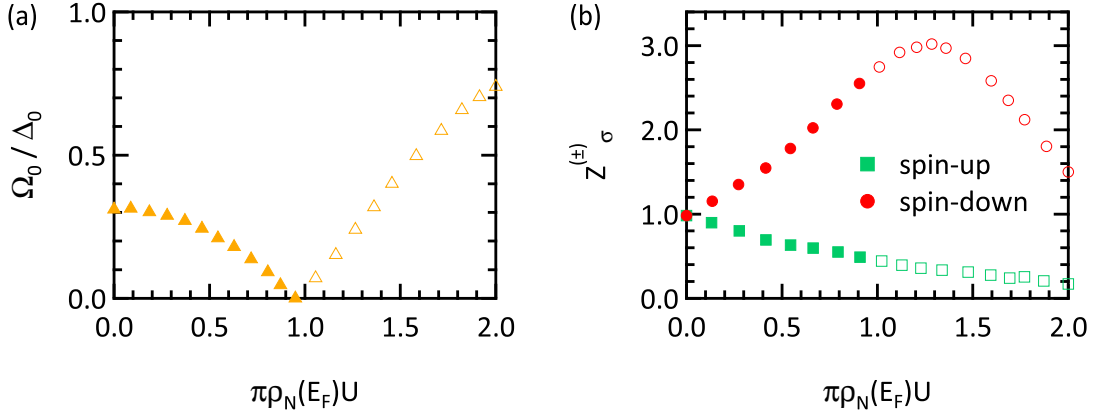


Figure 2.13: Energies and spectral weights of quasi-particle bound states for Coulomb interaction. The figure is adapted from Ref. 12. (a) The Coulomb interaction effects the critical coupling  $w_c(U)$ . (b) The spin-degeneracy is lifted by the Coulomb potential due to the broken particle-hole symmetry. Solid (open) symbols refer to regime of  $w < w_c$  ( $w > w_c$ ).

bound states are referred to as spin-down, when the spin projection of the particle component is anti-parallel and the projection of the hole component is parallel to the spin of the impurity [12]. Neglecting the Coulomb interaction, the minimum excitation energy for the quasi-particle states decreases when increasing  $w$  for  $w < w_c(U)$  (Fig. 2.12(a)). In this regime, the superconducting condensate is stable for quasi-particle excitations with spin-down character. However, its excitation energy would become negative for  $w > w_c(U)$ . Instead, the superconductor undergoes a quantum phase transition to a spin-polarized state. The calculation of the total spin polarization reveals  $\langle s_z \rangle = 0$  for  $w < w_c(U)$  and  $\langle s_z \rangle = -1/2$  for  $w > w_c(U)$  at zero-temperature [12]. For  $w > w_c(U)$  the excitation energy of the quasi-particle bound state increases with increasing  $w$  and changes its spin orientation. In the absence of the Coulomb potential, the same spectral weights are found for the spin-up and spin-down channels (Fig. 2.12(a)). As shown in Fig. 2.13(a) for  $\pi\rho_N(E_F)w = 1.4$ , the Coulomb interaction effects the critical coupling  $w_c(U)$ . Furthermore, different spectral weights for spin-up and spin-down states are observed due to the Coulomb potential and the resulting broken particle-hole symmetry (Fig. 2.13(b)).

### 2.3.2 Spatial Distribution of Quasi-particle Bound States

In general, the relaxation of quasi-particle excitations to the superconducting ground state is expected to occur within the superconducting coherence length (Sec. 2.1.3). Since the Coulomb potential and the scattering potential, respectively, is usually considered as strongly localized for the bound states, they should decay exponentially within length scales on the order of the coherence length when increasing the distance from the magnetic impurity. However, experimental observations suggest that the spectral density vanishes on much shorter length scales, which are in fact in the order of the Fermi length [16, 18]. At first view,

## Chapter 2. Theoretical Background

---

these findings are surprising because decays on such short length scales would suggest energy excitations clearly exceeding the superconducting gap energies, as can be seen from the simple estimation  $E \propto \hbar v_F / l_F$ . The expression reveals energies in the order of the Fermi energy but such states could not be formed within the superconducting gap [12]. Instead, the theoretical model explains the quick decay by a power-law prefactor in the exponential decay of the bound state. For isotropic scattering with a uniform gap function  $\Delta(\mathbf{r})$ , both the Coulomb and the magnetic interaction decay exponentially with the prefactor  $1/r$ , which give squared the prefactor for the spectral weight. Furthermore, it is found that the interaction potentials spatially oscillate with the Fermi wave vector  $\propto \sin(k_F r)$ . The resulting spectral weight of the bound state reads as

$$Z_{\sigma}^{(\pm)}(\mathbf{r}) \propto \left( \frac{\sin(k_F r - \delta^{\pm})}{k_F r - \delta^{\pm}} \right)^2 \exp(-2r |\sin(\delta^+ - \delta^-)| / \xi_0), \quad (2.64)$$

with the Fermi wave vector  $k_F$  and the coherence length  $\xi$  [11, 12, 16]. The phase shifts for scattering of spin-up ( $\delta^+$ ) and spin-down ( $\delta^-$ ) electrons are given by the Coulomb potential and the magnetic coupling [11]. They are correlated to the energy of the formed bound states by [11]:

$$\frac{E}{\Delta_0} = \cos(\delta^+ - \delta^-). \quad (2.65)$$

Due to the prefactor, the spectral weight of the bound state already decreases significantly at length scales much smaller than the coherence length. It is important to mention that constant energy positions of the bound state are assumed for the derivation of Eq. 2.64.

## 3 Experimental Techniques

This chapter introduces the most important experimental techniques for this work, namely the scanning tunneling microscopy (STM) and the Meservey-Tedrow-Fulde (MTF) technique. These techniques represent great inventions opening up entirely new fields of research. In both fields, many achievements have been published ranging from the investigation of fundamental mechanisms to advanced technological applications. While a full coverage is not feasible in the framework of this thesis, the basic concepts of STM and MTF is presented in the following sections.

### 3.1 Scanning Tunneling Microscopy

The STM was developed in 1981 by G. Binnig and H. Rohrer [76–78] who were rewarded with the Physics Nobel Prize five years later. The technique provides the ability to image surfaces with sub-nanometer resolution and to manipulate single atoms or molecules. In addition, STM reveals the detailed electronic properties of the investigated system, such as the local DOS (LDOS). The underlying concept of STM is quantum tunneling. The quantum mechanical phenomenon describes the transmission of particles through barriers, which would not be surmounted in the classical picture. This brief introduction presents the basic working principle of STM and its main components. The discussion of the tunneling theory includes the approaches presented by J. Bardeen to calculate the tunnel current [79] as well as the Tersoff-Hamann model for the special geometry of STM tips [80, 81].

#### 3.1.1 Working Principle

The basic working principle of STM is presented in Fig. 3.1. A conducting tip (usually made from metal wire) is positioned close to a conducting sample. In classical STM, there is no mechanical contact between the tip and the sample; instead, there is a small separation on the order of  $10 \text{ \AA}$ . Applying a bias voltage between tip and sample results in a detectable current flow due to quantum tunneling. The phenomenon is correlated with wave nature of electrons

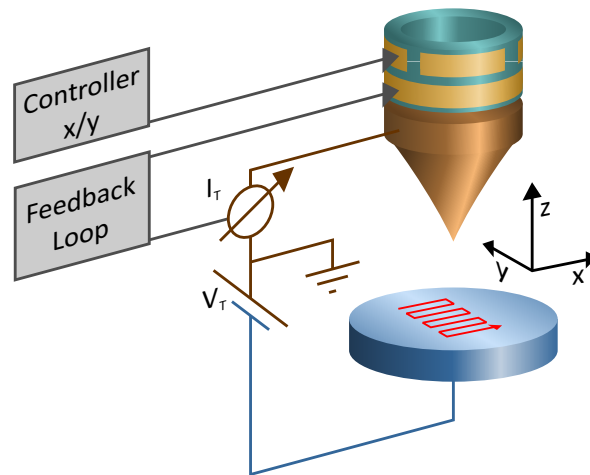


Figure 3.1: Schematic of the STM working principle. The conducting tip is positioned close to the sample in order to enable electron tunneling. Applying an external bias results in the formation of a measurable tunnel current. The current is recorded as the signal for the feedback loop, regulating the tip-to-sample distance. In order to image the surface of the sample, the tip is scanned by an additional  $x/y$ -controller.

in quantum mechanics as described in Sec. 3.1.2. The tunnel currents are usually in the order of 1 nA.

To image the surface of the sample, the tip is scanned over the sample and the resulting tunnel current is simultaneously recorded. (In Sec. 3.1.2, it is explained that STM does not directly image the actual topography of the surface but the local electronic structure.) The spatial positioning of the tip is usually achieved by piezoelectric actuators, which allow moving the tip with atomic scale precision. The two most commonly applied modes of operation are the *constant height mode* and the *constant current mode*. In the *constant height mode*, the  $z$ -position of the STM tip is fixed while the tip scans the sample surface and the tunnel current is recorded. Naturally, the method is only employed for flat surfaces to avoid contact between tip and sample, for example due to atomic step heights. It sets high demands in terms of stability and, therefore, disturbances such as vibrations or piezo creep have to be eliminated. Modern control electronics considerably facilitate this method by automatically compensating piezo effects and by electronically adjusting a flat scanning plane. According to its name, the *constant current mode* employs a fixed set point for the tunnel current. To keep the current constant, the tip-to-sample distance is adjusted by a feedback loop, which records the current as feedback signal for a proportional-integral controller. The optimal setup parameters take into account the roughness of the sample, the scan speed and the required spatial resolution. In 1982, atomic steps were resolved for Au(110) and CaIrSn<sub>4</sub> surfaces [77], the detailed surface  $7 \times 7$  reconstruction of Si(111) was successfully imaged in 1983 [78].

STM greatly benefits from the high sensitivity of the tunnel current with respect to the tip-to-sample distance. In fact, the tunnel current changes by an order of magnitude when the



tip-to-sample distance is changed by only 1 Å, as demonstrated in Sec. 3.1.2. This makes STM very sensitive for detecting small height corrugations of the sample, resulting in highly resolved surface topographies. It is important to mention that the tunnel current is mainly governed by the last atom at the tip apex, in contrast to superconducting length scales such as the London penetration depth or the coherence length (Sec. 2.1.3).

#### 3.1.2 Theoretical Description of Electron Tunneling

The concept of tunneling is discussed for the case of a one-dimensional (1D) potential barrier of thickness  $d$  and height  $V$  (Fig. 3.2). In the classical description, particles can only pass when their energy levels exceed the barrier height ( $E > V$ ), otherwise ( $E < V$ ) the potential step represents an impenetrable barrier. Due to their wavelike nature, the quantum mechanical description of electrons leads to a certain probability for passing the barrier, which is called quantum tunneling. The Schrödinger equation reads for a single electron as follows [82]:

$$\left( -\frac{\hbar^2}{2m} \frac{\partial^2}{\partial z^2} + V(z) \right) \psi(z) = E\psi(z), \quad (3.1)$$

with  $\hbar$  the reduced Planck constant,  $m$  the electron mass and  $z$  the position. The solution of the differential equation depends on the ratio of the electron energy and the potential energy:

$$\psi(z) = \begin{cases} Ae^{ikz} + Be^{-ikz} & \text{for the tip,} \\ Ce^{-\kappa z} + De^{\kappa z} & \text{for the vacuum barrier,} \\ Fe^{ikz} + Ge^{-ikz} & \text{for the sample.} \end{cases} \quad (3.2)$$

In the tip region,  $A = 1$  fulfills the norm for the wave function and  $B$  is the amplitude of the reflected part of the electron wave. For simplification, quantum tunneling is only considered for electrons tunneling from the tip to the sample, which means  $G = 0$ . The wave vector  $k$  of the traveling wave solution depends on the difference between the electron energy and the potential:

$$k = \frac{\sqrt{2m(E - V)}}{\hbar}. \quad (3.3)$$

In the barrier, the energy of the electron is smaller than the potential ( $E < V$ ), which results in an exponentially decaying wave

$$\kappa = \frac{\sqrt{2m(V - E)}}{\hbar}. \quad (3.4)$$

The remaining unknowns ( $B$ ,  $C$ ,  $D$ , and  $G$ ) are calculated from the conditions that both the wave function  $\psi(z)$  as well as its derivative  $\psi'(z)$  are continuous functions in space. The

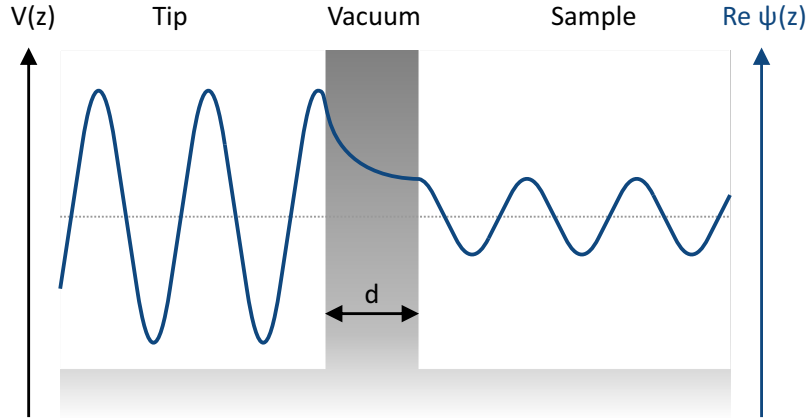


Figure 3.2: Schematic of quantum tunneling in a 1D potential barrier. Due to their wavelike character in quantum mechanics, electrons tunnel through potential barriers with a certain probability, even when their energy levels are below the barrier height ( $E < V$ ).

probability  $P$  for an electron to transmit the tunnel barrier depends on its energy level [82]:

$$P(E) = \frac{4E(V - E)}{4E(V - E) + V^2 \sinh^2(2\kappa d)}. \quad (3.5)$$

In contrast to the classical view, the transmission probability is neither zero for  $E < V$  nor equals one for  $E > V$ . In the case of  $\kappa d \gg 1$ , the probability for an electron transmitting the vacuum barrier exponentially depends on the tunneling distance  $P(E) \propto e^{-2\kappa d}$ .

In 1961, J. Bardeen presented a more general formalism to describe electron tunneling between two isolated electrodes for more complex geometries than the 1D potential barrier. The approach takes into account the existence of multiple conduction channels as indicated in Fig. 3.3(a). In Bardeen's model, the tunnel current is derived by Fermi's golden rule from time-dependent perturbation theory [79]:

$$I = \frac{2\pi e}{\hbar} \sum_{\mu, \nu} (f(E_\mu) - f(E_\nu)) |M_{\mu\nu}|^2 \delta(E_\mu - E_\nu - eV), \quad (3.6)$$

with the Fermi function  $f$ , the applied voltage  $V$  and the energy  $E_\mu$  ( $E_\nu$ ) of the state  $\psi_\mu$  ( $\psi_\nu$ ).  $M_{\mu\nu}$  are the elements of the tunnel transmission matrix, which gives the transmission rate for an electron tunneling from the occupied state  $\psi_\mu$  to the unoccupied state  $\psi_\nu$ :

$$M_{\mu\nu} = \frac{\hbar^2}{2m} \int (\psi_\mu^* \nabla \psi_\nu - \psi_\mu \nabla \psi_\nu^*) dA. \quad (3.7)$$

$M_{\mu\nu}$  is directly correlated to the overlap of the wave functions  $\psi_\mu$  and  $\psi_\nu$ . The integration covers the area  $A$  between tip and sample. In practice, the calculation of the matrix elements is difficult because the wave functions are not known in full detail.

The common work-around for this problem is the Tersoff-Hamann model [80, 81]. The discrete

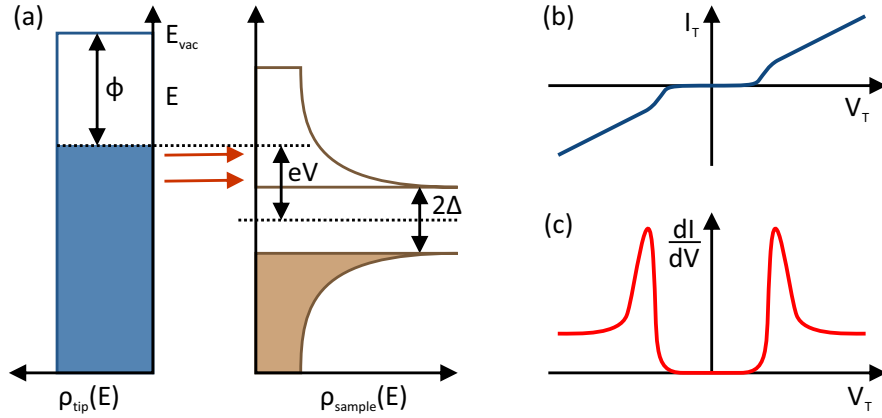


Figure 3.3: Probing the electronic properties by scanning tunneling spectroscopy. (a) The tunnel process is illustrated for the transmission between the normal conducting DOS of the tip ( $\rho_{\text{tip}}$ ) and the superconducting quasi-particle DOS ( $\rho_{\text{sample}}$ ) of the sample. Applying the bias  $V$  results in the formation of a detectable tunnel current. (b) The tunnel current is recorded as a function of the applied voltage. The non-conducting range around the zero-bias arises from the gap in the superconducting DOS. (c) The differential conductance ( $dI/dV$ ) reveals the detailed electronic structure of the sample.

states  $\psi_\mu$  and  $\psi_\nu$  are replaced by continuous distributions, which are given by the DOS for the tip  $\rho_t(E)$  and the sample  $\rho_s(E)$ . The tunnel matrix reads

$$|M_{t,s}(E, V, z)|^2 = \exp\left(-2z\sqrt{\frac{m}{\hbar^2}(\phi_t + \phi_s - eV + 2E)}\right), \quad (3.8)$$

where  $\phi_t$  ( $\phi_s$ ) is the work function of the tip (sample). The resulting tunnel current

$$I(V) \propto \int \rho_s(E) \rho_t(E - eV) |M_{t,s}(E, V, z)|^2 (f(E - eV, T) - f(E, T)) dE, \quad (3.9)$$

depends on the DOS of tip and sample, the temperature  $T$  in the Fermi function  $f$  and the applied bias  $V$ . In the Tersoff-Hamann approach, the DOS of tip and sample are considered constant for the investigated range of energies. More importantly, the model is restricted to wave functions of  $s$ -type which is equivalent to a spherical wave function at the tip apex. The expression for the tunneling current is simplified to

$$I(V) \propto \int \rho_s(E) dE, \quad (3.10)$$

which represents an approximation for zero-temperature ( $T = 0$ ) and small potential differences ( $eV \ll \phi$ ). Then, the measured tunnel current directly reflects the LDOS of the sample.

### 3.1.3 Scanning Tunneling Spectroscopy

STM does not only image the surface of a sample but it also reveals its detailed electronic properties. This ability is primarily employed in scanning tunneling spectroscopy (STS). Differentiating Eq. 3.10 reveals the direct correlation between the differential conductance ( $dI/dV$ ) and the LDOS of the sample ( $\rho_s$ ):

$$\frac{dI}{dV} \propto \int \rho_s(E) f'(E, T) dE. \quad (3.11)$$

In this approximation, the DOS of tip is constant in the investigated energy interval. Broadening effects due to finite temperatures are described by the convolution of the LDOS and the derivative of the Fermi function  $f'(E, T)$ . While the differential conductance can be obtained from differentiating the tunnel current as a function of the applied voltage, the derivative generally reacts very sensitively to parasitic noise in the measurement of the tunnel current. In practice, the differential conductance is usually recorded by a lock-in technique. Here, the applied bias  $V_0$  is combined with a small modulated voltage signal  $V_{\text{mod}}$ :

$$V = V_0 + V_{\text{mod}} \sin(\omega t), \quad (3.12)$$

where  $\omega$  is the modulation frequency. The lock-in detection of the signal averages the LDOS over the modulation range ( $\pm V_{\text{mod}}$ ). Therefore, the choice of the lock-in amplitude is essential in order to resolve the spectral features of interest. Increasing the modulation frequency usually decreases the measurement time required to obtain sufficient signal-to-noise ratios. However, the chosen frequency needs to stay below the bandwidth limitation of the current amplifier and needs to take into account noise frequencies of the system. For example, in order to resolve the Zeeman splitting (Chap. 4 and Chap. 5), the  $dI/dV$  spectra are recorded with a lock-in modulation voltage  $V_{\text{mod}} \approx 5 - 20 \mu\text{V}$  and a modulation frequency of  $f = \omega / (2\pi) \approx 700 \text{ Hz}$ .

The effective energy resolution is a measure of the minimum spectral separation at which two spectral features are still distinguishable. For the experiments presented here, it consists of the thermal broadening  $\Delta E_{\text{thermal}}$  and the lock-in averaging  $\Delta E_{\text{lock-in}}$  [83]:

$$\Delta E \approx \sqrt{(3.5k_B T)^2 + (2.5eV_{\text{mod}})^2}. \quad (3.13)$$

The pre-factor of the thermal broadening describes elastic tunneling, and thus changes for inelastic processes [84]. From Eq. 3.13, the direct correlation becomes obvious between thermal broadening effects and the achievable energy resolution. For example, the MTF-technique (Sec. 3.3) requires recording  $dI/dV$  spectra with an energy resolution in the order of  $100 \mu\text{eV}$  and, therefore, the approach is only suitable in low temperature systems.

### 3.2 Millikelvin Scanning Tunneling Microscope

Since thermal disturbances hamper the investigation of small electronic effects (Eq. 3.13), STM in the low temperature regime represents an especially powerful tool combining high spatial and spectral energy resolution to gain insight into physical mechanisms, that cannot be resolved at higher temperatures. Furthermore, such experiments generally benefit from an ultra-high vacuum (UHV) environment, in which complex *in situ* preparation of tips and samples can be realized. Most experimental work of this thesis has been carried out on an STM operating at millikelvin temperatures in UHV. In addition, external magnetic fields can be applied up to 14 T perpendicular to the sample plane and 0.5 T in-plane. Several technical challenges arise from operating an STM under such conditions. This section represents a brief introduction into the experimental setup, Refs 85, 86 are recommended for a more detailed description.

#### 3.2.1 Overview of the System

In Fig. 3.4, an overview of the millikelvin STM (mK-STM) is presented. The system consists of a cryostat integrating a dilution refrigerator into UHV and the preparation chamber that allows for the *in situ* preparation and transfer of tips and samples. In general, STM experiments react highly sensitively to external disturbances such as mechanical vibrations or electromagnetic radiation. While the influence of the mechanical stability becomes directly obvious for the tip-to-sample distance, to which the tunnel current is directly correlated (Eq. 3.10), electromagnetic noise disturbs the amplification and measurement of the small tunnel currents and bias voltages applied in STM. The influence of external disturbances needs to be limited in order to increase the quality of the experimental data. Since the STM is rigidly attached to the dilution refrigerator for strong thermal coupling, the entire system requires mechanical isolation from external vibrations present in the building. The mK-STM extends over two floors, but is only in mechanical contact to the top floor, where it rests on a combination of active and passive dampers. In addition, all connections to the cryostat, such as the electrical cables and pumping lines, are first anchored on a separate damping stage before they connect to the active and then to the passive damping stages of the cryostat. To minimize disturbing vibrations created by the operation of the dilution refrigerator, the geometry of the STM unit is optimized to limit the influence of mechanical disturbances [87].

The preparation of tips and samples is carried out in the UHV preparation chamber. Pressures in the low  $10^{-10}$  mbar range are achieved by a combination of a main turbo pump, an ion pump and a sublimation pump. For STM measurements, the mechanical turbo pumps are switched off to further reduce vibrations in the STM and to protect the pumps from stray fields of the magnet.

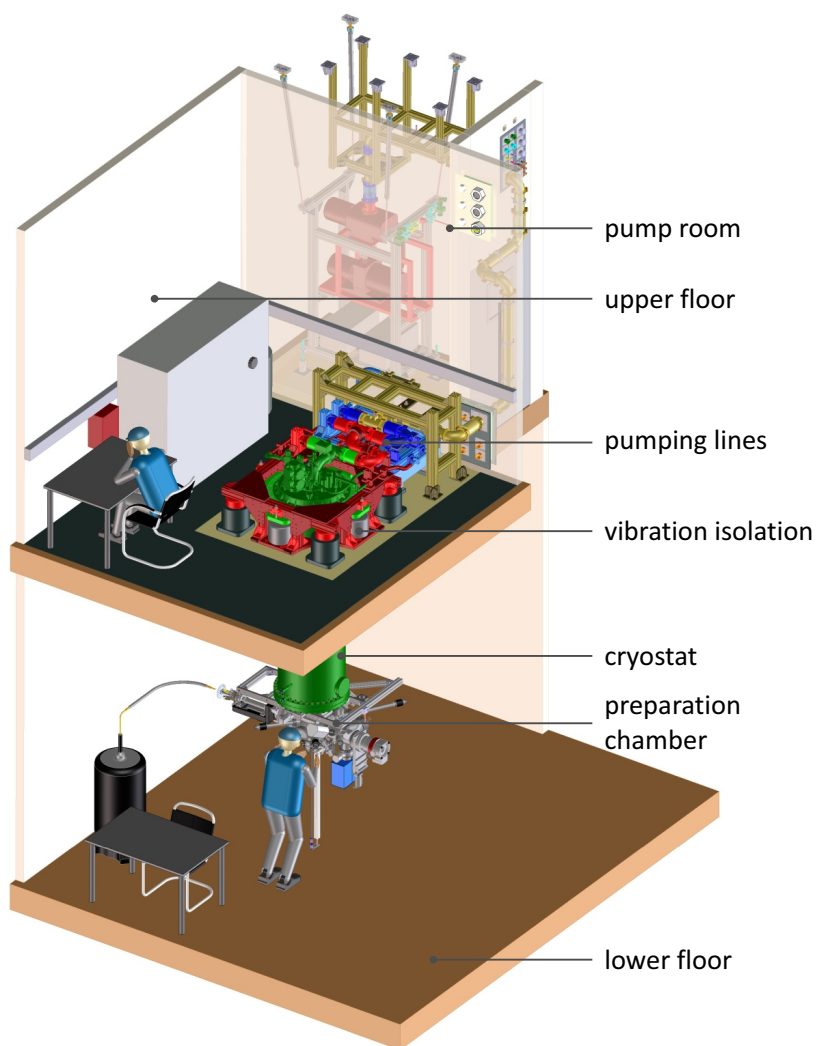


Figure 3.4: Design of the mK-STM (adapted from Ref. 85). The entire system extends over two floors. The cryostat maintenance as well as the STM electronics are accessed in the top floor and the preparation of STM tips and samples is carried out in the UHV chamber located in the lower floor.

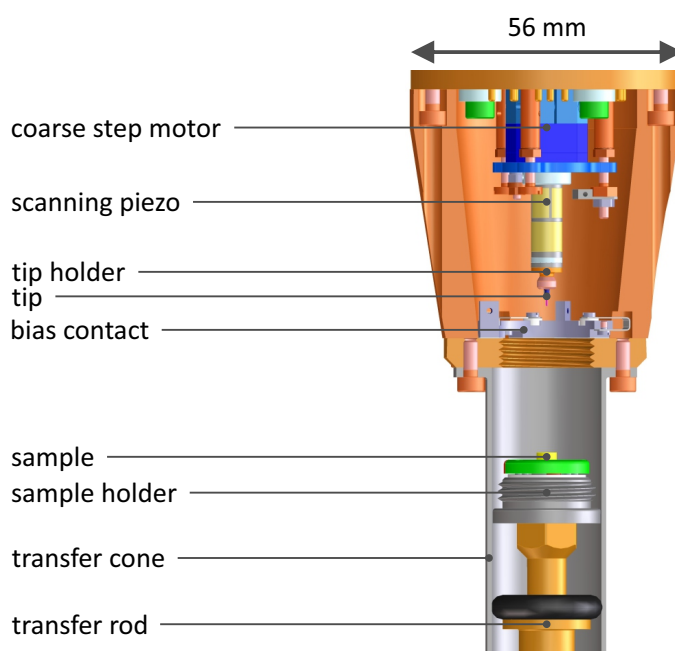


Figure 3.5: Design of the STM unit (adapted from Ref. 85). The STM unit functions under extreme conditions, such as UHV, millikelvin temperatures and high magnetic field.

#### 3.2.2 STM Unit

The STM unit is schematically presented in Fig. 3.5 [85]. In this setup, the position of the sample is fixed while the tip-to-sample distance is controlled by a moveable tip. The positioning mechanism consists of two parts. First, the step motor for the coarse approach moves the tip within 100 nm distance to the sample. The second part is the scan tube, which is made from piezoelectric material and directly attached to the coarse motor. Applying a bias between the inner and outer contacts of the piezoelectric tube enables fine control of the  $z$ -position as well as scanning in the  $xy$ -plane. The tip is mounted on the scan tube with a banana plug, which allows for exchanging tips *in situ*. The external thread of the sample holder fits in the STM, where the bias contact is provided by metal springs. The sample is fixed on the holder by two half-discs, which function as a thermocouple during the sample preparation. The STM unit needs to function in UHV at millikelvin temperatures in high magnetic field. Therefore, the materials selected for its fabrication have low vapor pressures for lower outgassing rates in vacuum and feature high thermal conductivity to increase the cooling efficiency. Furthermore, they show no strong response to external magnetic fields, such as ferromagnetic or diamagnetic behavior. For example, the sample holder is made of silicon silver for high thermal conductivity and better cooling of the sample. The thermocouple consists of Pt/Pt<sub>90</sub>Rh<sub>10</sub> (type S) to avoid superconducting effects at low temperatures, such as the superconducting gap or diamagnetic response to external magnetic fields.

### 3.2.3 Dilution Refrigeration

Low temperatures in the millikelvin regime are achieved by attaching the STM unit to a dilution refrigerator. Its cooling power results from the heat of mixing the two different helium isotopes  $^3\text{He}$  and  $^4\text{He}$  [88]. The refrigeration process is continuous and requires no mechanically moving parts inside the cryostat.

The cryostat (Fig. 3.6) consists of a liquid nitrogen, a liquid helium and a 1 K dewar, which are thermally decoupled by UHV shells. Shielded from thermal radiation by the outer dewars, the central dilution insert can be cooled to 10 mK by circulating a mixture of  $^3\text{He}$  and  $^4\text{He}$ . In the closed  $^3\text{He}$  and  $^4\text{He}$  cycle, the mixture is first pumped through liquid nitrogen and liquid helium cold traps to remove any contamination, such as machine oil of the mechanical pumps. Then, the  $^3\text{He}$  and  $^4\text{He}$  mixture is cooled by the 1 K dewar and a combination of heat exchangers of the dilution unit until it enters the mixing chamber, which represents the coldest part of the cryostat. When cooled down to millikelvin temperatures,  $^3\text{He}$  and  $^4\text{He}$  exhibit characteristic behaviors due to their different amounts of neutrons in the nucleus. The total nuclear spin of  $^4\text{He}$  vanishes ( $I_{^4\text{He}} = 0$ ) and, therefore, it follows the Bose-Einstein statistic that leads to a superfluid transition at 2.17 K.  $^3\text{He}$  possesses a nuclear spin ( $I_{^3\text{He}} = 1/2$ ) obeying the Fermi statistic and Pauli's exclusion principle. While low concentrations of  $^3\text{He}$  form a Fermi liquid in superfluid  $^4\text{He}$  below 2.17 K, high  $^3\text{He}$  concentrations result in a mixture of normal fluid  $^4\text{He}$  and  $^3\text{He}$ . Depending on the  $^3\text{He}$  content of the mixture, a spontaneous phase separation occurs at temperatures below 870 mK and a concentrated ( $^3\text{He}$  rich) phase and a dilute ( $^3\text{He}$  poor) phase are formed. In the mixing chamber of the dilution refrigerator, the concentrated and the dilute phase are only separated by a phase boundary.  $^3\text{He}$  passing from the concentrated to the dilute phase represents an endothermic process, which requires heat from its surroundings. The heat necessary for passing the phase boundary is the cooling power of the refrigeration. The process is enhanced by pumping or even heating the still, where the  $^3\text{He}$  leaves the dilute phase and is compressed by mechanical pumps to reenter the cycle. In the low millikelvin regime, the concentrated phase basically consists of pure  $^3\text{He}$ , which represents the working fluid of the dilution cryostat.

### 3.2.4 Energy Resolution

The temperature of the STM was verified by placing ruthenium oxide sensors at the position of the sample and the tip, respectively [85]. The measurement reveals  $T_{\text{tip}} = 17 \pm 5$  mK and  $T_{\text{sample}} = 20 \pm 5$  mK [86]. However, the energy resolution of electronic measurements is defined by the temperature of the electron bath (Eq. 3.13). Especially at very low temperatures, the temperature of the electron bath is not necessarily the same as the temperature of the solid lattice due to the reduced phonon-electron interactions. Capacitive noise in shielded cables, external radio frequency noise and electromagnetic fields represent disturbances that increase the electron temperature with respect to the lattice. Noise pick-up is prevented by shielding and filtering the signal lines. The filtering consists of external radio frequency filters operating



### 3.2. Millikelvin Scanning Tunneling Microscope

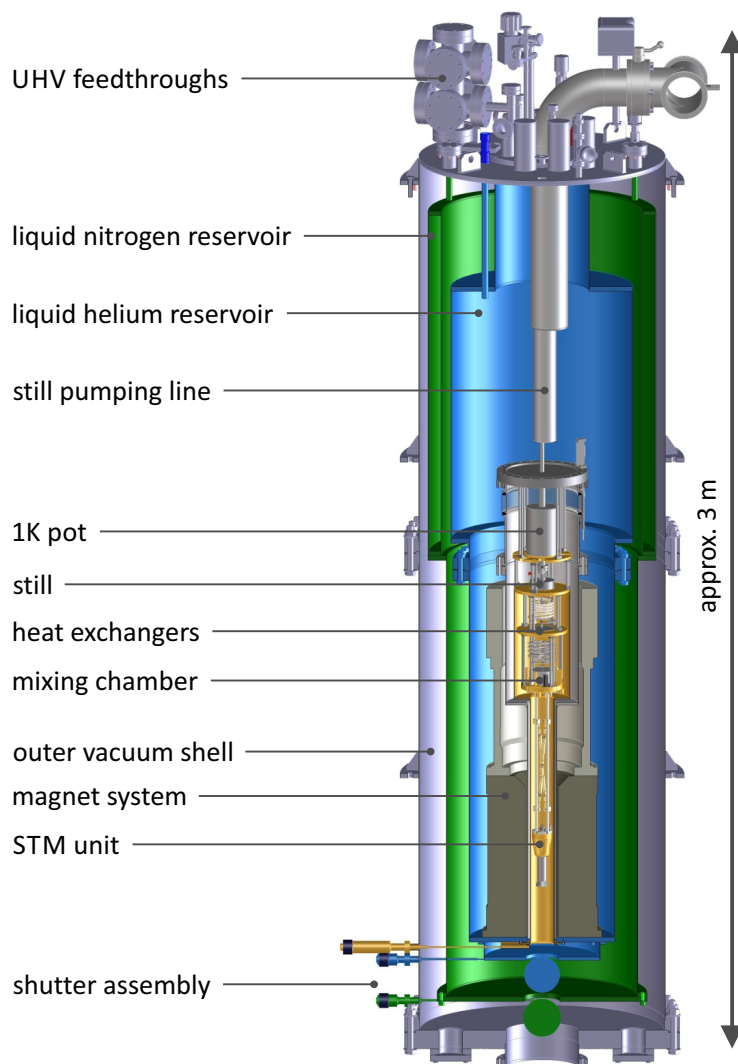


Figure 3.6: The dilution refrigerator of the mK-STM (adapted from Ref. 85). The liquid nitrogen and liquid helium dewars shield the inner dilution unit from thermal radiation. Cooled radiation shields are employed for the same task at the bottom transfer for tip and samples. The cooling power of the dilution refrigerator stems from the heat of mixing liquid  $^3\text{He}$  and  $^4\text{He}$ .

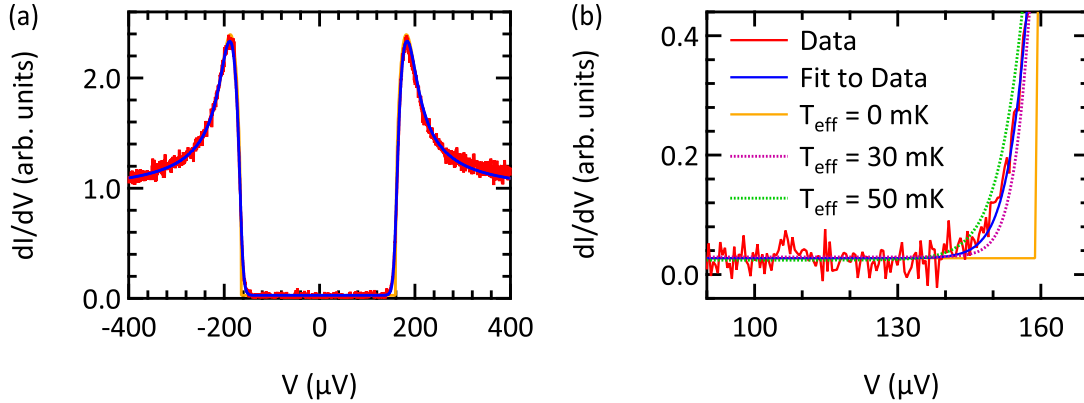


Figure 3.7: Differential conductance measured between a superconducting Al tip and a Cu(111) surface (adapted from Ref. 85). (a) The  $dI/dV$  spectrum is fitted by the Maki equation, in which the effective temperature is a fitting parameter. (b) For the gap edges, the quality of the fit is illustrated by constraining the temperature parameter to fixed values.

at room temperature and an intrinsic filtering effect of the cables at high frequencies. To verify the energy resolution, the superconducting quasi-particle DOS of an Al tip is measured on a Cu(111) surface. The measurement is shown in Fig. 3.7(a). The superconducting gap is fitted with the Maki model (Sec. 3.3.2), in which the temperature parameter is regarded as the effective electron temperature  $T_{\text{eff}} = 38 \pm 1$  mK [86]. It corresponds to an energy resolution of  $\Delta E = 3.5k_B T_{\text{eff}} = 11.4 \pm 0.3 \mu\text{eV}$  [86]. The quality of the fit is illustrated by constraining the temperature parameter to fixed values (Fig. 3.7(b)).

### 3.3 Meservey-Tedrow-Fulde Technique

In the 1970s, R. Meservey, P. M. Tedrow and P. Fulde studied superconducting thin films by tunneling experiments [7–9]. Observing the lifted spin-degeneracy of the superconducting quasi-particle DOS in high magnetic fields, they developed a scheme that employs the superconducting films as a detector for the spin polarization of magnetic materials. Their approach is also known as the MTF technique based on the spin-polarized tunneling of electrons — the origin of spintronics.

#### 3.3.1 Spin-dependent Tunneling

In their pioneering experiments, R. Meservey and P. M. Tedrow used standard thin film tunnel junctions to reveal detailed information about the superconducting quasi-particle DOS [7]. The tunnel junctions typically consist of a thin film superconductor and a normal conducting counter electrode, which are separated by an insulating layer. For example, Al/Al<sub>2</sub>O<sub>3</sub>/Ag was used to investigate the quasi-particle DOS in magnetic fields [7]. When single electrons tunnel in the superconductor, a Cooper pair has to break, which requires the energy  $\Delta$  (Eq. 2.21)

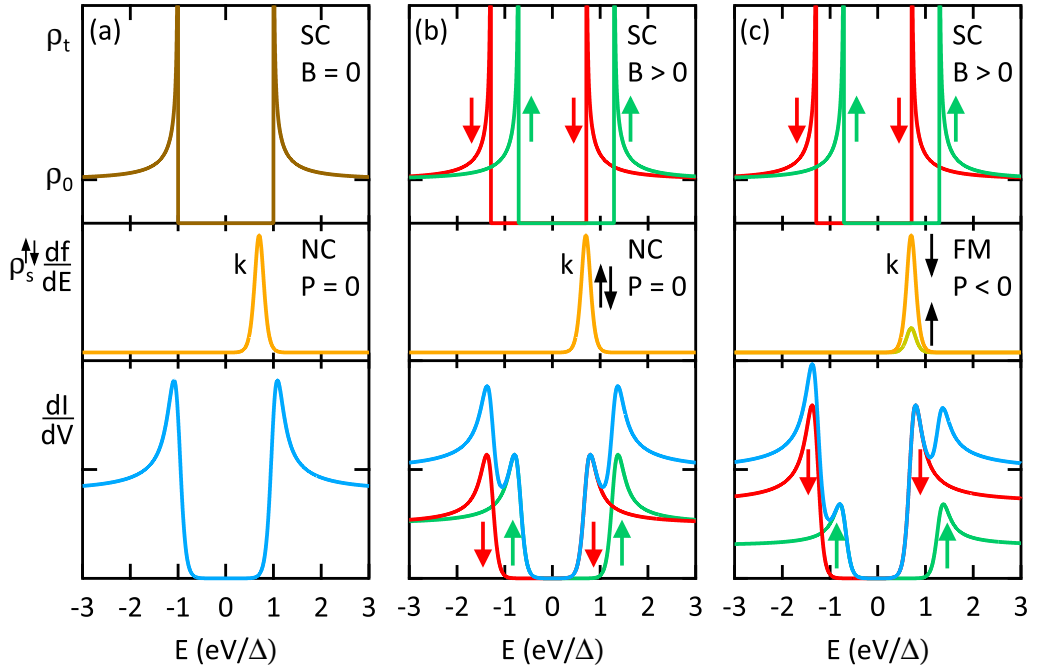


Figure 3.8: Origin of the differential conductance spectra used in the MTF technique [7–9]. This technique employs tunneling experiments between a superconductor (SC) and a normal conducting (NC) electrode separated by an insulating layer. The figure is based on Ref. 9. The top panels depict the quasi-particle DOS of the superconductor ( $\rho_t$ ). The middle panel describes the thermal broadening as well as the two contributions of the spin-up DOS ( $\rho_s^\uparrow$ ) and spin-down DOS ( $\rho_s^\downarrow$ ) of the normal conducting electrode. The resulting  $dI/dV$  spectrum is shown in the bottom panel, where the spin-up (green) and spin-down (red) contributions are also shown separately when they are different. (a) The quasi-particle DOS of the superconductor  $\rho_t$  exhibits a characteristic gap and two coherence peaks (top). The derivative  $k$  of the Fermi function  $f(E)$  takes into account thermal broadening effects (middle). The measured  $dI/dV$  spectrum is the result of convolving the quasi-particle DOS and the derivative of the Fermi function (bottom). (b) In an external magnetic field the quasi-particle DOS is split by the Zeeman energy and four peaks are observed in the  $dI/dV$  spectrum. (c) For a ferromagnetic electrode, a spin polarization at the Fermi level leads to an imbalance between spin-up and spin-down electrons. The spin polarization of the tunneling electrons can be directly extracted from the asymmetry of the  $dI/dV$  spectrum.

according to BCS theory (Sec. 2.1.2). The resulting quasi-particle DOS shows a characteristic gap (Fig. 3.8(a)), which can be measured by the differential conductance (Eq. 3.11). Since the counter electrode is normal conducting, thermal broadening occurs at the Fermi edge of the metal. This is taken into account by convolving the superconducting quasi-particle DOS and the derivative of the Fermi function (Fig. 3.8(a)) as described in Eq. 3.11.

In the Meissner phase, superconductors generally expel external magnetic fields from their interior except for the small regions described by the London penetration depth (Sec. 2.1.1). When the superconductor is geometrically confined to dimensions on the order of the London penetration depth, shielding currents cannot be formed efficiently anymore and, as a result, the critical fields exceed the critical bulk fields (Sec. 2.1.4) [39]. In such devices, the unusual situation emerges that the magnetic field interacts with the majority of the Cooper pairs. In magnetic fields  $B$ , the spin degeneracy of the quasi-particle DOS is lifted by the Zeeman energy creating spin-up and spin-down channels that are separated by  $E/B = 2\mu_B \approx 116 \mu\text{eV/T}$  for  $s = 1/2$ ,  $g\text{-factor} = 2$  and  $\mu_B$  the Bohr magneton (Fig. 3.8(b)). If the normal conducting metal of the tunnel junction is non-magnetic, the contributions of the spin-up and the spin-down channels are equivalent, which results in a symmetric  $dI/dV$  spectrum. In the case of a ferromagnetic sample, however, the DOS typically differs between spin-up and spin-down electrons (Fig. 3.8(c)). Since the measured  $dI/dV$  spectrum is the sum of spin-up and spin-down channels, the spin-polarization of the ferromagnetic electrode at the Fermi level results in an asymmetric  $dI/dV$  spectrum. Analyzing the asymmetry reveals absolute values of the spin-polarization of the tunneling electrons at the Fermi level [8, 9].

When the original BCS superconducting quasi-particle DOS (Eq. 2.21) is employed to extract the absolute spin-polarization, the conductance is only required at four different voltages around  $V_0$  [9, 89], which are given by

$$\sigma_1 = dI/dV(-V_0 - \mu B/e), \quad (3.14)$$

$$\sigma_2 = dI/dV(-V_0 + \mu B/e), \quad (3.15)$$

$$\sigma_3 = dI/dV(V_0 - \mu B/e), \text{ and} \quad (3.16)$$

$$\sigma_4 = dI/dV(V_0 + \mu B/e). \quad (3.17)$$

In this case, the spin-polarization  $P$  is calculated from these four data points by

$$P = \frac{(\sigma_4 - \sigma_2) - (\sigma_1 - \sigma_3)}{(\sigma_4 - \sigma_2) + (\sigma_1 - \sigma_3)}. \quad (3.18)$$

While R. Meservey and P. M. Tedrow chose  $V_0$  to be close to  $\Delta/e$  in order to minimize experimental errors, the choice is arbitrary and does not effect the resulting spin-polarization in the absence of spin-orbit coupling. However, the spin-polarization becomes a sensitive function of  $V_0$  when spin-orbit scattering is taken into account. For such a case, D. Worledge and T. Geballe demonstrated that an original spin-polarization of  $P = 72\%$  can vary between

$P = 41\%$  and  $P = 95\%$  depending on the choice of  $V_0$  [54]. While the influence of either spin-orbit coupling [90, 91] or orbital depairing [91] was discussed, fitting experimental data actually proved challenging when including both contributions at the same time [92]. Therefore, the spin-polarizations obtained from Eq. 3.18 were reduced by 6 – 8% in practice to take spin-orbit interactions into account. A more accurate analysis is provided by solving the Maki equations [48, 54, 55].

#### 3.3.2 Extended Maki Model

The Maki model calculates the superconducting quasi-particle DOS in the presence of magnetic and spin-orbit scattering (Sec. 2.1.6). The theory provides good agreement to experiments carried out on non-magnetic tunnel junctions (Ag/Al<sub>2</sub>O<sub>3</sub>/Al) [52] as well as to spin-polarized measurements (Gd/Al<sub>2</sub>O<sub>3</sub>/Al) [54, 93]. The DOS obtained by the Maki model (Eq. 2.41) is employed to calculate the differential conductance spectra according to Eq. 3.11. In magnetic fields, it consists of the spin-up and spin-down contributions due to the Zeeman energy:

$$\begin{aligned} \frac{dI}{dV} \propto & |N_{\uparrow}| |M_{\uparrow}|^2 \int_{-\infty}^{+\infty} \rho_{\uparrow}(E, B) f'(E + eV, T) dE \\ & + |N_{\downarrow}| |M_{\downarrow}|^2 \int_{-\infty}^{+\infty} \rho_{\downarrow}(E, B) f'(E + eV, T) dE, \end{aligned} \quad (3.19)$$

where  $|M_{\uparrow}|^2$  is the tunnel matrix (Eq. 3.7). Thermal broadening is described by the derivative of the Fermi function  $f'(E + eV, T)$  at the temperature  $T$  (Fig. 3.10). The spin-polarization is given by

$$P = \frac{|N_{\uparrow}| - |N_{\downarrow}|}{|N_{\uparrow}| + |N_{\downarrow}|}. \quad (3.20)$$

In this expression,  $|M_{\uparrow\downarrow}|^2 = 1$  is employed because the detailed wave functions of the electronic states are usually not known in practice. In the following section, the influence of the parameters of the Maki model is demonstrated for several calculated  $dI/dV$  spectra. In Chap. 4 and Chap. 5, a fitting routine based on Eq. 3.19 is used to extract superconducting parameters from spectroscopy measurements.

In order to investigate the influence of orbital depairing and spin-orbit scattering, the superconducting quasi-particle DOS is calculated by solving the Maki equations (Eq. 2.42). The superconducting gap  $\Delta = 400 \mu\text{eV}$  and the external magnetic field  $B = 3 \text{ T}$  are kept constant for these calculations. The counter electrode is non-magnetic ( $P = 0$ ), which leads to symmetric spectral features. In Fig. 3.9(a), the influence is investigated for the orbital depairing parameter at finite temperature  $T = 100 \text{ mK}$ . Due to the Zeeman energy, the coherence peaks of the superconducting DOS are split into the contributions of the spin-up and spin-down

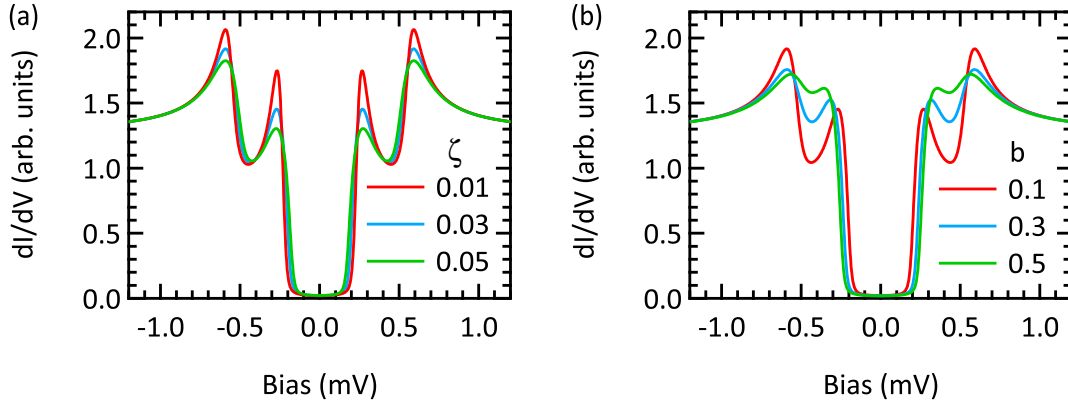


Figure 3.9: Differential conductance spectra calculated by the Maki model to demonstrate depairing and spin-orbit scattering. (a) The coherence peaks appear less pronounced and the superconducting gap decreases due to the orbital depairing. (b) The spin-orbit coupling mixes the spin states and, as a result, the magnitude of the Zeeman split coherence peaks adjust for increasing the parameter  $b$ .

channels. As a consequence of the orbital depairing, the spectral features are less pronounced, for example, the height of the coherence peaks is decreased and the DOS is smeared out at the gap edges ( $V \approx \pm 0.2$  mV). Effectively, the superconducting gap is slightly decreased. The effects increase when increasing the pair breaking parameter  $\zeta$ . However, even for the largest scattering parameter,  $\zeta = 0.05$ , the superconducting gap is not filled in the region close to zero-bias. In Fig. 3.9(b), the effect of spin-orbit coupling is shown. The most characteristic feature is the spin-mixing that forms small peaks at the position of the coherence peaks of the opposite spin moment. In general, the magnitude of the higher peak of the  $dI/dV$  signal is decreased while that of the lower  $dI/dV$  peak is increased. At the same time, the mixing of the spin channels makes the visible separation of the peaks smaller. When the spin-orbit scattering is increased, the mixing of the spin states increases as well. In the limit of  $b \rightarrow \infty$ , the spin channels are no longer separated.

In addition to orbital depairing and spin-orbit coupling, non-equilibrium excitations play a significant role in experiments on superconductors [94, 95]. These excitations mostly occur for energies close to the superconducting gap ( $E \approx \Delta$ ). The time  $\tau_r$  describes the relaxation process for two quasi-particles driven away from the equilibrium state:

$$\tau_r = \sqrt{\frac{\Delta}{T}} \tau_0 e^{\Delta/(k_B T)}, \quad (3.21)$$

where  $\tau_0$  depends on the electron-phonon coupling,  $T$  is the temperature,  $\Delta$  represents the superconducting gap and  $k_B$  is the Boltzmann constant [94, 95]. Relaxation into the ground state results in the reformation of a Cooper pair. Experimentally, the superconducting quasi-particle DOS appears broadened due to the finite lifetime of the quasi-particles. The broadening becomes obvious in the region of the gap edge, especially for higher temperatures [95]. To

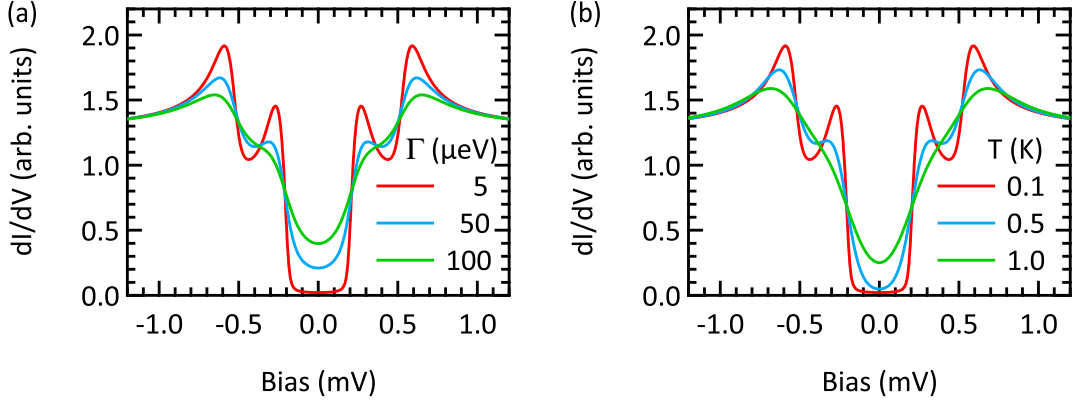


Figure 3.10: Differential conductance spectra calculated by the Maki model to demonstrate the influence of the broadening parameter  $\Gamma$  and temperature  $T$ . (a) Non-equilibrium excitations limit the lifetime of the quasi-particles. As a result, broadening is observed for the superconducting quasi-particle DOS, which is described by the broadening parameter  $\Gamma$ . (b) The effect of thermal broadening is described by the convolution of the  $dI/dV$  spectrum and derivative of the Fermi function  $f'(E + eV, T)$  at the temperature  $T$ .

include finite lifetime effects, the superconducting quasi-particle DOS (Eq. 2.42) is modified by adding an imaginary part to the energy  $E \rightarrow E - i\Gamma$  [95]:

$$u_{\pm} = \frac{(E - i\Gamma) \mp \mu_B B}{\Delta} + \zeta \frac{u_{\pm}}{\sqrt{1 - u_{\pm}^2}} + b \frac{u_{\mp} - u_{\pm}}{\sqrt{1 - u_{\mp}^2}}. \quad (3.22)$$

The parameter  $\Gamma$  broadens the spectral features and results in a much better agreement to data obtained by tunneling experiments [95, 96]. In Fig. 3.10(a), the superconducting DOS is calculated from Eq. 3.22 for several values of  $\Gamma$ . With increasing  $\Gamma$  the spectral features appear less pronounced. For the largest  $\Gamma = 100 \mu\text{eV}$ , the broadening hides the separation of the spin-up and the spin-down contributions. Instead of the Zeeman split coherence peaks, only the formation of a shoulder is observed in the  $dI/dV$  signal. The effects are similar to thermal broadening, which is presented in Fig. 3.10(b) for several temperatures.





# 4 Geometrically Confined Superconductors in Magnetic Fields

In this chapter, the impact of geometrical confinement is investigated for superconducting STM tips in magnetic field. To this end, the experimentally obtained magnetic field dependence for several V tips is analyzed by the extended Maki model and compared to microscopic calculations based on a 1D Usadel equation. The theoretical model for superconducting cones leads to a direct correlation between the detailed geometry and the order of the superconducting phase transition. Comparing the experimental findings to the theory reveals first and second order phase transitions in the V STM tips. In addition, the Usadel theory explains experimentally observed spectral broadening in magnetic fields. Parts of the results discussed in this chapter are already published in Refs 97, 98.

## 4.1 Overview and Motivation

When geometrically confined to dimensions smaller than the London penetration depth, superconductors in a magnetic field exhibit properties that can significantly differ from their bulk counterparts. Such effects have been extensively studied on superconducting thin films using sandwich tunnel junctions [6, 39–41]. Due to the geometrical confinement, the critical magnetic fields, at which the films become normal conducting, are considerably enhanced compared to the bulk [39]. At the critical field, the order of the superconducting phase transition depends not only on temperature but also on geometrical factors such as the film thickness as well as the magnetic field itself (Sec. 2.1.5) [6, 39]. In addition to thin films, various other geometries have been studied experimentally and theoretically such as disks, rings or spheres [42–46].

In this thesis, superconductors are employed as tips in STM. The approach aims to combine the superconducting properties (Sec. 2.1) with the atomic scale resolution of STM (Sec. 3.1). For example, superconducting STM tips can be employed for enhancing energy resolution [18, 99], for accessing parameters of a superconductor [100], as probes for absolute spin polarization (Sec. 3.3), and for designing Josephson junctions [101]. The geometry of such tips is well approximated by cones for the mesoscopic length scales, where superconductivity

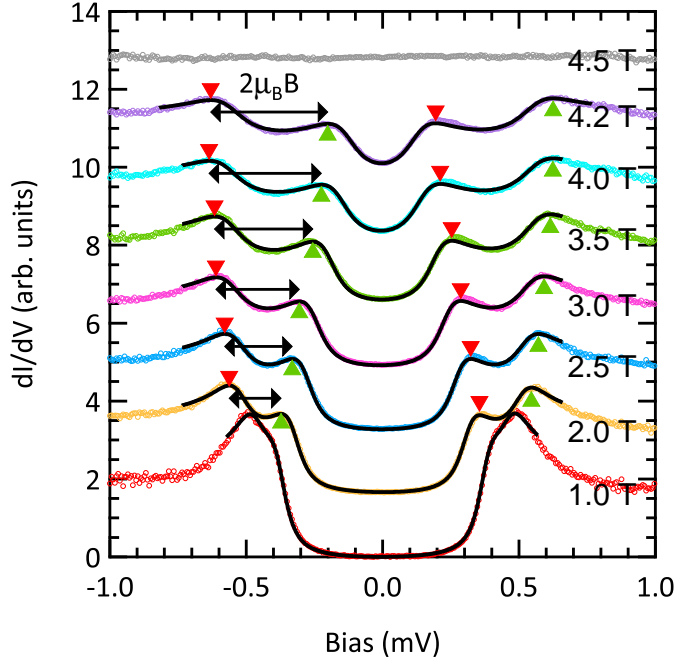


Figure 4.1: Magnetic field dependence of superconducting V tip with sharp spectral features. (a) The  $dI/dV$  spectra are measured with a superconducting V tip on normal conducting V(100) at 15 mK. With increasing external magnetic field the Zeeman splitting (indicated by the horizontal arrows) is enhanced and the superconducting gap decreases. The lines are fits based on Maki’s theory, red (green) triangles mark the coherence peak of the spin-down (spin-up) channel.

has to be described (Sec. 2.1.3). A cone presents a particularly interesting and challenging geometry covering length scales from the atomic scale apex to the macroscopic base [102]. In a conical geometry, it is *a priori* not clear if the superconducting properties are effected due to the mesoscopic confinement, or if quantum size effects have to be considered, as in the case of zero-dimensional superconductors [103–106]. In this context, the magnetic field dependence of the superconducting gap is of fundamental interest. The order of the superconducting phase transition also remains an open question. Therefore, it is essential to understand the impact of the confinement on tunneling experiments employing superconducting STM tips.

## 4.2 Magnetic Field Dependence of Vanadium STM Tips

The experiments were carried out on an STM operating in ultrahigh vacuum (UHV) at a base temperature of 15 mK. External magnetic fields up to 14 T can be applied perpendicular to the sample plane (Sec. 3.2) [85, 86]. The STM tips are mechanically cut *ex situ* under tension from polycrystalline V wire of 99.8 % purity and then transferred to the STM. The thin native oxide is removed by field emission on a V(100) sample, which is cleaned by several cycles of Ar ion sputtering and annealing to 1000 °C. After this procedure, all V tips are superconducting at

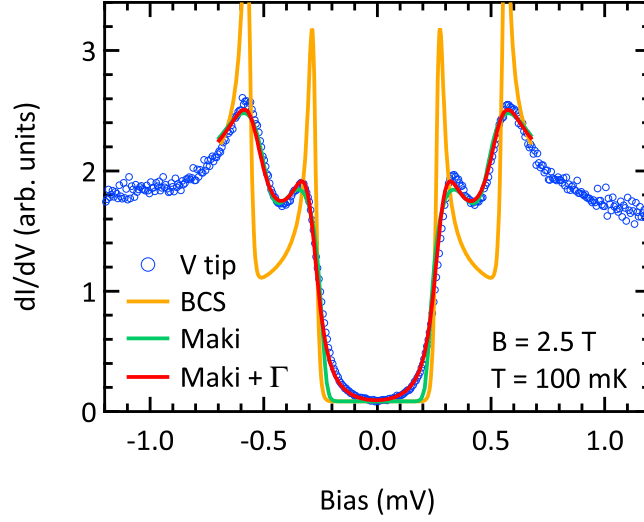


Figure 4.2: Comparison between experimental data and several fit models. The original BCS theory neglects magnetic and spin-orbit scattering. Better agreement is obtained by the Maki model. The filling of the gap is described by the additional damping parameter  $\Gamma$  in the extended Maki model.

about 1 K, but exhibit varying properties, which will be discussed below. In magnetic fields, the superconductivity of the tips is optimized by short bias voltage pulses to shape the tip apex on the V(100) sample. As soon as the tips show superconductivity at higher magnetic fields, the STM unit is cooled down to 15 mK. At this temperature, differential conductance spectra are acquired by a lock-in technique (modulation amplitude  $V_{\text{mod}} = 20 \mu\text{V}$ , modulation frequency  $f_{\text{mod}} = 720 \text{ Hz}$ ). After stabilizing the tunneling contact at  $I_S = 500 \text{ pA}$  and  $V_S = 2.5 \text{ mV}$  the feedback loop is opened and the  $dI/dV$  spectra are measured as a function of the bias voltage.

In Fig. 4.1,  $dI/dV$  spectra measured with a superconducting V tip on a V(100) single crystal are presented for increasing magnetic fields. The magnetic field is perpendicular to the sample surface and parallel to the axis of the tip. Since the critical field for bulk V  $B_{c,\text{bulk}}$  is smaller than 0.5 T [30], the sample is normal conducting for all measurements shown. At the measuring temperature of 15 mK, all spectra feature superconducting quasi-particle DOS for magnetic fields up to 4.2 T, proving that the tip apex remains superconducting. The enhanced critical field results from the confined geometry naturally provided by the tip, which hinders the formation of shielding currents and retains the superconducting phase. The characteristic four-peak-structure of the superconducting coherence peaks is caused by the lifted spin degeneracy of the quasi-particle DOS. The splitting increases with magnetic field  $B$  (see arrows in Fig. 4.1) and follows the theoretical prediction  $\Delta E = 2\mu_B B$  of a system with spin  $s = 1/2$ ,  $g$ -factor = 2 and  $\mu_B$  the Bohr magneton. The superconducting gap becomes smaller and closes at the critical field  $B_c \approx 4.5 \text{ T}$ .

To characterize the data, the superconducting quasi-particle DOS is described by several

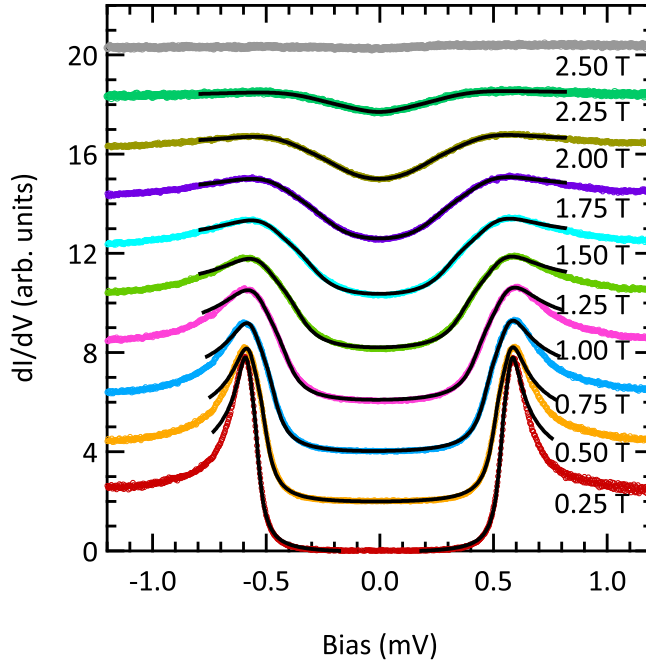


Figure 4.3: Magnetic field dependence of superconducting V tip with broadened spectral features. Compared with the tip in Fig. 4.1, the spectral features appear much broader and the critical field  $B_c \approx 2.5$  T is smaller. This observation indicates the influence of the specific tip geometry.

theories, which are employed as fitting routines in Fig. 4.2. First, a fit based on BCS theory (Eq. 2.21) is exemplarily shown for a measurement at 2.5 T, demonstrating that the  $dI/dV$  spectra of the V tips are in general insufficiently described by BCS theory. This is not too surprising, considering the impurity concentration of the used V wire as well as the spin-orbit coupling in V. The analysis based on the Maki model (Eq. 2.41) takes into account magnetic and spin-orbit scattering [48, 54] and, as a result, much better agreement with the  $dI/dV$  spectra is obtained. While the fit correctly reproduces the Zeeman split coherence peaks, the central gap region still deviates from the acquired data (Fig. 4.2). The  $dI/dV$  spectra usually exhibit broader spectral features than one would expect just from thermal effects at 15 mK. In particular at higher magnetic fields, the filling of the superconducting gap is observed where the  $dI/dV$  signal does not completely go to zero, as predicted by the original Maki model (Eq. 2.41) [48, 54]. Therefore, the extended Maki model is applied with the additional phenomenological broadening parameter  $\Gamma$  (Eq. 3.22) [95]. Including  $\Gamma$  broadens the spectral features and results in a much better fit to the experimental data (Fig. 4.2). It is important to mention that an artificially introduced parameter  $\Gamma$  should not be attributed to any microscopic pair-breaking mechanism. Its appearance is the price one has to pay for a good fitting of experimental data by an oversimplified Maki model. In Sec. 4.3, a microscopic approach based on the Usadel equations is presented, which consistently describes the broadening of the quasi-particle DOS in the tip without any broadening parameters. However, the approach cannot routinely be

## 4.2. Magnetic Field Dependence of Vanadium STM Tips

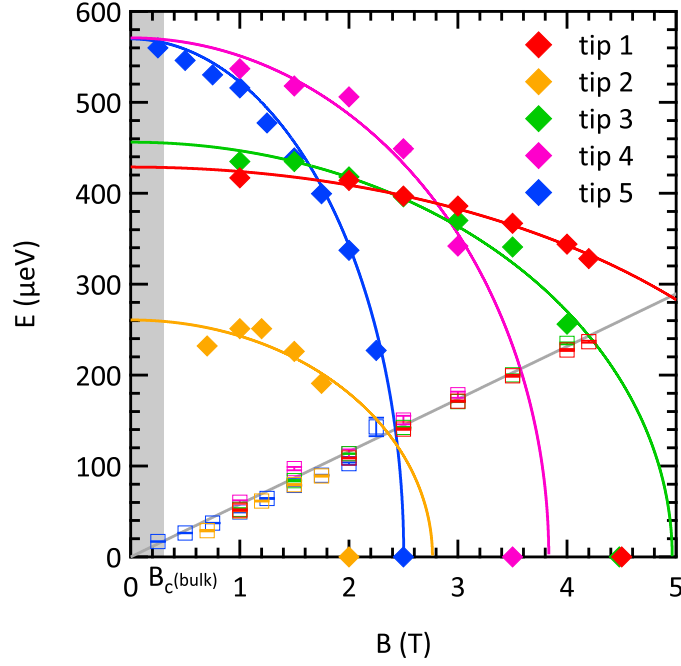


Figure 4.4: Superconducting gaps  $\Delta$  (solid markers) and Zeeman splitting  $\mu_B B$  (open markers) of V tips. The results are derived from experimental data by the extended Maki model. The lines indicate elliptic fits of the superconducting gaps at small  $B$ , which largely overestimate  $B_c$  for most tips deviating from the bulk phase transition.

used as fitting procedure due to the high computational effort.

In Fig. 4.1, the black solid lines represent fits to the data using the extended Maki model (Eq. 2.41 and Eq. 2.42). In Fig. 4.3, the same experiment is repeated with a different STM tip made from V wire. While the superconducting DOS of the tip is clearly visible and similar to Fig. 4.1, the spectral features appear much broader and the critical field  $B_c \approx 2.5$  T is smaller. Fitting the more broadened spectra with the extended Maki equation requires larger  $\Gamma$  values than in Fig. 4.1. The broader spectra can be attributed to a tip that is more blunt as demonstrated in Sec. 4.3. Furthermore, the transition to the normal conducting state at high fields seems smoother than in Fig. 4.1.

Repeating these experiments for several V tips, the superconducting parameters are extracted by the fitting routine based on the extended Maki model. Fig. 4.4 shows the superconducting gap  $\Delta$  (solid symbols) and the Zeeman energy (open symbols) as a function of the external magnetic field  $B$ . The analysis reveals large variations of the critical fields ( $2 \text{ T} \leq B_c \leq 4.5 \text{ T}$ ) as well as of the superconducting gaps at zero-field ( $260 \mu\text{eV} \leq \Delta_0 \leq 580 \mu\text{eV}$ ). The enhanced critical fields  $B_c$  compared to bulk V ( $B_{c,\text{bulk}}$ ) result from the confined geometry naturally provided by the tip. The confinement prevents the efficient formation of compensation currents, which are usually formed to eject external magnetic fields inside the superconductor but tend to destroy superconductivity at the critical current density. Furthermore, the magnetic field dependence

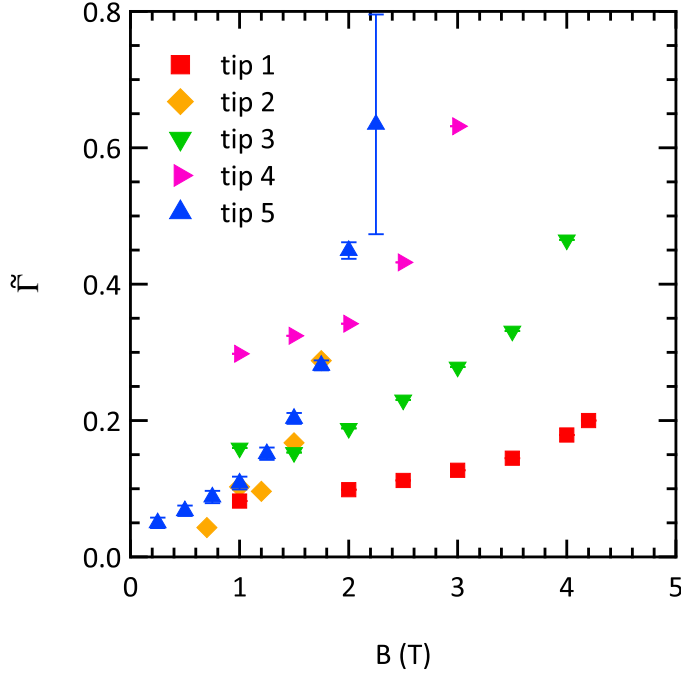


Figure 4.5: The reduced parameter  $\tilde{\Gamma} = \Gamma/\Delta$  for spectral broadening. The fits based on the extended Maki model reveal that  $\tilde{\Gamma}$  increases monotonically with increasing magnetic field for all V tips.  $\tilde{\Gamma}$  as well as the rate of change  $d\tilde{\Gamma}/dB$  indicate the influence of the specific geometry of each tip.

of the superconducting gap  $\Delta$  depends on the specific tip. For example, tip 1 (Fig. 4.1) remains superconducting at large external magnetic fields and shows a discontinuous transition to the normal conducting state. For other tips, such as tip 5 (Fig. 4.3), a more continuous phase transition is observed where the gap steadily decreases until the superconductivity vanishes. This behavior becomes more obvious when comparing the measured superconducting gaps to ellipses drawn as a guide to the eye in Fig. 4.4. While the ellipses largely overestimate the critical fields of tips 1 and 2, good agreement is found for tip 4 and 5. Different initial superconducting gaps  $\Delta_0$  are found at zero-field, all of which are smaller than the superconducting bulk gap of V [26]. This reduction might be explained by the influence of V oxide at the tip surface, changes in the phonon dispersion, and correspondingly the electron-phonon interaction, or grain size effects within the material [107–109]. An effective reduction in  $\Delta$  due to single magnetic impurities is excluded. At the given 99.8% purity of the V wire, the superconductor is in the dirty limit, such that impurities can be treated in a mean field approach. Furthermore, the observed Zeeman splitting follows the theoretical prediction of a system with spin  $s = 1/2$  and  $g = 2$  for all investigated V tips (gray line and open symbols in Fig. 4.4) [110]. Therefore, the superconducting DOS at the apex is not influenced by the formation of vortices in its vicinity (Sec. 2.1.4) [102].

The phenomenological broadening parameter  $\Gamma$  obtained by fitting the properties of the

## 4.2. Magnetic Field Dependence of Vanadium STM Tips

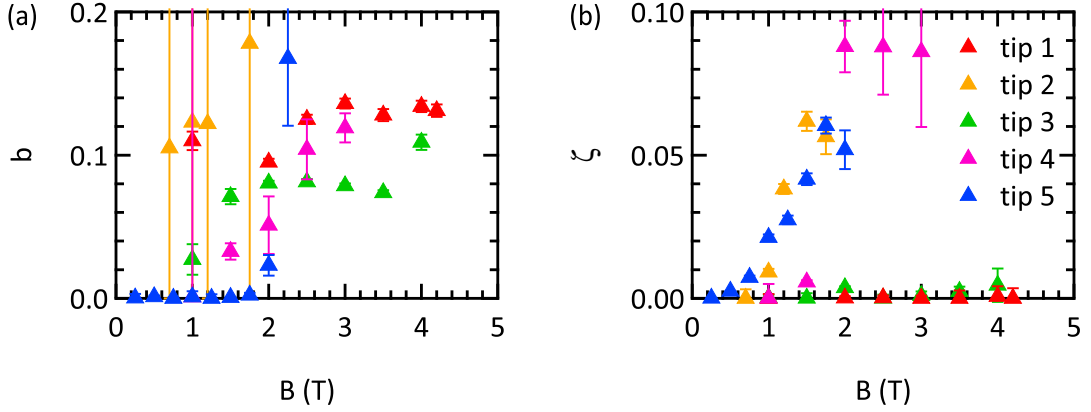


Figure 4.6: The magnetic field dependence for the spin-orbit scattering  $b$  and the orbital depairing  $\zeta$ . (a)  $b$  only slightly increases with increasing field. The sudden increase for  $B \rightarrow B_c$  of tip 3 and 5 is probably correlated with the gap filling rather than with spin-orbit scattering. (b) The depairing parameter  $\zeta$  strongly depends on the tip indicating the influence of its geometry.

superconducting V tips within the extended Maki model is shown in Fig. 4.5, where the reduced broadening parameter  $\tilde{\Gamma} = \Gamma/\Delta$  is plotted as a function of the external magnetic field. When increasing the external field, the values of  $\tilde{\Gamma}$  increase monotonically for all V tips. Both  $\tilde{\Gamma}$  as well as the rate of change  $d\tilde{\Gamma}/dB$  depend on the specific tip, indicating that  $\Gamma$  is correlated with the specific geometry of each tip. To obtain a better understanding of the geometrical influence on the non-uniform superconducting state in the V tips and to find a connection between  $\Gamma$  and the tip geometry, a 1D Usadel equation for a conical superconductor is solved in Sec. 4.3.

In Fig. 4.6, the magnetic field dependence is shown for the spin-orbit scattering  $b$  and the orbital depairing  $\zeta$ . Both effects are minor in comparison with the overall broadening by  $\Gamma$  discussed before. Fixing both parameters to average values only slightly reduces the overall fit quality. In fact, the spin-orbit interaction surpasses the Zeeman energy for the applied fields and, therefore, strong variations in  $b$  are not expected. The orbital depairing is a measure of the kinetic energy of Cooper pairs and is expected to increase in magnetic fields. The depairing parameter  $\zeta$  extracted for the superconducting V tips reveals a monotonic magnetic field dependence. However, the rate of increase strongly depends on the tip indicating the influence of the detailed tip geometry.

The extracted superconducting gaps (Fig. 4.4) diminish differently in increasing magnetic fields. This observation indicates the presence of first and second order phase transitions, which are characterized by the response of the order parameter to an external parameter, e. g. the magnetic field (Sec. 2.1.5). However, extracting the superconducting order parameter is not straight-forward for these measurements due to geometrical confinement, orbital depairing and spin-orbit scattering. Therefore, a more detailed theoretical model is presented for the

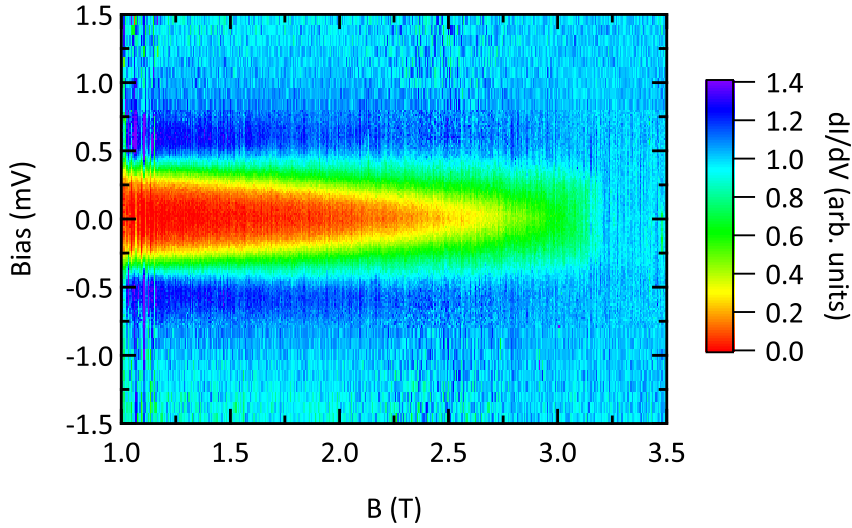


Figure 4.7: Continuous measurement of the differential conductance while ramping the magnetic field. The superconducting quasi-particle DOS of a V tip is measured for magnetic fields from 1 T to 3.5 T. This dynamic method saves measurement time and enables the investigation of the magnetic field dependence with higher resolution.

analysis in Sec. 4.3. The measurements presented in Fig. 4.4 are carried out in static field conditions. To this end, the superconducting magnet of the mK-STM is ramped to the requested field strength and switched to the persistent mode, where the stability of the magnetic field is guaranteed and the power supply can be switched off in order to eliminate additional noise. The method provides the best signal-to-noise ratios, especially in combination with recording times up to 200 ms for each data point of the  $dI/dV$  spectrum. In addition, the acquired spectra are averaged by repeating the measurements up to 20 times. However, such a recording process for the entire magnetic field dependence of the V tip proves very time consuming, which limits the number of investigated magnetic fields.

For the precise characterization of the phase transition, the superconducting gap is required as a function of the magnetic field with the best possible resolution. In Fig. 4.7, the superconducting quasi-particle DOS of a V tip is measured on V(100) while ramping the magnet from 1 T to 3.5 T. This dynamic method shortens the time consuming setting up of each magnetic field value and enables the  $dI/dV$  spectra to be recorded at a much higher magnetic field resolution. However, it comes at the cost of additional noise due to the response of the system to the changing external field and the radio frequency noise of the magnet power supply. In order to minimize these disturbances, the measurement of the  $dI/dV$  spectra is optimized in terms of short recording times (feedback loop off) and small tunnel currents (large tip-to-sample distances). For example, the recording time and the tunnel current for the stabilizing conditions are reduced by a factor of ten. However, the measurements are still highly sensitive to external noise and contact between tip and sample frequently occurs even at low tunnel currents. Since the mechanical contact with the sample usually effects the superconducting



## 4.2. Magnetic Field Dependence of Vanadium STM Tips

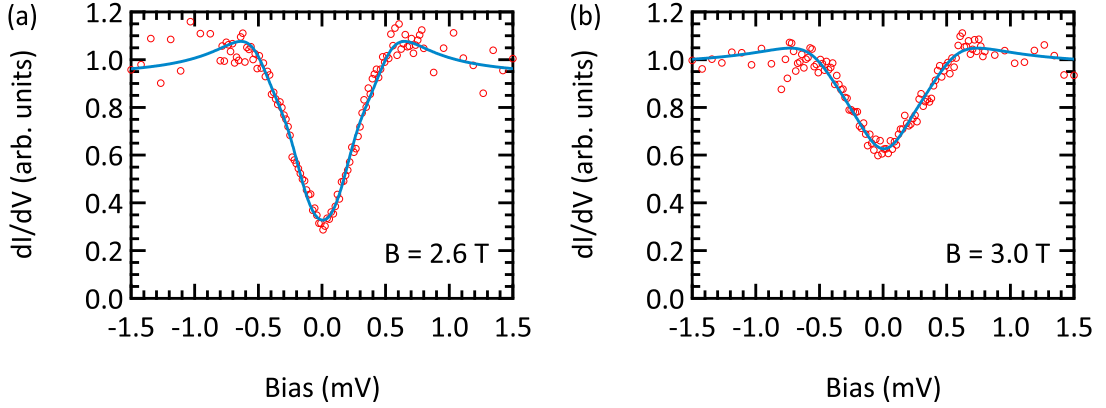


Figure 4.8: Differential conductance spectra and Maki fits for the dynamic measurement method. The density of data points is reduced in comparison to Fig. 4.1 and Fig. 4.3. The fit routine based on the extended Maki model can still be applied to extract the superconducting parameters.

properties, the dynamic method proves unsuitable when comparing the superconducting properties of several V tips.

The measurement presented in Fig. 4.7 progressed successfully without any tip changes. The tunnel contact is stabilized at  $I_S = 200$  pA and  $V_S = 2.5$  mV and the feedback loop is opened to record a  $dI/dV$  spectra as a function of the bias voltage. The feedback is then closed again to stabilize the tunnel contact before the next  $dI/dV$  spectrum is acquired. At the same time, the magnetic field is ramped from 1 T to 4 T (passing  $B_c$ ) at a very slow ramping rate (0.171 mT/s). In this way, more than 550  $dI/dV$  spectra are recorded for the superconducting phase transition. The corresponding magnetic field resolution of 5.34 mT per spectrum allows for a detailed comparison of the differential conductance data and the fit results due to the high density of data points. To this end, the single  $dI/dV$  spectra are analyzed by the fit routine based on the extended Maki model, exemplary shown for two differential conductance spectra in Fig. 4.8 (a) and (b). Compared to the measurements with static magnet field (Fig. 4.1 and Fig. 4.3), the density of data points is reduced by approximately a factor of five. Furthermore, only ten data points are acquired for each bias sign outside the coherence peaks in the normal conducting regime to reduce the recording time. Despite this, the quality of the fits is still acceptable. In Fig. 4.9(a), the differential conductance at zero-bias is compared to the superconducting gap extracted from the Maki fits to entire  $dI/dV$  spectra. The zero-bias conductance ( $dI/dV_{0V}$ ) is normalized with respect to the normal conducting regime ( $dI/dV_{NC}$ ) as  $dI/dV_{norm} = (dI/dV_{NC} - dI/dV_{0V}) / dI/dV_{0V}$  (Fig. 4.9(b)). For small fields ( $B \ll B_c$ ), both approaches lead to similar results. With increasing field, differences become more obvious until large deviations occur close to the critical field ( $B \rightarrow B_c$ ). As will be discussed in Sec. 4.4, first and second order phase transitions are best distinguished in this region. While the continuous approach is too sensitive for a more extended study, this single successful measurement still demonstrates that entire  $dI/dV$  spectra need to be recorded for

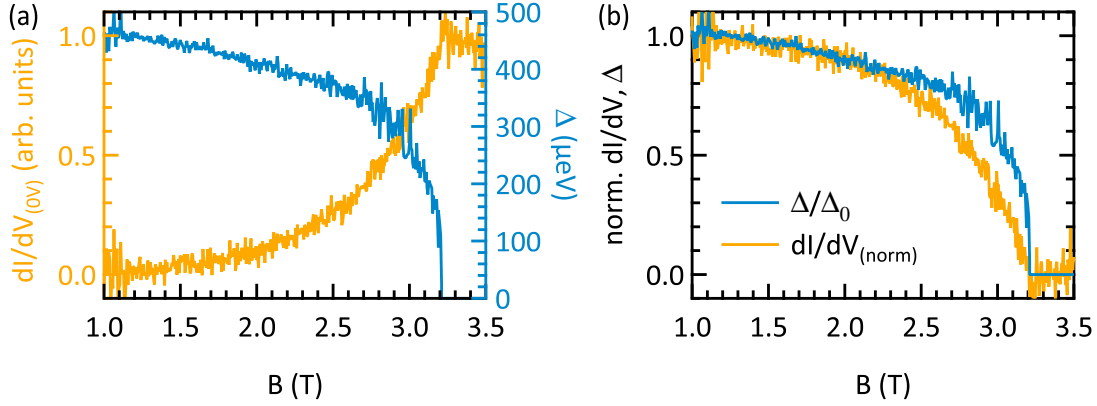


Figure 4.9: Comparison of zero-bias differential conductance and the superconducting gap. The superconducting gaps are extracted by Maki fits to the  $dI/dV$  spectra shown in Fig. 4.7. When normalized, the differences of both approaches become obvious in the regime close to the critical field ( $B \rightarrow B_c$ ), which is essential for the characterization of the phase transition (Sec. 4.4).

the characterization of the superconducting phase transition. In this context, the density of recorded magnetic fields has to be adjusted for static measurements in close vicinity of the critical field, as discussed in Sec. 4.5.

### 4.3 Usadel Equation for Superconducting Cones in Magnetic Fields

For the quantitative description of the non-uniform superconducting state in the V tips, a quasi-classical approach based on the Usadel equation is employed (Sec. 2.1.7) [58]. The approach presented in this section was derived by M. A. Skvortsov and O. V. Kondrashov for the polycrystalline V tips in the dirty limit, where the electron mean free path is smaller than the coherence length ( $l \ll \xi_0$ ). The STM tips are modeled as superconducting cones with the opening angle  $\alpha$  in an external magnetic field  $B$  applied along the tip  $z$ -direction (insets in Fig. 4.11(a) and (b)). In the case  $\alpha \ll 1$ , one can use the adiabatic approximation neglecting variations perpendicular to the cone axis. The resulting 1D Usadel equation for spin-down quasi-particles is expressed in terms of the spectral angle  $\theta_\epsilon(\tilde{z})$  [59]:

$$\frac{\alpha/\alpha_c}{3\sqrt{2}} \mu_B B \left( -\theta_\epsilon'' - \frac{2}{\tilde{z}} \theta_\epsilon' + \tilde{z}^2 \sin 2\theta_\epsilon \right) + (\epsilon - i\mu_B B) \sin \theta_\epsilon = \Delta(\tilde{z}) \cos \theta_\epsilon, \quad (4.1)$$

where  $\epsilon$  is the imaginary Matsubara energy,  $\tilde{z}$  is the dimensionless  $z$ -coordinate defined by  $\tilde{z} = z\sqrt{\pi B \alpha / 2\Phi_0}$ , and  $\Phi_0 = h/2e$  is the superconducting flux quantum. The tip radius at  $z$  is described by the equation  $R(z) = \alpha z$ . In this notation, the critical angle  $\alpha_c$  is defined as

$$\alpha_c = (2\sqrt{2}/3)(c\mu_B/eD) = \sqrt{2}(m_*/m)/(k_F l) \ll 1, \quad (4.2)$$

#### 4.4. Magnetic Field Dependence of Superconducting Cones

with the diffusion coefficient  $D$ , the Fermi wave vector  $k_F$ , and the effective mass  $m_*$ . The order parameter  $\Delta(\bar{z})$  is determined from the self-consistency equation at  $T = 0$ :

$$\Delta(\bar{z}) = \lambda \operatorname{Re} \int_0^{\hbar\omega_D} \sin\theta_\epsilon(\bar{z}) d\epsilon, \quad (4.3)$$

where  $\lambda$  is electron-phonon coupling constant, and  $\hbar\omega_D$  is the Debye energy. The DOS is obtained by analytic continuation:

$$\rho_{\downarrow\uparrow}(E, \bar{z}) = (\rho_0/2) \operatorname{sgn}(E) \operatorname{Re} \cos\theta_{-iE}^\pm(\bar{z}), \quad (4.4)$$

where  $\theta_\epsilon^+(\bar{z}) = \theta_\epsilon(\bar{z})$ , and  $\theta_\epsilon^-(\bar{z})$  is obtained by changing the spin orientation.  $u_\pm = -i \coth\theta^\pm$ , Eq. (4.4) generalizes Eq. 2.42 to a non-uniform case. Calculating the free energy of such a system reveals that the nature of the phase transition at the critical field is determined by the ratio  $\alpha/\alpha_c$ . While for small opening angles  $\alpha < \alpha_c$  (sharp tips) a first order phase transition with abrupt disappearance of the superconducting gap  $\Delta$  at  $B = B_c$  is expected, larger opening angles  $\alpha > \alpha_c$  (blunter tips) exhibit a second order phase transition, with  $\Delta$  continuously vanishing at  $B = B_c$ . The critical field is derived from the free energy as

$$B_c = B_p \frac{1}{\sqrt{1 + (\alpha/\alpha_c)^2}}, \quad (4.5)$$

where  $B_p = \Delta_0 / (g\mu_B)$  is the paramagnetic limit.

#### 4.4 Magnetic Field Dependence of Superconducting Cones

The magnetic field dependence for superconducting cones is numerically calculated by Eq. 4.4 for  $0.2 \leq \alpha/\alpha_c \leq 4$ . For the numerical approach, the differential Usadel equation (Eq. 4.4) is solved under consideration of the boundary conditions, which are given by the self-consistency equation (Eq. 4.3). The calculations are executed in MATLAB using the `bvp5c` solver [111]. As initial starting configuration, the superconducting order parameter in the tip is chosen to decay as a Gaussian function of the dimensionless coordinate  $\bar{z}$

$$\Delta(\bar{z}) = \Delta_0 e^{-\bar{z}^2}. \quad (4.6)$$

The solution provided by `bvp5c` fulfills the boundary conditions  $\phi'(0) = 0$  and  $\phi(z \rightarrow \infty) = 0$ . The iterative procedure is repeated until the difference between the solutions of the last two iterations ( $n$  and  $n - 1$ ) lies below a given threshold value  $t$ :

$$\sum_{\bar{z}} (\Delta_n(\bar{z}) - \Delta_{n-1}(\bar{z}))^2 < t. \quad (4.7)$$

On the one hand, the threshold value should be as small as possible to achieve a converging solution. On the other hand, small thresholds  $t$  drastically increase the number of iterations resulting in unmanageable computation times. In Fig. 4.10(a), the magnetic field dependence

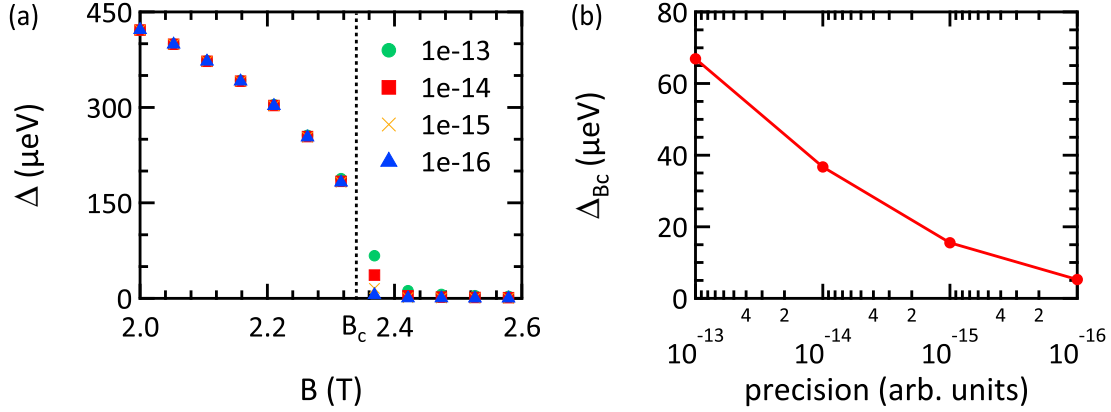


Figure 4.10: Numerical precision of the Usadel approach. (a) The magnetic field dependence of the superconducting gap is numerically calculated for a cone with the opening angle  $\alpha/\alpha_c = 2$ . The solution is effected by the chosen accuracy of the numerical approach. (b) The precision of the numerical procedure is increased until the superconducting gap at the critical field  $\Delta(B_c)$  lies below three percent of its initial zero-field value.

of the superconducting gap is numerically calculated for a conical geometry with the opening angle  $\alpha/\alpha_c = 2$ . Increasing the accuracy of the numerical approach effects the solution considerably in the region of  $B_c$  and in particular for  $B > B_c$ . The analytical expression for the critical field (Eq. 4.5) is used to identify a suitable threshold value, which offers acceptable accuracy in combination with manageable computational times. In Fig. 4.10(b), the resulting superconducting gap at the critical field  $\Delta(B_c)$  is shown as a function of the threshold value  $t$ . According to the analytic expression, the superconducting gap should vanish for  $B \geq B_c$  and, therefore, the precision of the analytic calculations is increased until the superconducting gap at the critical field is below three percent of its initial value ( $\Delta(B_c) < 0.03\Delta_0$ ). In practice, this approach offers a good trade-off between accuracy and computational effort.

The approach based on the 1D Usadel equation provides detailed information about the superconductivity in the cone geometry. In Fig. 4.11(a), the superconducting gap in a tip with  $\alpha/\alpha_c = 0.4$  is displayed as a function of the dimensionless coordinate  $\tilde{z}$ . The figure shows that only the apex of the cone remains superconducting in an external magnetic field for  $B > B_{c,\text{bulk}}$ . When increasing the magnetic field, the superconducting region shrinks and becomes more confined to the apex of the cone. At the critical field  $B_c = 4.35$  T, the superconducting gap vanishes and the entire cone is normal conducting. Fig. 4.11(b) shows the superconducting gap for a wider opening angle  $\alpha/\alpha_c = 3.2$ . Here, the critical field is significantly smaller ( $B_c = 1.27$  T) and the superconducting region is more confined at the tip apex. This indicates a strong influence of the confined geometry, i. e. the opening angle  $\alpha$ .

The geometrical confinement also effects the quasi-particle DOS measured in tunnel experiments. In Fig. 4.12, the calculated quasi-particle DOS at the apex of a superconducting cone is displayed for  $\alpha/\alpha_c = 0.4$  for different external magnetic fields. The spectral features are

#### 4.4. Magnetic Field Dependence of Superconducting Cones

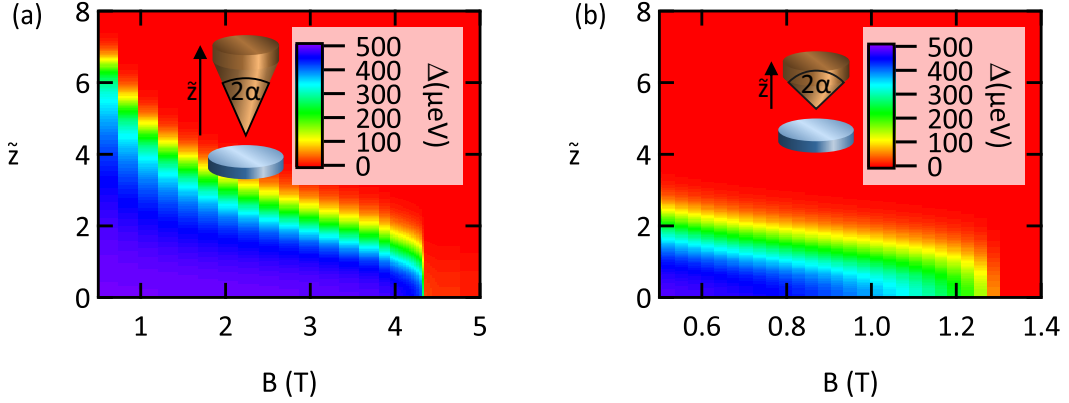


Figure 4.11: Calculated superconductivity of cones with opening angle  $\alpha$  in an external magnetic field. (a) The apex of a sharp cone ( $\alpha/\alpha_c = 0.4$ ) remains superconducting for magnetic fields up to 4.3 T. (b) For a blunt cone ( $\alpha/\alpha_c = 3.2$ ) the superconducting part is more confined to the apex and the critical field is smaller ( $B_c = 1.27$  T).

well-defined and the increasing Zeeman splitting is clearly observable. In Fig. 4.13, the same calculation is shown for  $\alpha/\alpha_c = 3.2$ . The wider opening angle results in broadened spectra, where the separation of the spin-up and spin-down contributions is completely smeared out.

Due to the high computational cost related with the self-consistency equation (Eq. 4.3), the Usadel approach is unsuitable as a fitting routine for the experimental  $dI/dV$  spectra. However, for a more quantitative comparison of the experimental data with the calculations based on the Usadel equation, the fitting routine based on Maki's extended model is employed to analyze the calculated spectra with  $b = \zeta = 0$ , because spin-orbit coupling and orbital depairing only play a minor role in the Usadel approach. The fits are shown as dashed lines in Fig. 4.12 and Fig. 4.13. The superconducting gaps obtained from the Maki fits match the results obtained from the Usadel equation. The direct comparison is presented in Fig. 4.16 for a sharp tip, a blunt tip and a tip with the critical opening angle  $\alpha_c$ . It turns out that the fits for the calculated spectra also require the phenomenological parameter  $\Gamma$ . This represents an interesting observation because the geometrical confinement is the only origin for broadening effects in the Usadel equation. It indicates that the broadening in the experimental data is directly related to the conical confinement of the tip and justifies the use of the  $\Gamma$  parameter for the analysis based on the extended Maki model.

In Fig. 4.14, the magnetic field dependence of the superconducting gap  $\Delta$  is presented for several superconducting cones with varying opening angles  $0.2 \leq \alpha/\alpha_c \leq 4$ . Increasing  $\alpha/\alpha_c$  clearly decreases the critical field  $B_c$  of the cone. More importantly, at the critical field, the ratio  $\alpha/\alpha_c$  determines the order of the superconducting phase transition. Sharp cones with  $\alpha/\alpha_c < 1$  exhibit a first order phase transition to the normal state. That becomes most obvious for very sharp tips ( $\alpha/\alpha_c \ll 1$ ), when the superconducting gap  $\Delta$  remains almost constant up to the critical field where it abruptly vanishes and the cone becomes normal. Increasing  $\alpha/\alpha_c \rightarrow 1$ ,

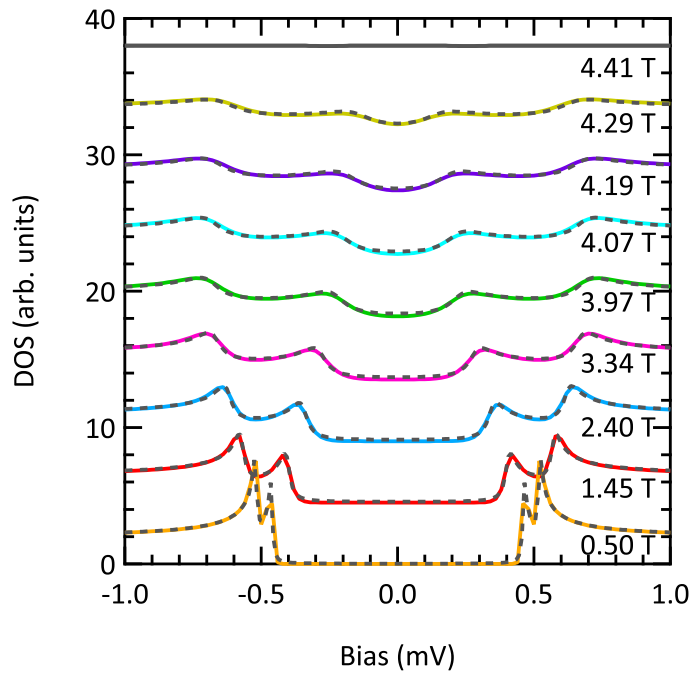


Figure 4.12: Superconducting quasi-particle DOS for  $\alpha/\alpha_c = 0.4$ . The DOS of the sharp tip exhibits clear spectral features and the lifted spin degeneracy is clearly visible due to the Zeeman energy.

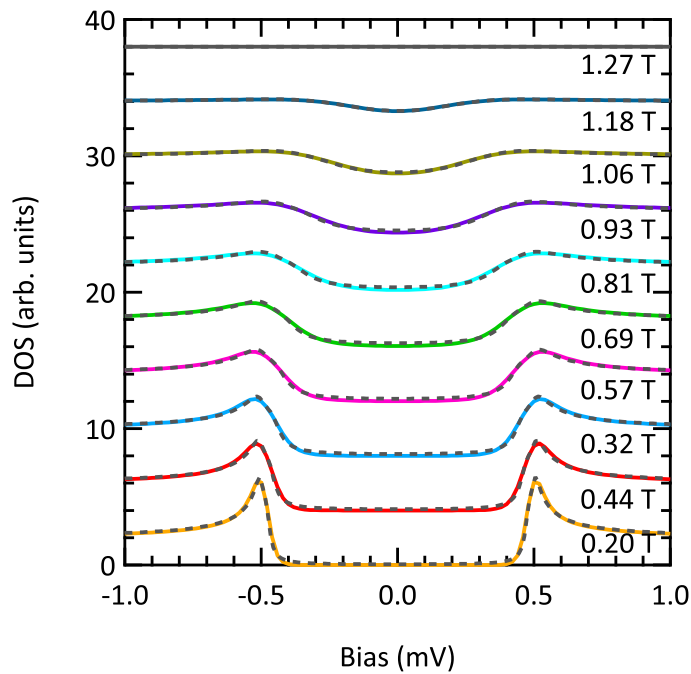


Figure 4.13: Superconducting quasi-particle DOS for  $\alpha/\alpha_c = 3.2$ . The DOS of the blunt tip appears more broadened.

#### 4.4. Magnetic Field Dependence of Superconducting Cones

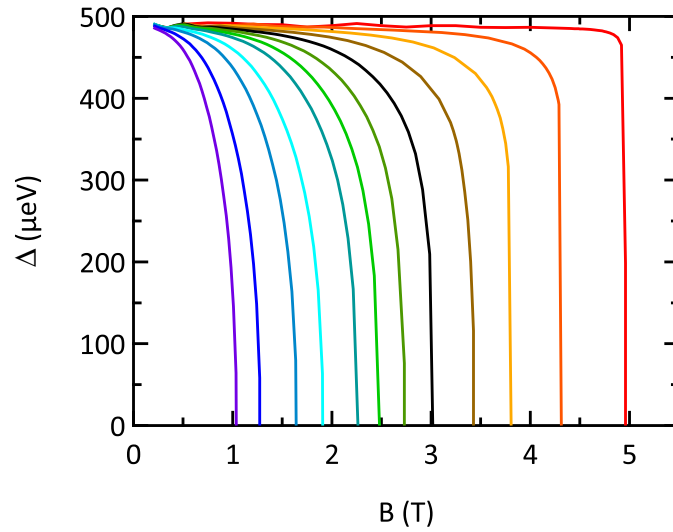


Figure 4.14: Superconducting gaps extracted by the extended Maki Model fit from the Usadel spectra. The magnetic field dependence of the superconducting gap  $\Delta$  is determined by the opening angle  $\alpha$ . For  $\alpha/\alpha_c < 1$ , the phase transition is of first order and for  $\alpha/\alpha_c > 1$  a second order phase transition is observed. The legend is given in Fig. 4.15.

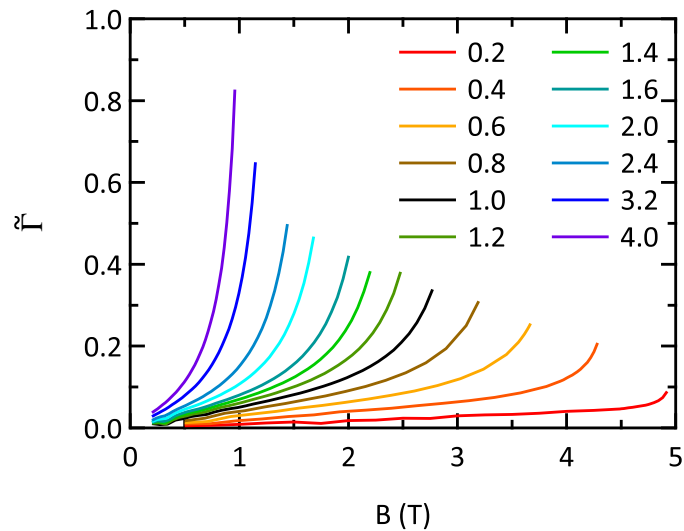


Figure 4.15: Broadening parameters extracted by the extended Maki Model fit from the Usadel spectra. The spectral broadening is described by the parameter  $\Gamma$ , which increases with  $\alpha$ . The numbers in the legend are the ratios of  $\alpha/\alpha_c$ .

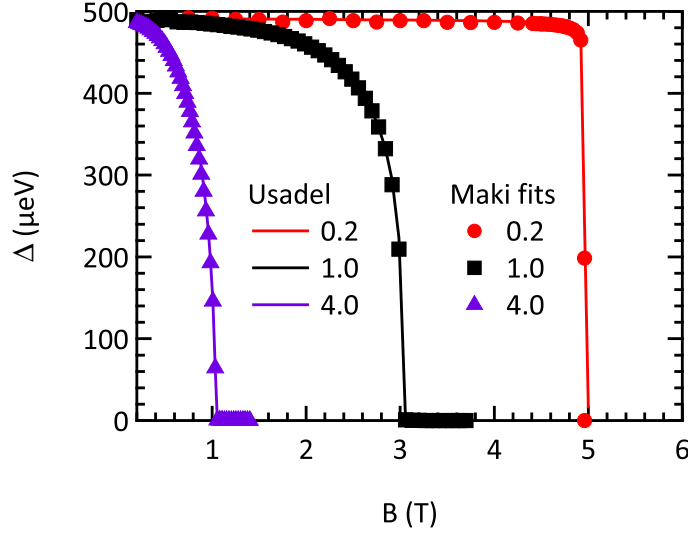


Figure 4.16: Comparison of the superconducting gaps obtained by the Usadel calculations and the Maki fits. The superconducting gaps for several opening angles  $\alpha/\alpha_c$  are numerically calculated as a function of the external magnetic field (lines). The corresponding superconducting quasi-particle DOS is fitted by the extended Maki model. The superconducting gaps extracted as fit parameter match the original Usadel calculations.

the superconducting gap decreases more rapidly at higher fields, but at the critical field, there is still the discontinuous drop of the superconducting gap to zero. Blunter tips with  $\alpha/\alpha_c > 1$  (but still  $\alpha \ll 1$ ) undergo a second order phase transition, in which the superconducting gap continuously decreases to zero. For a quantitative analysis of the spectral broadening, Fig. 4.15 shows the reduced Dynes parameter  $\tilde{\Gamma} = \Gamma/\Delta$  of the calculated quasi-particle DOS fitted by the extended Maki model as a function of the magnetic field. For all cones with opening angles  $0.2 \leq \alpha/\alpha_c \leq 4$ , good agreement with the fit function is obtained, i. e. the spectral broadening is well-described by the phenomenological parameter  $\Gamma$ . As already indicated in Fig. 4.12 and Fig. 4.13,  $\tilde{\Gamma}$  increases with the opening angle  $\alpha$ . More importantly, the rate of change  $d\tilde{\Gamma}/dB$  in the magnetic field is also a function of the opening angle. When increasing  $\alpha/\alpha_c$ , the spectral broadening becomes more sensitive to the external field and, therefore, the observation of features such as coherence peaks split by the Zeeman energy is more difficult.

## 4.5 Order of the Superconducting Phase Transition

The magnetic field dependence is investigated for superconducting V tips by STM (Sec. 4.2). The presence of geometrical confinement, orbital depairing and spin-orbit scattering makes characterizing the order of the superconducting phase transition difficult. Therefore, the tips are modeled as superconducting cones, for which the magnetic field dependence is derived from a 1D Usadel approach (Sec. 4.4). While the numerical Usadel calculations take into account the detailed geometry by the opening angle  $\alpha$ , the computational effort renders a



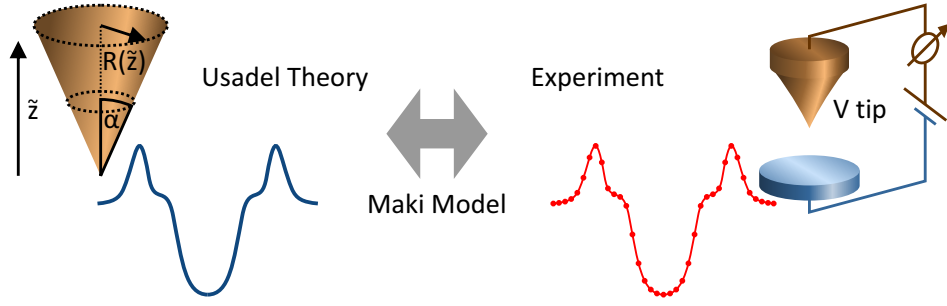


Figure 4.17: The extended Maki model as a link between Usadel calculations and experimental results. The extended Maki model is employed to fit both the experimentally acquired  $dI/dV$  spectra and the numerically calculated superconducting quasi-particle DOS. The procedure enables the implementation of findings from the Usadel calculations for the analysis of the experimental data, for example the first and second order phase transitions.

fit routine based on the Usadel approach difficult. This is mainly due to the fact that the numerical solutions require various iterations in order to fulfill the self-consistency equation (Eq. 4.3). The extended Maki model represents a possible work-around for this problem connecting the microscopic Usadel model and the STM experiment, as schematically shown in Fig. 4.17. Both the experimentally acquired and the numerically calculated superconducting quasi-particle DOS are fitted by the extended Maki model. This procedure allows for analysis of the experimental results considering the findings of the Usadel calculations, such as the first and second order of the phase transition. Furthermore, it turns out that the damping parameter  $\Gamma$  is directly correlated with the opening angle  $\alpha$  and the geometry, respectively (Fig. 4.15). In a simplified view, the  $\Gamma$  parameter represents a computationally inexpensive replacement for the detailed calculation of the full tip geometry.

For comparing the superconducting gaps obtained from the Usadel equation to the experimental findings in Fig. 4.18, the measurements and calculations are normalized to the zero-field gaps  $\Delta_0$  and critical fields  $B_c$ . The black line for  $\alpha/\alpha_c = 1$  marks the separation between phase transitions of first and second order. The comparison shows that the superconducting gaps of tip 1 lie in the region above the separation line and, therefore, tip 1 undergoes a phase transition of first order. For tip 2, the classification of the phase transition is ambiguous, since it is too close to the changeover from a first order to a second order transition. Tips 3 to 5 exhibit a second order phase transition, as already indicated by the continuously vanishing gaps (Fig. 4.4).

In Fig. 4.19, the rate of change  $d\tilde{\Gamma}/d\tilde{B}$  in the magnetic field is calculated for the Usadel results at lower magnetic fields ( $0.5B_c \leq B \leq 0.7B_c$ ), where a linear approximation is reasonable. The gray area indicates the results obtained when shifting the fitting range from  $0.45B_c \leq B \leq 0.65B_c$ , respectively, from  $0.55B_c \leq B \leq 0.75B_c$  and gives an error estimation for this approach.  $d\tilde{\Gamma}/d\tilde{B}$  is also extracted from the fits of the experimental data for the similar field range. While the opening angle of the V STM tips cannot be determined experimentally, comparing the experimentally obtained values of  $d\tilde{\Gamma}/d\tilde{B}$  to the Usadel calculations (line in Fig. 4.19) allows

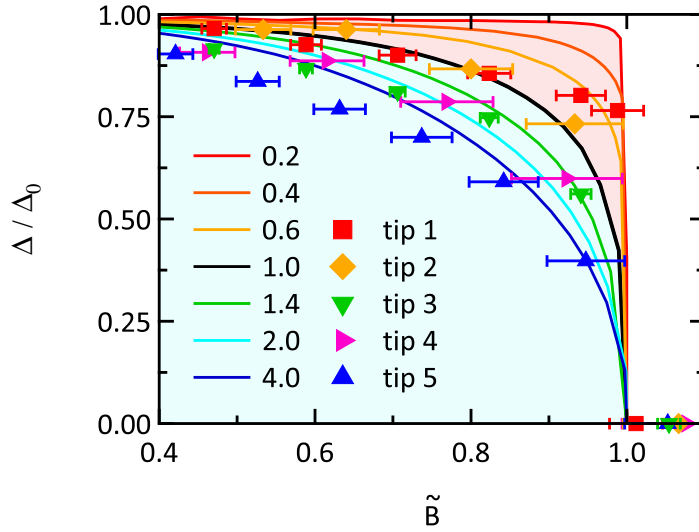


Figure 4.18: Comparison of the Usadel calculations and the experimentally obtained superconducting gaps. The normalized superconducting gaps  $\Delta/\Delta_0$  calculated by the Usadel equation (lines) as a function of the normalized magnetic field  $\tilde{B} = B/B_c$  exhibit first and second order phase transitions depending on the opening angle  $\alpha$ . The markers are the normalized experimental data from Fig. 4.4.

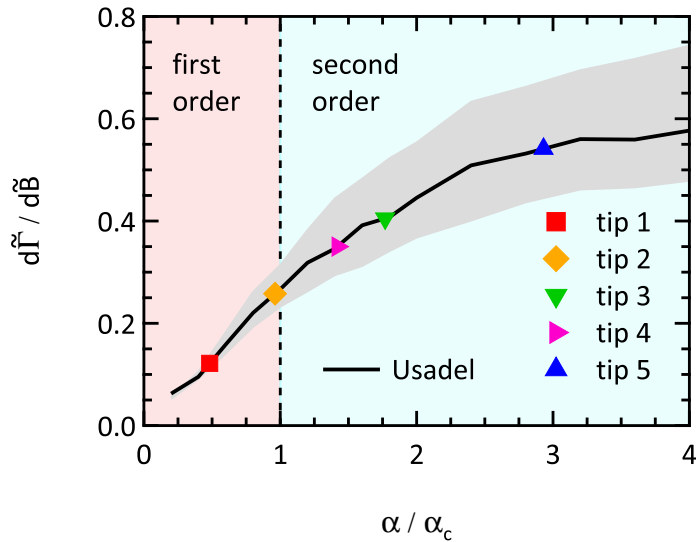


Figure 4.19: The rate of change of the broadening parameter  $\Gamma$  in a magnetic field allows for an additional classification of the superconducting phase transition in the V tips.

## 4.5. Order of the Superconducting Phase Transition

---

for an estimation of an effective  $\alpha/\alpha_c$ . This approach provides an additional independent parameter to characterize the order of the superconducting phase transition. Again, it shows that tip 1 undergoes a first order phase transition. The order of the transition in the second tip cannot clearly be characterized within the error estimation, but tips 3 to 5 are clearly in the regime where  $\alpha/\alpha_c > 1$ , indicating a second order phase transitions. Therefore, the findings of the field dependence of the broadening parameter confirm the characterization of the phase transition by the superconducting gaps (Fig. 4.18).

The phase transitions of superconducting V STM tips are investigated for various geometries in magnetic fields at low temperatures. Solving an effective 1D Usadel equation, the direct correlation of the cone geometry and the order of the superconducting phase transition is revealed; first order for very sharp tips ( $\alpha < \alpha_c$ ) and second order for blunter tips ( $\alpha > \alpha_c$ ). The microscopic approach provides a physical interpretation for the experimentally observed broadening of the  $dI/dV$  spectra and sheds light on the origin of the phenomenological parameter  $\Gamma$  introduced to fit the data by the extended Maki model. This parameter is not directly related to any microscopic pair-breaking but is a formal way to cure the inapplicability of the Maki model to systems with non-uniform superconductivity resulting from geometrical confinement and external magnetic fields. So far,  $\Gamma$  has been employed as a phenomenological description of various systems and the study of the superconducting tips represents a novel point of view on its microscopic origin. For experimental applications, the detailed understanding of the superconductivity in the cone geometry is essential. The investigations facilitate the application of superconducting STM tips in the presence of an external magnetic field as an additional tuning parameter, which enables techniques such as Meservey-Tedrow-Fulde STM (Chap. 5) or Josephson STM [97, 101, 112, 113]. Both techniques greatly benefit from clearly distinguishable spectral  $dI/dV$  features, e. g. for resolving the Zeeman splitting and probing absolute spin polarization (Chap. 5). The combination of Josephson STM with external magnetic fields enables a wide range of additional experiments, such as single electron spin resonance measurements [114, 115]. The findings suggest that both techniques benefit from superconducting tips with small opening angles ( $\alpha \ll \alpha_c$ ) resulting in small broadening ( $\Gamma \ll \Delta$ ) and first order phase transitions at high critical fields ( $B_c \gg B_{c,\text{bulk}}$ ).



# 5 Probing Absolute Spin Polarization at the Nanoscale

In this chapter, a novel approach is presented to quantitatively probe spin polarization at the nanoscale. For this purpose, the MTF technique (Sec. 3.3) is transferred to STM by employing the superconducting V tips characterized in Chap. 4. The approach combines the quantitative probing capability for spin polarization with precise control at the atomic scale and the well-defined vacuum tunnel barrier of the STM. To demonstrate the virtues of the new technique, the local spin structure of a Co nanoisland is spatially resolved with an absolute scale for the spin polarization. Furthermore, variations of the spin polarization up to 65 % are found when changing the tip-to-sample distance by only 2.3 Å, which can be related to a different decay of the spin-up and spin-down wave functions into vacuum. In part, the chapter has already been published in Ref. 97.

## 5.1 Overview and Motivation

Many modern technological advances such as magnetic hard drives utilize spin-polarized tunnel currents [116, 117]. Detecting the spin polarization of tunneling electrons does not only offer insight into the underlying mechanisms of spin-dependent transport but is also essential for novel concepts in spintronics, which employ spin-dependent tunneling on the molecular or even on the atomic scale [118–121]. In this context, spin-polarized scanning tunneling microscopy (SP-STM) represents a versatile tool providing detailed information about the spin properties as well as of the surface topology. In SP-STM, the spin-sensitive signal results from the tunnel magnetoresistance effect, which, in the simplest description is proportional to the product of the local spin polarization of the sample and the tip [64, 122]. While SP-STM with (anti-)ferromagnetic tips provides information of the relative spin orientation in the sample, direct conclusions concerning the absolute values of spin polarization are difficult due to the unknown electronic structure of the STM tip (Sec. 5.5). However, absolute values are desirable, for example, when comparing the efficiency of multiple spin-dependent transport channels or spin-filter systems at the atomic scale. For mesoscopic systems such as planar thin film tunnel junctions, the quantitative probing capability for absolute spin polarization is provided by the MTF effect (Sec. 3.3). A major drawback in thin film tunnel junctions is the lack of local

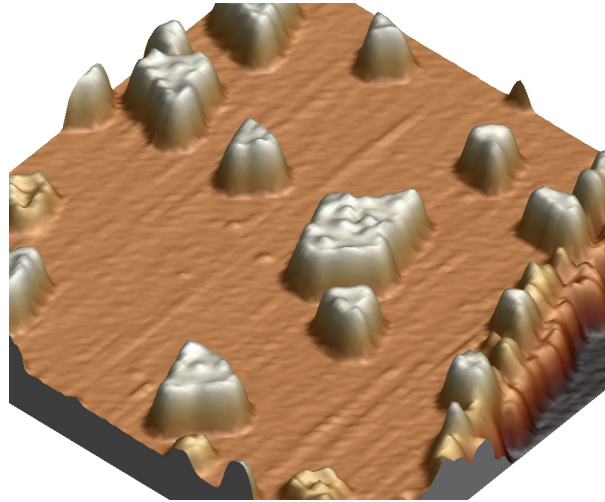


Figure 5.1: STM image of Co nanoislands on Cu(111) (scan range  $60\text{ nm} \times 60\text{ nm}$ ,  $I_T = 50\text{ pA}$  and  $V_T = 1\text{ V}$ ). In the sub-monolayer coverage regime, Co forms bilayer nanoislands on the Cu(111) surface. The orientation of the triangular shapes is the direct result of the stacking order.

resolution, as the measured signal is averaged over the whole area of the tunnel junction. As spin transport is influenced by variations on the atomic scale, it is thus desirable to combine the absolute probing capabilities of the MTF effect with the local resolution capabilities of the STM. In addition, as the tunnel barrier of the STM is vacuum — the most ideal, defect free and spin neutral barrier — the magnetic structures can be measured directly. This avoids the potential influence of the insulating barrier material on the spin transport through a matching of the electronic structure at the interface or the spin polarizing properties of the barrier material itself.

The capability to probe absolute values of spin polarization is transferred to STM employing the Zeeman split superconducting DOS of V tips. As a first demonstration of this novel technique, the spin polarization of a magnetic nanostructure is quantitatively resolved with atomic scale control. Furthermore, a direct correlation is reported for electron orbitals decaying into the tunnel barrier and the resulting spin polarization of the tunneling electrons.

### 5.2 Cobalt Nanoislands on Copper

For the evaluation of a novel STM technique, Co nanoislands on the Cu(111) surface represent an ideal test system, which has been subject to intense research, for example by SP-STM and calculations based on density functional theory (DFT) [123–128]. Originally, thin Co films on Cu were considered as a highly promising candidate for magnetic storage media with perpendicular crystal anisotropy [129]. While the small lattice mismatch ( $-1.9\%$ ) enables epitaxial growth, the high surface energy of Co with respect to Cu hampers the formation of smooth Co monolayers [130]. Instead, Co forms three-dimensional nanoislands on the Cu

### 5.3. Meservey-Tedrow-Fulde Scanning Tunneling Microscopy

---

surface. These islands are of bilayer height and form triangular structures, as shown in Fig. 5.1. Two opposite orientations of the triangular shapes are observed. While the majority of the structures follow the fcc stacking of the Cu substrate, a minority are rotated by  $180^\circ$ , as the result of a stacking fault [124, 131]. The stacking order directly effects the electronic properties and shifts the characteristic spectral features [124]. In general, two electronic main features have been identified in STM studies [123, 124]. A majority state formed by *sp*-electrons was found by a combined study of STM and DFT calculations. Analyzing the Friedel oscillations in the LDOS reveals that the dispersion relation of the majority state is similar to the dispersion of free electrons. Furthermore, an additional minority state of *d* character is found giving rise to an additional peak in the LDOS below the Fermi level [123].

The overall magnetization of the Co nanoisland points out-of-plane due to the perpendicular easy axis of the magneto-crystalline anisotropy (Sec. 2.2.1). On the Co surface, the majority state dominates the electronic structure in the inner regions of the Co nanoisland at the Fermi level, which results in a positive spin polarization [125, 127, 128]. The rim is mostly governed by the minority state creating negative spin polarization due to the more localized character of the *d*-electrons [125, 127, 128]. In addition, the triangular Co islands serve as geometrical confinement for less localized electrons. Due to reflection at the boundaries, the majority surface state forms standing wave patterns. The quantum interference results from the complex interplay of the majority and minority state. As a result, the spin polarization at the Co surface changes its sign and magnitude on the sub-nanometer scale [127, 128].

For the sample preparation, the Cu(111) sample is cleaned in several cycles of Ar<sup>+</sup> ion sputtering and annealing to approximately 600°C for several minutes. Co is deposited in sub-monolayer coverage at room temperature by using an electron beam evaporator. Under these conditions, Co forms the bilayer islands of triangular shape as described above. After being transferred to the STM unit without breaking the UHV, the sample is cooled to 15 mK for the measurements.

### 5.3 Meservey-Tedrow-Fulde Scanning Tunneling Microscopy

The superconducting V tips characterized in Chap. 4 are used for probing absolute values of the spin polarization at the atomic scale.<sup>1</sup> In comparison to the original experiments carried out by R. Meservey and P. M. Tedrow (Sec. 3.3), the STM tips replace the thin film superconductor as the electrode and the isolating layer of the sandwich tunnel junction is realized by the vacuum tunnel barrier of STM (Sec. 3.1). In the following, the approach is referred to as MTF-STM.

---

<sup>1</sup>As described in Sec. 4.2, the STM tips are prepared by field emission and voltage pulses on the V(100) sample. Since picking-up Co and Cu suppresses the superconducting properties of the V tips, the preparation is carried out on the V(100) surface, which is afterward replaced by the Cu(111) sample with the Co islands. Mechanical contact between tip and sample usually destroys the superconductivity in the tip requiring a new tip preparation. Successfully transferring a V tip suitable for the MTF technique to the Cu sample has been one of the most time-consuming experimental challenges.

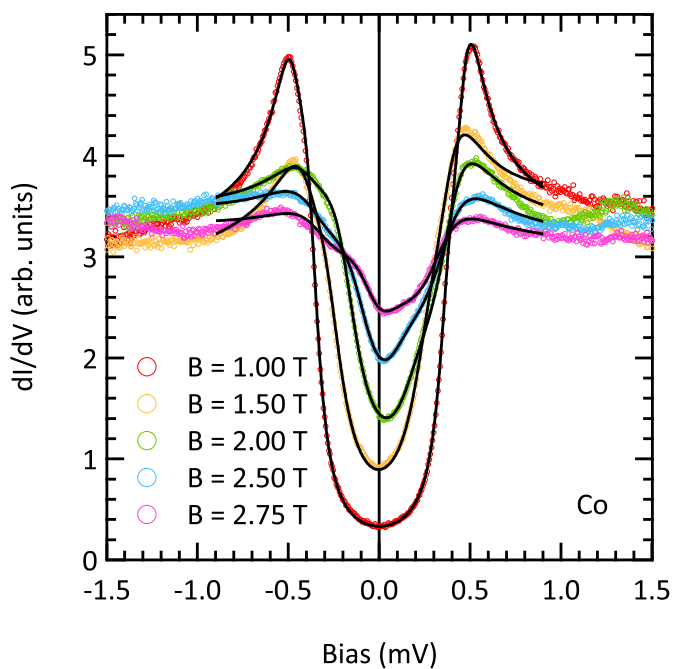


Figure 5.2:  $dI/dV$  spectra measured on the center region of a Co nanoisland with a superconducting V tip. The asymmetry stems from the spin polarization of the tunneling electrons, which is analyzed by fits based on the extended Maki model (lines).

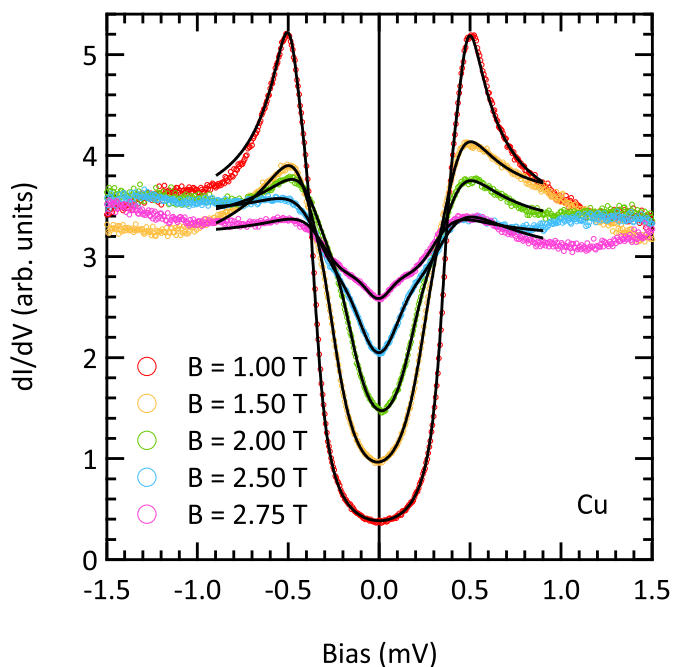


Figure 5.3:  $dI/dV$  spectra measured on the bare Cu surface. The same superconducting tip as in Fig. 5.2 is used for a reference measurement. The resulting  $dI/dV$  spectra show no asymmetry indicating that the electrons tunneling from the Cu surface are not spin-polarized.



In Fig. 5.2,  $dI/dV$  spectra are measured on a Co island with a superconducting V tip. At the measuring temperature of 15 mK, all spectra feature superconducting quasi-particle DOS for magnetic fields up to 2.75 T. More importantly, the conductance measurements show a clear asymmetry due to the imbalance between the tunneling spin-up and spin-down electrons. For this particular superconducting tip, the critical field ( $B_c \approx 3$  T) is lower and the spectral features appear more broadened than the measurements with the tip presented in Fig. 4.1. As discussed in Chap. 4, both findings are attributed to the influence of the tip geometry. Instead of the characteristic four-peak-structure of the superconducting coherence peaks, the lifted spin degeneracy is only visible in the formation of a shoulder in the  $dI/dV$  spectra, which becomes clearly visible at the gap edge with increasing magnetic field. In order to analyze the spin polarization of the tunneling electrons, the spectra are fit by the extended Maki model (lines in Fig. 5.2). The model reveals its full strength for the broadened spectral features, which would make the use of the simpler method based on four different  $dI/dV$  values difficult (Eq. 3.18). In contrast, the spectral broadening does not hamper a detailed analysis of the spin polarization by the Maki fits and absolute values can still be derived with high accuracy as will be discussed in the following. The spectral broadening only slightly increases the error bars as discussed below. Furthermore, Maki's theory includes a spin-orbit related mixing of the spin channels in magnetic fields that also effects the differential conductance measurements (Sec. 3.3.2). Although the spin-orbit interaction is still rather small, this term needs to be included to minimize the error bar on the extracted spin-polarization. As a reference, differential conductance spectra are measured with the same superconducting V tip on the bare Cu(111) surface in Fig. 5.2. The lines in Fig. 5.2 represent fits to the data using the extended Maki model (Sec. 3.3.2). While the critical field and the overall broadening of the spectral features are similar to the measurements shown in Fig. 5.2, the  $dI/dV$  spectra appear symmetric, indicating that the DOS on the Cu(111) surface is not spin-polarized.

In addition to the experiments presented in Fig. 5.2 and Fig. 5.3, the measurements are repeated for the reversed orientation of the external magnetic field. For both field orientations, the investigated magnet fields surpass the coercivity of the Co island. In Fig. 5.4(a), the superconducting gaps and the Zeeman splitting are extracted by the Maki fits from the  $dI/dV$  spectra. In general, neither the superconducting gap nor the Zeeman splitting depend on the orientation of the magnetic field. For both field directions, the superconducting gap decreases with increasing magnetic field until the tip becomes normal conducting at the critical field ( $B_c \approx 3$  T). The comparison with the numerical calculations carried out in Chap. 4 reveals that the tip clearly undergoes a second order phase transition (Fig. 5.4(b)). For this particular tip, the magnetic field dependence clearly indicates that the effective opening angle exceeds the critical angle  $\alpha_c$  (Chap. 4). In fact, the behavior is similar to the numerical calculations carried out for the largest opening angle  $\alpha/\alpha_c = 4$ . While tips with smaller effective opening angles show less spectral broadening (Fig. 4.19) and generally provide better detecting capabilities, this particular tip is still suitable to analyze the spin polarization of the tunneling electrons with acceptable error estimations as discussed below. The extracted superconducting gaps as well as the Zeeman splitting lead to similar results for measurements on Co and Cu. This

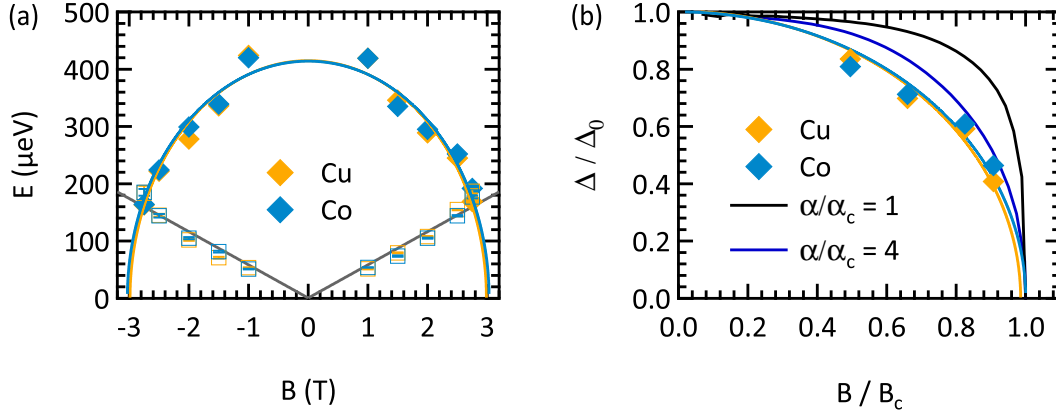


Figure 5.4: Superconducting gaps and Zeeman splitting of a V tip measured on a Co nanoisland and on the Cu(111) surface. (a) The magnetic field dependence of the superconducting gap (markers) and the Zeeman splitting (lines) are not effected by the Co. These results are independent of the magnetic field orientation (parallel or antiparallel to the tip axis). (b) The magnetic field dependence of the superconducting gap is compared to the numerical calculations discussed in Chap. 4, which reveals the second order phase transition.

finding indicates that the superconductivity of the tip is not effected by the stray fields of the Co island. On the one hand, the external magnetic field is considerably enhanced directly above the top Co layer, which should effect the superconducting tip apex. On the other hand, the stray field is locally confined to the small Co nanoisland and, most likely, does not reach most of the superconducting regions in the tip. The fact that the stray field can be neglected on the superconducting length scales distinguishes MTF-STM from most other conventional STM techniques, where the measurements are usually governed by the properties of the last atoms at the tip apex (Sec. 3.1.2).

The asymmetry of the  $dI/dV$  spectra stems from the spin polarization of the tunneling electrons. The imbalance between spin-up and spin-down electrons is depicted in Fig. 5.5 for a Co nanoisland and the bare Cu(111) surface as a reference. For Co, the analysis based on the extended Maki model reveals a high spin polarization of  $54 \pm 4\%$  (Fig. 5.5(a)), which means that the tunnel current consists of 77% spin-up and 23% spin-down electrons.<sup>2</sup> This finding illustrates that the MTF technique is only sensitive to the spin polarization of the electrons at the Fermi level ( $P(E_F)$ ). For magnetic fields larger than the coercive field of the Co nanoisland, the stable magnetization configuration demands parallel alignment of the magnetic fields to the external field lines. In this case, one would actually expect negative overall spin polarization of the Co nanostructure with respect to the external field because the spin points opposite to the magnetic moment (Sec. 2.2.1). As a reference the same analysis is shown for the Cu(111) surface in Fig. 5.5(b). The fit based on the Maki theory reveals a negligible spin polarization of

<sup>2</sup>The correlation between the spin polarization and the amount of tunneling electrons for each spin orientation is given by Eq. 3.19 and Eq. 3.20 as  $P = 2N_{\uparrow} - 1$  with  $N_{\uparrow} + N_{\downarrow} = 1$ .

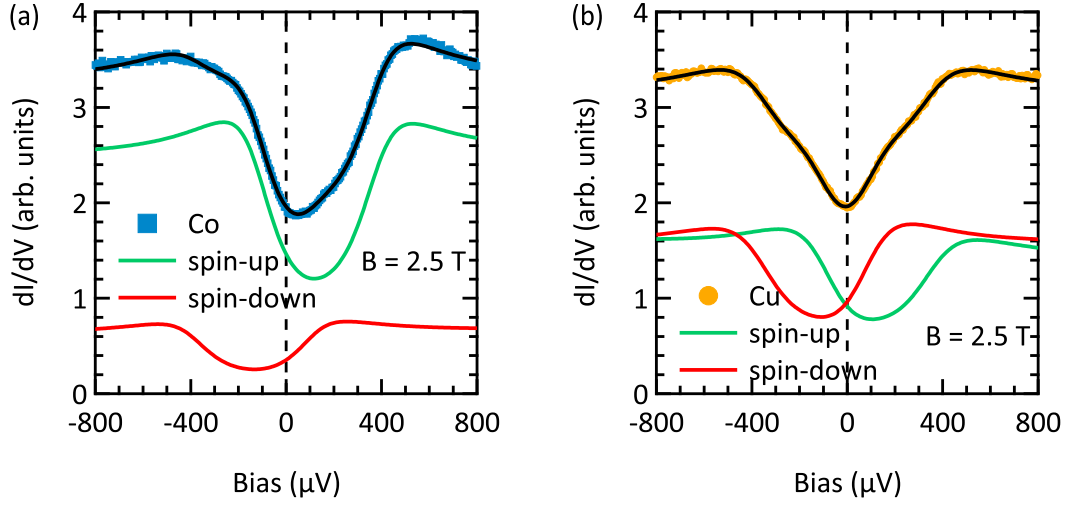


Figure 5.5: Contributions of spin-up and spin-down electrons to the tunnel current. (a) The  $dI/dV$  spectrum measured on the Co island is asymmetric due to the spin polarization of the tunneling electrons. The spin-up and the spin-down contributions are extracted from the Maki fit. (b) The spin polarization of the tunneling electrons is negligible for the Cu(111) surface resulting in equal contributions of spin-up and spin-down electrons.

$0 \pm 2\%$ . Accordingly, the tunnel current consists of 50 % spin-up and 50 % spin-down electrons (Fig. 5.5(b)). This ability to probe the absolute spin polarization with MTF-STM goes beyond conventional SP-STM, relying on the tunnel magnetoresistance effect between two magnetic electrodes [122]. A more detailed comparison of these approaches is presented in Sec. 5.5.

In Fig. 5.6(a), differential conductance spectra are measured for a larger voltage range. In addition to the superconducting gap, the LDOS also shows features for higher energies in the normal conducting regime. Since the features differ in both energy position as well as intensity for measurements on Co and Cu, they probably stem from the substrate and thus tip effects can be excluded. Furthermore, the additional states are effected by the external magnetic field (Fig. 5.6(b)). In general, the observed states occur on energies, which are in the order of the superconducting gap. For metal samples, such behavior is not expected and contradicts the approximations made in the MTF technique. It assumes a constant DOS for the normal metal electrode in order to calculate the resulting conductance (Sec. 3.3). In part, these effects are compensated by the fit routine subtracting linear and constant offsets.

To gain insight into the local variation of spin polarization, more than one thousand  $dI/dV$  spectra are acquired on the Co island shown in Fig. 5.7(a). The superconducting gap  $\Delta$  (Fig. 5.7(b)) as well as the broadening parameter  $\Gamma$  (Fig. 5.7(c)) are extracted from the differential conductance measurements as described before. When employed as free fit parameters,  $\Delta$  and  $\Gamma$  show small variations due to the topography of the Co nanoisland. For example,  $\Delta$  appears slightly increased at the edge of the island, where additional tunneling channels might open due to the specific geometries of tip and sample. Furthermore,  $\Delta$  and  $\Gamma$  can be altered by the

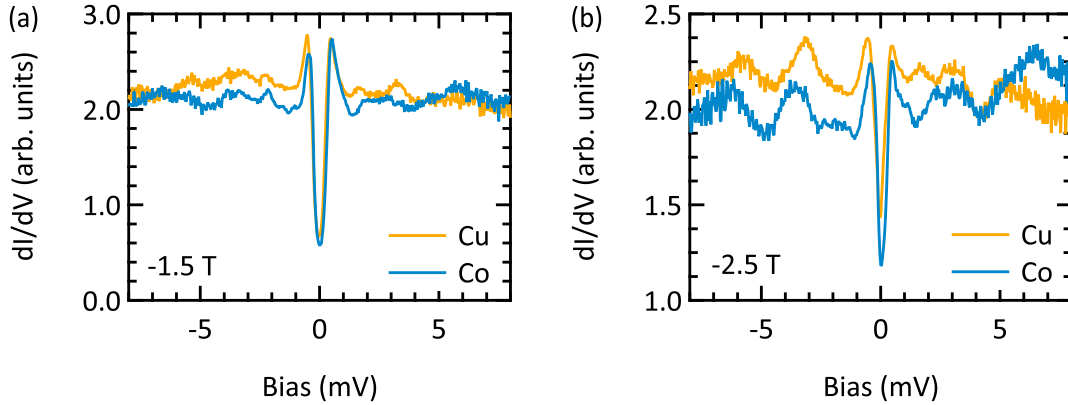


Figure 5.6:  $dI/dV$  spectra obtained on Cu and Co for larger voltage ranges. (a) Besides the superconducting gap, additional electronic features are observed in the LDOS on Co and Cu. (b) These states also depend on the external magnetic field.

fitting procedure within certain limits due to the broadening of the  $dI/dV$  spectra. As discussed below, these small variations are considered for the error estimation of the spin polarization.

The Maki analysis of the differential conductance spectra reveals locally resolved absolute values of the spin polarization. The resulting map for the investigated part of the Co nanoisland is presented in in Fig. 5.7(d). Negligible spin polarization ( $0\% < P < 2\%$ ) is obtained on the bare Cu surface, meaning that the substrate electrons are not polarized within the error estimation. The inner region of the Co island is governed by the surface state of the majority  $sp$ -electrons and shows positive spin polarization. The rim state at the outer region of the Co island is formed by the minority  $d$ -electrons exhibiting negative spin polarization [127]. These findings, as well as the observed variations within the rim state at the Fermi level, are in good agreement with previous investigations [124–128]. Employing the quantitative scale of MTF-STM, negative spin polarization down to  $-56 \pm 5\%$  is found at the outer region and positive polarization up to  $+65 \pm 5\%$  around the center position of the Co island. In Fig. 5.7(e) and (f), the tunnel current is separated into the contributing spin-up and spin-down electrons. In Fig. 5.7(e), the transport is dominated by spin-up electrons due to the majority surfaces state in the center region of the Co nanoisland. More importantly, the rim regions showing negative spin polarization almost completely lack the presence of spin-up electrons, emphasizing that the spin separation in the nanostructure occurs within sub-nanometer length scales. The corresponding behavior is observed for the spin-down electrons (Fig. 5.7(f)). Here, the bright red rim region corresponds to the negative spin polarization. At the center of the Co nanoisland, the spin-down channel almost completely vanishes, which gives rise to the high positive spin polarization. The measured spin polarization is about a factor of two higher than the spin polarization above the Co island calculated from DFT (Sec. 5.2) [126, 127]. This underlines the influence of the tunnel barrier, which is discussed in Sec. 5.4.

In order to estimate the errors of the absolute values of spin polarization, the extraction process

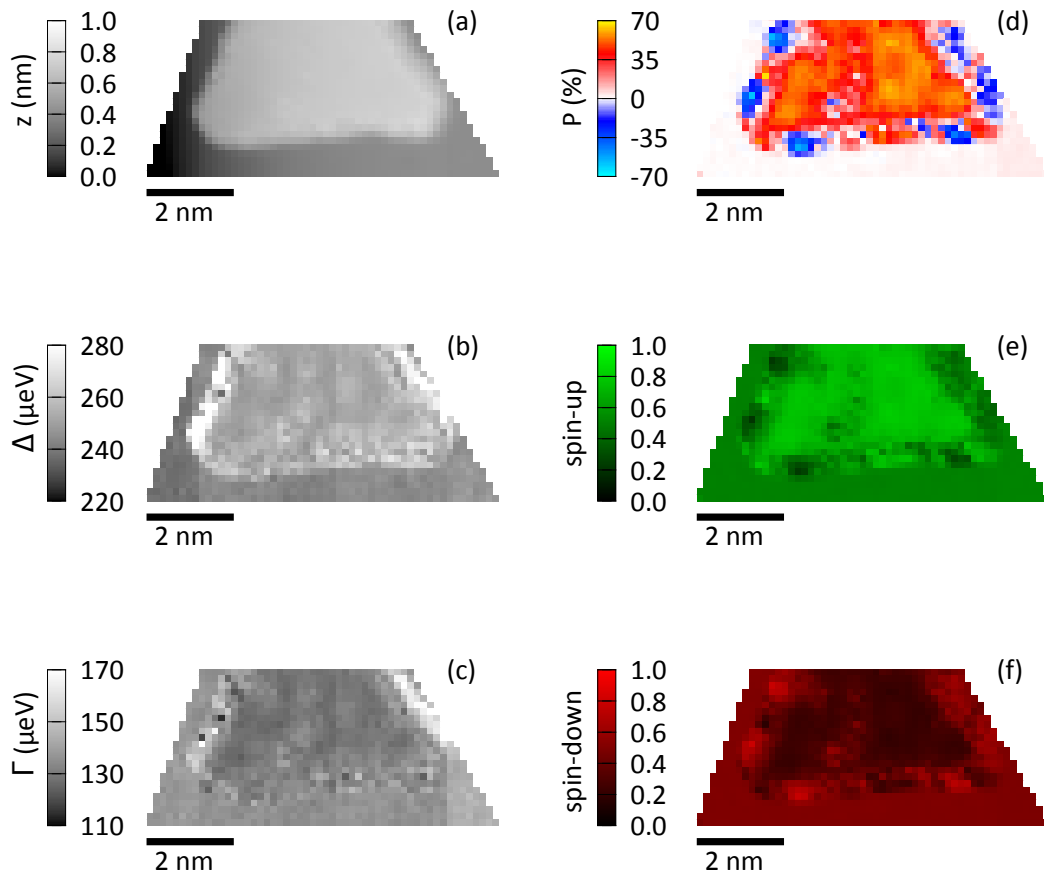


Figure 5.7: Probing absolute values of spin polarization at the nanoscale. (a) Lower part of a triangular Co island, on which more than one thousand  $dI/dV$  spectra are acquired. The  $z$  values are recorded at the stabilizing conditions ( $I_S = 500$  pA and  $V_S = 2.5$  mV). (b) The superconducting gap  $\Delta$  and (c) the broadening parameter  $\Gamma$  are extracted from the  $dI/dV$  spectra by the extended Maki model. (d) Positive spin polarization up to  $+65 \pm 5\%$  is found around the center position of the Co island and negative values down to  $-56 \pm 5\%$  are extracted at the outer region. On the Cu(111) surface, the obtained spin polarization is negligible ( $0\% < P < 2\%$ ). (e) The spin-up and (f) spin-down contribution of the tunnel current are separated revealing the regions dominated by each spin orientation.

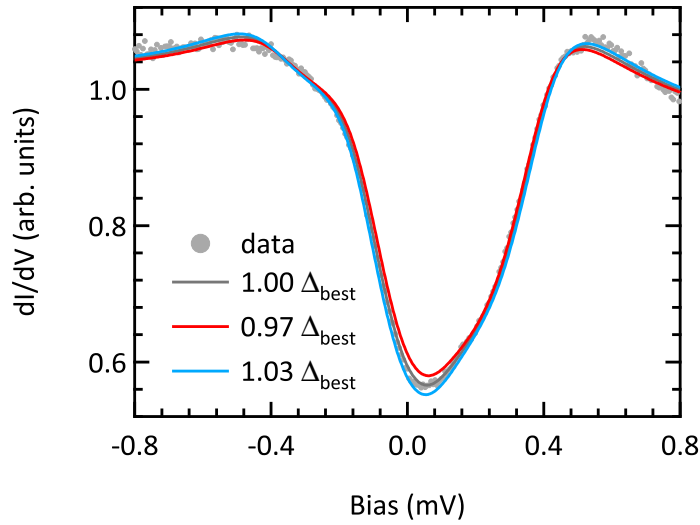


Figure 5.8: Error estimation for the fitting routine performed by varying the superconducting gap. For the  $dI/dV$  spectrum with 54% spin polarization, the superconducting gap  $\Delta$  is increased (or decreased) by 3% and the fitting routine is run to optimize the differential conductance by varying  $P$ .

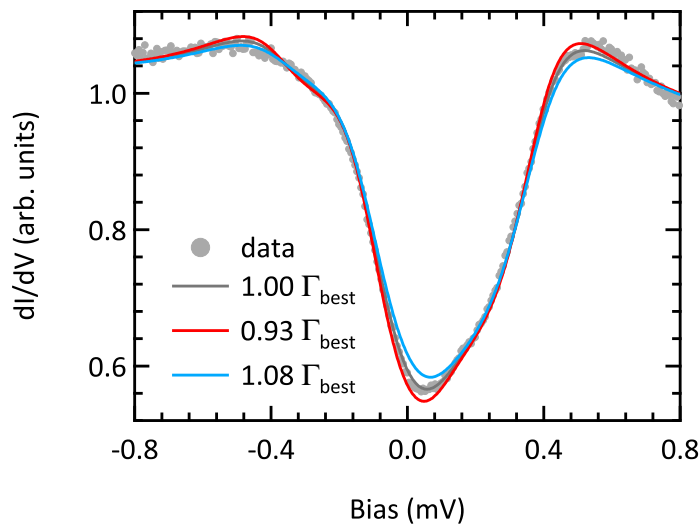


Figure 5.9: Error estimation for the fitting routine performed by varying the broadening parameter. The same calculations as in Fig. 5.8 are repeated for the damping parameter  $\Gamma$ . The broadening parameter  $\Gamma$  is increased (or decreased) by 3% and the fitting routine optimizes the differential conductance by varying  $P$ .

for the spin polarization from the differential conductance measurements is discussed in more detail for the MTF technique. Originally, R. Meservey and P. M. Tedrow used a simple method based on four different  $dI/dV$  values (Sec. 3.3), however, the approach leads to incorrect results in the presence of spin-orbit coupling, as demonstrated in Ref. 54. In this context, the choice of V as a material is important because its rather low spin-orbit coupling already reduces the spin mixing in magnetic field, which is analyzed by the extended Maki model. From the fit routine, the spin-orbit coupling parameter  $b = 0.14$  is obtained for the  $dI/dV$  measurements on Cu. This result is in good agreement with experiments carried out on thin film sandwich tunnel junctions [132]. Since the spin-orbit mixing is a property of the superconducting V tip,  $b$  is kept constant in the fit routine for all differential conductance spectra. The orbital depairing parameter is handled accordingly and best fits are achieved for  $\zeta = 0.05$  on Cu. Keeping  $b$  and  $\zeta$  constant provides not only good agreement of the fits with the data but also decreases the convergence time for the entire fit procedure. In addition, small known bias offsets are corrected in the  $dI/dV$  spectra and a linear background is subtracted. The spin polarization is then mainly influenced by the superconducting gap  $\Delta$  and the broadening parameter  $\Gamma$  and, therefore, the error estimation focuses on these two parameters in the following. A single fitting parameter (such as  $\Delta$ ) is varied so that it deviates on purpose from the ideal fitting value. Keeping this parameter fixed the fitting routine is run and the resulting spin polarization is evaluated. In Fig. 5.8,  $\Delta$  is fixed to a value increased (or decreased) by 3 % from the best fitting result ( $\Delta_{\text{best}}$ ) and the fitting routine is run to optimize  $P$ . Even these small deviations significantly alter the resulting  $dI/dV$  spectra and the quality of the fits is significantly decreased ( $\chi^2$  increases by six orders of magnitude). The resulting spin polarization is increased (or decreased) by 1 %. In Fig. 5.9,  $\Gamma$  is varied similar to the previous calculations for  $\Delta$  ( $\chi^2$  increases in the same range). The resulting spin polarization is changed by 5 %. Considering the good agreement between the fits and the experimental data, the deviations discussed in Fig. 5.8 and Fig. 5.9 are regarded as the upper limit. Assuming negligible correlation between  $\Delta$  and  $\Gamma$  allows calculation of the total error propagation of the spin polarization, which leads to the error estimation discussed before.

The calculations for the error estimation (Fig. 5.8 and Fig. 5.9) are repeated for several differential conductance measurements corresponding to spin polarizations of  $-56\% \leq P \leq 65\%$ . In Fig. 5.10(a), the superconducting gap is varied by  $0.7\Delta \leq \Delta_{\text{best}} \leq 1.3\Delta$  from the best fitting result  $\Delta_{\text{best}}$ . The value for the superconducting gap is fixed and the fit routine optimizes the spin polarization  $P$  to find the best fitting solution. When increasing  $\Delta$ , the absolute value of the spin polarization decreases. The calculations are also carried out for the broadening parameter  $0.7\Gamma \leq \Gamma_{\text{best}} \leq 1.3\Gamma$  (Fig. 5.10(b)). Here, the absolute values of the resulting spin polarization increases with increasing  $\Gamma$ . When the spectral broadening is even more dominant than in the  $dI/dV$  measurements shown in Fig. 5.2 and Fig. 5.3, the fitting routine tends to compensate for the too large values for  $\Delta$  by increased  $\Gamma$  values in some cases. The findings presented in Fig. 5.10 suggest that the effects on the spin polarization might still be tolerable and that superconducting tips with more spectral broadening might still offer acceptable accuracy. While the calculations presented in Fig. 5.10 demonstrate the direct correlation

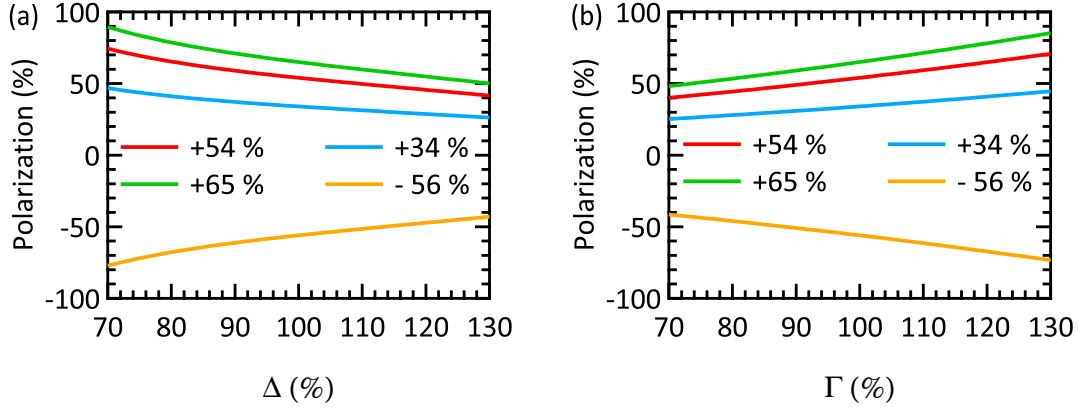


Figure 5.10: Resulting spin polarization when varying the superconducting gap or the broadening parameter. (a) The superconducting gap is varied by  $0.7\Delta \leq \Delta_{\text{best}} \leq 1.3\Delta$  from the best fitting result  $\Delta_0$ . The resulting spin polarization is a monotonic function of the varied parameter. (b) The calculations are repeated for the broadening parameter varied by  $0.7\Gamma \leq \Gamma_{\text{best}} \leq 1.3\Gamma$ .

between the fitting parameters  $\Delta$ ,  $\Gamma$  and  $P$  for a larger range, in practice, varying  $\Delta$  or  $\Gamma$  by only  $\pm 5\%$  already considerably decreases the quality of the fits.

### 5.4 Spin-filtering by Vacuum

Spin-dependent tunneling allows creation and detection of spin-polarized currents. For example, the tunnel magnetoresistance is the direct result of spin-dependent transport in magnetic tunnel junctions [64–66]. Though exploited in many applications, the contributions from the electrodes and the tunnel barrier are highly debated and difficult to separate. While in Jullière’s first theoretical description [64], the spin polarization is only determined by the imbalanced DOS for the spin-up and spin-down electrons in ferromagnetic electrodes (Fig. 5.11(a)), the tunnel barrier has tremendous effects on the spin polarization as well. Barrier materials such as EuS [133, 134] or MgO [116, 117] have intrinsic properties that lead to spin-filtering due to a spin-dependent decay of the electronic states (Fig. 5.11(b)). However, the spin-dependent decay does not require any intrinsic properties of the barrier. In a ferromagnet, the electronic states at a given energy are different for majority and minority electrons due to exchange splitting. Therefore, these states decay differently in any tunnel barrier, even in vacuum (Fig. 5.11(c)). While this mechanism provides the most versatile means for tuning the spin polarization of tunneling electrons, it is experimentally difficult to distinguish from competing effects such as the electronic structure of the tunnel barrier. In fact, decreasing as well as increasing spin polarizations have experimentally been observed as a function of barrier thickness and have been ascribed to the influence of the characteristic decay of electronic wave functions [135, 136]. Unequivocally measuring the correlation of spin polarization and the specific decay of electronic states requires, first, control of the



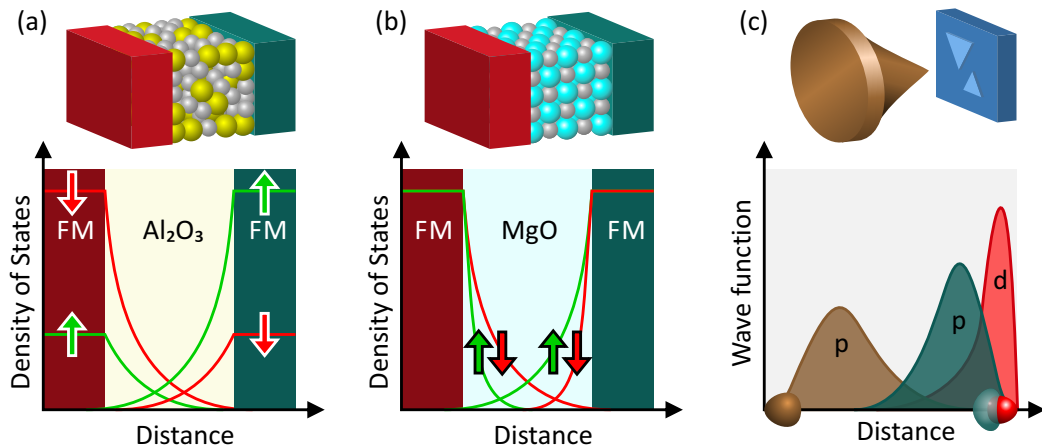


Figure 5.11: Schematic illustrations of the basic influences on the spin polarization of tunneling electrons. (a) In Jullière's model, the spin polarization does not depend on the width of the tunnel barrier. The asymmetry of spin-up and spin-down states provided by the ferromagnetic electrodes creates the spin-polarized tunnel currents. (b) Tunnel barriers such as MgO generate spin polarization of the tunneling electrons due to symmetry filtering. Here, the spin-polarization depends on the width of the tunnel barrier. (c) The specific decay of atomic orbitals is directly correlated with the tunneling probability for the electrons. If the spin states occupy different orbitals the tunnel current is spin-polarized. Since these electronic orbitals decay differently into vacuum the spin-polarization of the tunnel current varies with distance.

participating electronic states at the atomic scale. Secondly, using vacuum as the tunnel barrier eliminates any interfering electronic structure within the tunnel process. Thirdly, the spin polarization has to be measured on an absolute scale. MTF-STM fulfills all of these requirements as discussed in Sec. 5.3.

When measuring the spin polarization of the tunneling electrons on the Co nanoisland, it is observed that the spin polarization strongly varies with tip-to-sample distances. To investigate the distance dependence of the spin polarization, the tunnel current is increased for the stabilizing conditions from  $I_S = 0.5 \text{ nA}$  to  $I_S = 100 \text{ nA}$  at  $V_S = 9.5 \text{ mV}$ . After stabilizing the tunnel contact,  $dI/dV$  spectra are acquired on a fixed position in the center of a Co island and on the bare Cu surface for decreasing tip-to-sample distances. Two representative  $dI/dV$  spectra are presented in Fig. 5.12 which correspond to the largest and the smallest found spin polarizations. The extracted spin polarization is shown in Fig. 5.13. On Co, the analysis yields an increase of the spin polarization from  $34 \pm 3 \%$  to  $56 \pm 5 \%$  when the tip-to-sample distance is increased by only  $2.3 \text{ \AA}$ . This corresponds to an increase in spin polarization of  $65 \%$ . At the same time the conductance decreases from  $0.14G_0$  to  $0.0007G_0$  where  $G_0 = 2e^2/h$  is the conductance quantum. For this measurement range, the spin-filtering is highly sensitive on the barrier width ( $dP/dz \approx 10 \%/ \text{\AA}$ ), which clearly outperforms the benchmark material MgO in its standard range of application [137].

The strong distance dependence of the spin polarization can be attributed to the specific

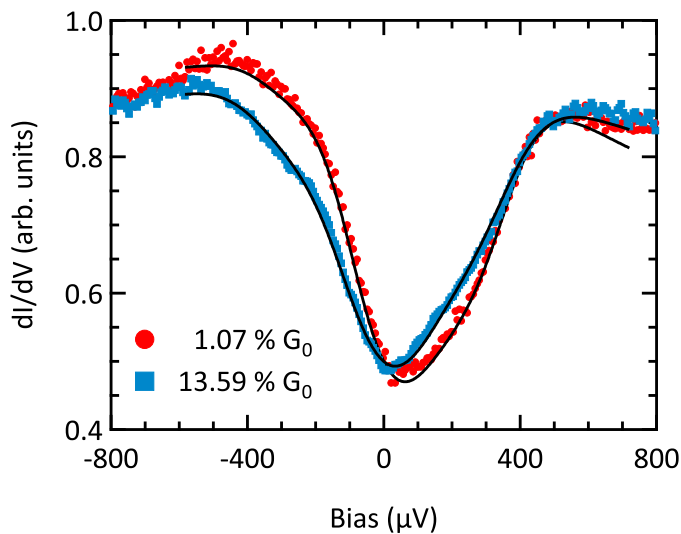


Figure 5.12: Differential conductance measured at two different tip-to-sample distances on a Co island. At higher conductance the  $dI/dV$  spectrum is less asymmetric due to a lower spin polarization ( $P = 34 \pm 3\%$ ) than at lower conductance ( $P = 56 \pm 5\%$ ).

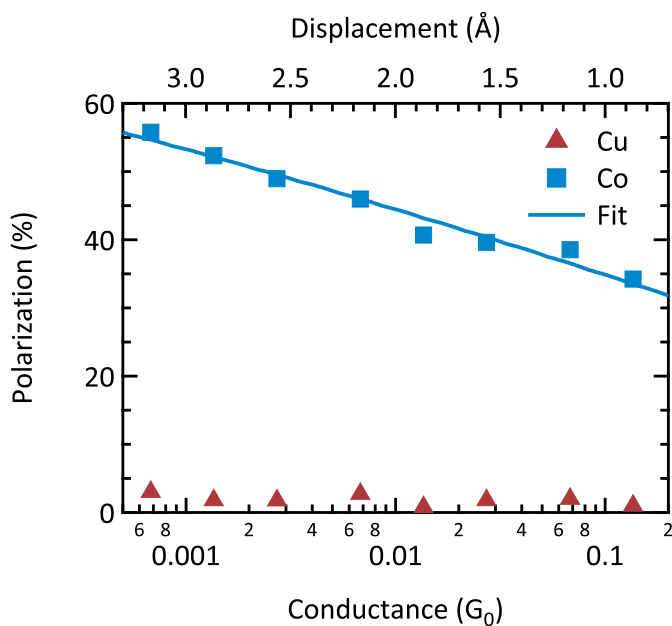


Figure 5.13: Distance dependence of the spin polarization of tunneling electrons. The spin polarization is measured on a single position of the Co island and the Cu surface for increasing conductance values. The fit shows the spin polarization calculated from a simple 1D model presented in Fig. 5.14.

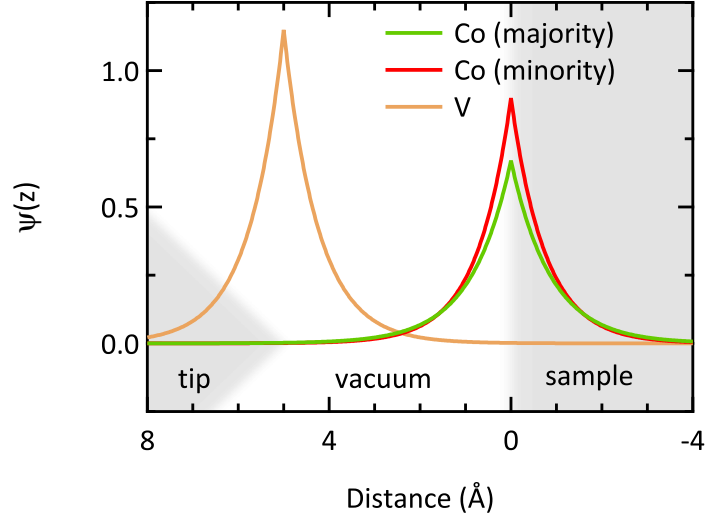


Figure 5.14: 1D model for the distance dependence of the spin polarization. In this model, the overlap as a function of distance is calculated for the Co minority and majority states with the exponentially decaying state of the tip.

electronic structure of the Co island, as the tip is spin neutral in the sense that the decay of the wave function is independent of the spin. In this context, the significant advantage of MTF-STM becomes obvious because changes of the spin polarization can be directly related to the spin polarization of the sample due to the known electronic structure of the tip. For a more quantitative analysis, a simple 1D model is utilized to describe the electronic states contributing to the tunnel current  $I$ . In this model, the spin polarization is defined as

$$P = (I_{\uparrow} - I_{\downarrow}) / (I_{\uparrow} + I_{\downarrow}), \quad (5.1)$$

with the spin-up ( $\uparrow$ ) and spin-down ( $\downarrow$ ) contributions of the tunnel current:

$$I_{\uparrow\downarrow} \propto |\langle \psi_{\uparrow\downarrow} | \psi_{\text{tip}} \rangle|^2. \quad (5.2)$$

Thus, the spin polarization only depends on the overlap of the majority (minority) Co wave function  $\psi_{\uparrow}$  ( $\psi_{\downarrow}$ ) with  $\psi_{\text{tip}}$ , the wave function of the tip. The decay of the wave functions into vacuum is modeled by exponential functions in the form of  $\psi(z) = \alpha e^{-\beta|z|}$  (Fig. 5.14). For the Co majority surface state, the vacuum wave vector  $k_0 = \sqrt{2m_0\Phi/\hbar^2}$  is used with the free electron mass  $m_0$  and the work function  $\Phi = 5 \text{ eV}$  for Co [138, 139]. The minority state is also approximated by an exponential decay and the decay constant is chosen in such a way as to reproduce the spin polarizations known from DFT calculations [126, 127].  $P = -3\%$  ( $P = 34\%$ ) is modeled at  $2.08 \text{ \AA}$  ( $4.16 \text{ \AA}$ ) above the Co island similar to the results provided by DFT calculations for the system [140]. The solid line in Fig. 5.13 represents a fit of this model to the measured distance dependence of the spin polarization of the tunneling electrons. When increasing the tip-to-sample distance the overlap with the localized minority state

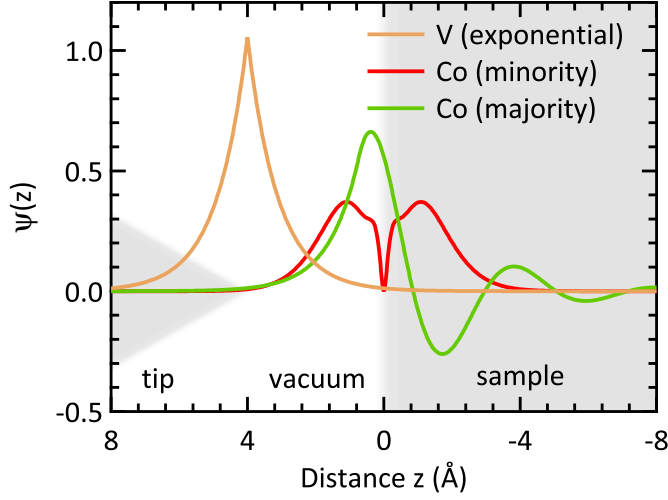


Figure 5.15: Alternative 1D model for distance dependence of the spin polarization. The electronic state of the V tips is modeled as in Fig. 5.14. The majority Co state is described by a Shockley type surface state and the Co minority state consists of Slater type Co(4s) states (75 %) and Co(3d) states (25 %).

decreases more quickly than the overlap with the delocalized majority state, hence, the spin polarization of the tunneling electrons increases in very good agreement with the experimental observations. Competing effects, such as the change of the tunnel barrier height or trapping states [141–144], are negligible in the measurement setup as discussed below.

In addition, the 1D model can also be used to estimate the tip-to-sample distance. For the best fit result, the factor of proportionality in Eq. 5.2 is determined in such a way that the tip-to-sample distance is 8.6 Å for the lowest conductance value and 6.2 Å at the largest conductance. The difference of 2.4 Å is in good agreement with the  $z$  values of the stabilization conditions for the tunnel contact. The tip-to-sample distances calculated by the 1D model also concur with two simple approximations: The tip-to-sample distance should be in the order of the lattice constant ( $a = 2.08$  Å) at  $G = G_0$  and a tunnel resistance of 10 Å at  $R = 10$  GΩ.

As an alternative for the 1D model presented in Fig. 5.14, the exponential functions for the Co states are replaced by more realistic models. To this end, the majority Co state is modeled by a surface state of a semi-infinite crystal [138]. Contrary to bulk states, the surface state decays not only into vacuum but also into the bulk material. The respective solutions of the wave function in vacuum ( $z \geq z_0$ ) and in the crystal ( $z \leq z_0$ ) are derived from Ref. 138:

$$\psi_{\text{out}}(z) = \alpha e^{-k_0 z} \text{ for } z \geq z_0 \quad (5.3)$$

$$\psi_{\text{in}}(z) = \beta e^{\mu z} \cos(\pi z / a + \delta) \text{ for } z \leq z_0 \quad (5.4)$$

with the wave vector  $\mu$ , the phase shift  $\delta$ , the lattice constant  $a$  and the normalization factors  $\alpha$  and  $\beta$ . The vacuum wave vector  $k_0 = \sqrt{2m_0\Phi/\hbar^2}$  is used with the free electron mass  $m_0$

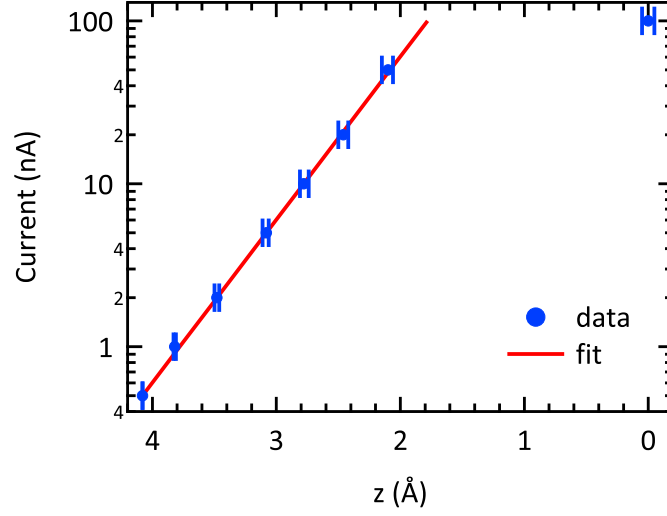


Figure 5.16: Distance dependence of the tunnel current. The tunnel current increases exponentially when the tip-to-sample distance is decreased demonstrating that the measurements apart from the last point are taken in the tunneling regime.

and the work function for Co [138, 139]. The remaining parameters are obtained by the norm  $|\psi(z)|^2 = 1$ , the continuity of the wave function ( $\psi_{\text{out}}(z_0) = \psi_{\text{in}}(z_0)$ ) and its derivative ( $\psi'_{\text{out}}(z_0) = \psi'_{\text{in}}(z_0)$ ). The minority state is modeled by Slater type radial orbital wave functions [145, 146]:

$$\psi_n(z) = N(z/a_0)^{n_{\text{eff}}-1} e^{-\frac{Z_{\text{eff}}}{n_{\text{eff}}} z/a_0} \quad (5.5)$$

where  $N$  is a normalization factor,  $a_0$  represents the Bohr radius,  $n_{\text{eff}}$  is an effective quantum number and  $Z_{\text{eff}}$  is an effective nuclear charge. The modeled minority state mostly consists of Co(4s) states (75 %) and Co(3d) states (25 %), which is in accordance with DFT calculations of this system [140]. As it turns out, this model can be used to fit the experimentally measured distance dependence of the spin polarization (Fig. 5.13). However, it leads to less realistic tip-to-sample distances and the reported spin polarization above the Co island are not reproduced. When the parameters are chosen in order to obtain  $P = -3\%$  ( $P = 34\%$ ) at  $2.08 \text{ \AA}$  ( $4.16 \text{ \AA}$ ) above the Co island, the measured distance dependence cannot be fitted anymore. Due to the complicated electronic structure of the Co island, it is unclear if Eq. 5.3 to Eq. 5.5 actually represent a more applicable description. Therefore, the simpler exponential decay is employed for the analysis.

When measuring the distance dependence of the spin polarization, the tip-to-sample distance is reduced due to the increasing tunnel currents in the stabilizing conditions. It is important to note that the measurements are still carried out in the tunneling regime and effects due to the transition to the point contact regime can be neglected. In Fig. 5.16, the tunnel current

is shown as a function of the distance  $z$ , which are drift corrected at the stabilizing bias ( $V_S = 9.5$  mV). For all except the last data point in the investigated conductance range, the tunnel current follows an exponential law with the decay constant  $\alpha = 2.3 \text{ \AA}^{-1}$ . As expected for the tunneling regime, the current decreases by an order of magnitude when the tunneling distance is increased by  $1 \text{ \AA}$ . Since the tunnel current follows this exponential law, only the width of the tunnel barrier needs to be considered in the theoretical 1D description. Changes in the barrier height  $\Phi$  are negligible. This is an important finding, since it means that the electron wave vector in the barrier  $\kappa$  is constant ( $\kappa \propto \sqrt{\Phi}$ ). Therefore, the distance dependence of the spin polarization is not the result of the varying electron momentum as described by the Slonczewski model [141, 142].

This study demonstrates the direct correlation between the characteristic decay of electronic states and the spin polarization of tunneling electrons. Varying the tunneling distance through a well-defined vacuum barrier leads to the tunable spin-filtering effect. No particular electronic properties of the tunnel barrier are required. Thus, the effect is universal and plays an ubiquitous role in any tunnel junction with at least one ferromagnetic electrode. The experiment provides direct access to the underlying physical mechanism involved in the spin-dependent tunneling process and, therefore, is ideal for comparison with theoretical models. MTF-STM represents an excellent technique to disentangle the contributions of the electrode and barrier material to the spin-polarized tunnel currents. Besides fundamental aspects, the approach offers direct access to a wide variety of systems mimicking components of real devices. For example, the role of metal oxide barriers in spin filters can be investigated on the atomic scale allowing additional information on structural influences, participating electronic wave functions or the formation of localized states [144]. In novel spintronic devices on the molecular or even on the atomic scale [118–121, 147] the approach provides direct insight into the detailed spin properties.

### 5.5 Alternatives for Probing Spin Polarization at the Nanoscale

MTF-STM combines the virtues of STM with the absolute probing capability for the spin polarization. The superconducting quasi-particle DOS of the tip is spin-neutral in the sense that the orbital wave function is the same for spin-up and spin-down electrons. Furthermore, there is no magnetic moment interfering with the magnetization of the sample which makes it the ideal probe for magnetic nanostructures. However, one also has to consider its limitations. From a technical perspective, the energy resolution ( $\mu B > k_B T$ ) requires operation at millikelvin temperatures, which is experimentally challenging, especially for STM (Sec. 3.2). An additional limitation represents the required magnetic field, which effects the magnetization of the sample. While MTF-STM might also work with magnetic fields applied perpendicular to the tip axis (parallel to the sample surface), this has not yet been demonstrated. Furthermore, the spin polarization is only revealed for the Fermi level and other energies cannot easily be accessed. In this section, the novel MTF-STM is compared to existing techniques probing the spin polarization of electrons (Tab. 5.1). Without any claim to completeness, this brief

## 5.5. Alternatives for Probing Spin Polarization at the Nanoscale

	MTF-STM	SP-STM	Shot Noise	Point Contact	Optical	Kondo Effect
$P$	absolute	relative	lower limit	absolute	absolute	absolute
$E$	$E_F$	$eV$	$E_F$	$E_F$	$eV - E_g \leftrightarrow E_F$	$E_F$
$B$	required	possible	possible	possible	possible	required
$T$	$\mu B > k_B T$		$\approx 4.2$ K	$T_c$	RT	$\mu B > k_B T_K$
$\mu$	no	yes	no	no	no	yes

Table 5.1: Probing spin polarization at the nanoscale. The overview compares several techniques for measuring the spin polarization  $P$  with differences in the electron energy  $E$  and the required external magnetic fields  $B$ , and the temperature regimes  $T$  for their application. The presence of magnetic moments in the spin detecting probes is indicated by  $\mu$ . So far, the experimental realization with atomic scale control has not been demonstrated for the last three methods.

summary focuses on techniques that are principally able to provide spatial resolution at the nanoscale. In this context, the measurement of the spin polarization is discussed for SP-STM [122] and for shot noise measurements carried out by STM [148]. The use of superconducting point contacts [149] is experimentally connected to MTF-STM. Additional techniques employ optical spin detectors [150] or Kondo systems for the spin detection [151].

SP-STM is a well established technique to investigate magnetic systems at the nanoscale. It relies on the tunnel magnetoresistance (Sec. 2.2.3) between sample and tip, which is either magnetic or coated with magnetic material. In this simple model, the asymmetry of the differential conductance reads as:

$$A = \frac{dI/dV_{AP} - dI/dV_P}{dI/dV_{AP} + dI/dV_P}, \quad (5.6)$$

with parallel (P) and anti-parallel (AP) magnetization directions of tip and sample. The asymmetry is directly linked to the spin polarization of the tip  $P_T$  and the spin polarization of the sample  $P_S$  by [122, 127]

$$A = -P_T P_S. \quad (5.7)$$

In principle, the signal can be obtained from two  $dI/dV$  maps recorded for both magnetization directions. However, the analysis is not straightforward due to the spin-dependent stabilization conditions of the tunnel contact and the complex data analysis. Alternatively, the tip's magnetization is modulated at high frequencies, so that it flips too fast to be compensated for by the feedback loop of the STM. The recorded signal becomes proportional to the local magnetization [152]. A major drawback of SP-STM is the fact that the recorded signal contains not only the spin polarization of the sample but also the spin polarization of the tip. The latter is generally unknown, at least for the less demanding tip preparations such as tip dips into magnetic films or bias pulses to collect magnetic atoms. On the plus side, the magnetic fields are only required to switch the relative magnetization between tip and sample. When modulated, the amplitude of the magnetic field is usually much smaller than the fields required for

MTF-STM. Anti-ferromagnetic tips are used to minimize the effect of stray fields. Nevertheless, any conclusions on absolute values of the spin polarization are difficult due to the influence of the tip-to-sample distance and the different decay of electron orbitals (Sec. 5.4). An advantage of SP-STM is the more flexible energy and temperature range in comparison to MTF-STM.

Another approach to probe spin-polarized transport is to analyze the shot noise of electric currents [148]. Shot noise arises from the quantization of the electron charge and can be measured by STM. For electrons with identical spins, the noise reduces by antibunching of the fermions according to the Pauli principle [153]. In general, the transport occurs via multiple conduction channels adding up to the total conductance  $G = G_0 \sum_i \tau_i$  with the transmission probability  $\tau_i$ . Including the spin reduces the spectral noise by the Fano factor  $F$  [148]:

$$F = \frac{\sum_j \tau_j (1 - \tau_j)}{\sum_j \tau_j}, \quad (5.8)$$

with  $j = (i, \sigma)$  describing the spin orientation. While the Fano factor provides a measure for the spin polarization at the Fermi energy, it also depends on the transmission probability of the transport channels  $\tau_i$ , which is usually unknown. Therefore, the approach only provides a lower limit for the measured spin polarization in the case of multi-channel transport. Furthermore, the spin quantization axis only needs to be fixed for time scales at which the tunneling processes occur. For the experimental realization, shot noise detection sets high demands on the measurement and amplification of small electric currents. Probing at low temperatures ( $\approx 4.2$  K) and at high frequencies is favorable in order to separate shot noise from other contributions, such as temperature dependent noise or  $1/f$  noise. The measurement can be combined with external magnetic fields.

Superconducting point contacts have been used to determine the spin polarization of metals [149]. In the ballistic transport regime, Andreev reflections convert the normal currents to supercurrents at the metallic interface opening an additional conductance channel for energies within the superconducting gap. The efficiency of the additional conductance channel is a measure for the spin polarization at the Fermi energy [149]:

$$P = \frac{N_{\uparrow}(E_F) v_{F\uparrow} - N_{\downarrow}(E_F) v_{F\downarrow}}{N_{\uparrow}(E_F) v_{F\uparrow} + N_{\downarrow}(E_F) v_{F\downarrow}}, \quad (5.9)$$

with the Fermi velocities  $v_{F\uparrow\downarrow}$ . This definition of the spin polarization is not necessarily the same as in Eq. 3.20. In comparison to the MTF technique, the approach based on the Andreev reflections has revealed different results of spin polarization that have been attributed to the unequal definitions, scattering effects at the metallic interfaces or simply variations of the spin polarizations for the investigated metals [149]. In principle, the superconducting V tips (Sec. 4.2) could also function as point contacts. Indeed, such an experiment has been attempted once in the mK-STM to compare the spin polarization obtained from tunneling and ballistic transport. However, it was not possible to achieve a stable point contact on the Co nanoisland. Nevertheless, the use of superconducting STM tips as local probes in the



## 5.5. Alternatives for Probing Spin Polarization at the Nanoscale

---

point contact regime represents an additional experimental challenge and sets high demands on the mechanical stability of the system. So far, locally resolved measurements of the spin polarization have not been demonstrated by the approach based on the Andreev reflections. However, it would be less demanding in terms of the energy resolution since the temperature regime is only governed by the critical temperature of the superconductor  $T_c$ . In addition, the technique would not require external magnetic fields, which, however, could still be used as an additional degree of freedom.

The spin polarization of tunneling electrons has also been measured with optical spin detectors [135, 150]. In an STM, a ferromagnetic Ni tip has been used on an AlGaAs(110) surface. The semiconducting sample not only forms the tunnel barrier but also serves as an optical spin detector [135, 150]. The degree of circular polarization in the light emitted by the recombination process in the semiconductor reveals absolute values of the spin polarization of the tunneling electrons. The optical detection is also spin-neutral, which means there are no magnetic stray fields interfering with the sample nor spin-polarized orbitals altering the tunneling probability for spin-up and spin-down electrons. In addition, there is no influence of topographic features on the measured spin polarization and external magnetic fields can be applied, though they are not required. Measurements have been carried out at room temperature [135, 150]. The probed binding energy range  $eV - E_g \leq E < E_F$  of the sample depends on the semiconducting gap  $E_g$  and the applied voltage  $V$ . The main challenge of the optical approach is spatial resolution in measurements, which would require the reversed experimental arrangement with the STM tip as optical detector. This would imply the challenging fabrication of STM tips made from crystalline AlGaAs with unaltered band structure, which has not been achieved so far.

As an alternative to the superconducting DOS employed in MTF-STM, Kondo systems have been proposed for quantitative measurements of the spin polarization [151]. In general, the Kondo effect describes an additional resonance in the LDOS at the Fermi level due to the screening of local magnetic moments by the surrounding host electrons. When the Zeeman energy in external magnetic fields exceeds the Kondo energy ( $\mu B > k_B T_K$ ), the characteristic Kondo signal is split into two independent fully spin-polarized peaks [151]. Such a system can be employed to measure the spin polarization of tunneling electrons on an absolute scale. It would require attachment of a Kondo system to the apex of an STM tip with a suitable Kondo temperature for available magnetic fields. However, this would still create obstacles similar to SP-STM such as interference of the magnetic tip moment with the magnetization of the sample and spin-dependent decay of the electron orbitals.



# 6 Probing Local Magnetic Moments Interacting with a Superconductor

In this chapter, the local excitations of the superconducting quasi-particle DOS induced by isolated magnetic moments are probed by STM. To this end, differential conductance spectra are obtained for magnetic molecules on the superconducting V(100) surface. Due to the magnetic coupling and the Coulomb potentials, bound states are formed within the superconducting gap at several energies. Their spectral properties appear strongly non-isotropic in spatially resolved measurements, which is attributed to the electronic structure of the adsorption sites and the reconstruction of the V(100) surface. Moreover, the quasi-particle excitations do not only occur on the molecule but also in its close vicinity, where their intensities decay within the distance  $x \approx \pm 30 \text{ \AA}$  while simultaneously showing periodic oscillations. These observations are explained by a 1D model assuming two magnetic moments within the molecular structure. The work presented in this chapter is still an ongoing project and, therefore, the analysis as well as the conclusions are preliminary.

## 6.1 Overview and Motivation

Conventional superconductivity arises from electrons forming Cooper pairs with opposing spin moments according to BCS theory (Sec. 2.1.2). The superconducting pairing is not only effected by external magnetic fields (Sec. 2.1.4) but also by the introduction of local magnetic impurities (Sec. 2.3). In their presence, the coherence of the superconducting state is locally weakened, which is manifested in the creation of bound states [72–74]. Inside the energy gap of the quasi-particle DOS, they occur as additional resonances revealing detailed information about the superconducting state [11–14]. For example, additional features within the superconducting gap have been observed on macroscopic planar tunnel junctions containing magnetic impurities [154]. On the atomic scale, STM has resolved the local distribution of bound states induced by single magnetic atoms on superconducting surfaces [16–18]. In this context, one of the most important findings represents quasi-particle excitations, which are not only limited to the impurity site but also detectable within a few Fermi wavelengths in its vicinity (Sec. 2.3.2) [16]. Increasing the impurity concentration in a controlled way might lead to interesting phenomena, such as the formation of impurity bands and gapless super-

conductivity [73, 155]. To this end, it is essential to fully understand the spatial distribution of the quasi-particle excitations, especially the short decay of the bound states in the vicinity of impurities.

### 6.2 Copper Phthalocyanine on V(100)

On metallic surfaces, the electronic configuration of single adsorbed atoms is usually effected by the itinerant electrons of the substrate. In order to protect their electronic properties, such as their magnetic moment, the atoms are decoupled from the substrate by using thin insulation layers [156, 157] or by encapsulating them in chemically stable molecules [18]. For the latter, metal-phthalocyanines are highly suitable due to their neutral end groups forming the mechanical contact and shielding the inner part. Metal-phthalocyanines have been deposited on various substrates as isolated molecules, self-organized molecular networks, and as mono- and multilayers [18, 158].

Here, copper phthalocyanine (CuPc) is employed to decouple the Cu core from the superconducting V(100) substrate [142, 161, 162]. CuPc represents a stable molecular structure, where the Cu bonds to four ligands consisting of pyrrole and benzene. In the gas phase, the bonding leaves the Cu ion in the oxidation state  $\text{Cu}^{2+}$  resulting in a  $S = 1/2$  ground state [163]. Experimental studies have shown that the magnetic moment of CuPc even continues to exist when the molecule is adsorbed on metal surfaces [164]. The size of an isolated CuPc molecule is about  $1.4 \text{ nm} \times 1.4 \text{ nm}$ . A low coverage of CuPc molecules is deposited at  $T_{\text{sample}} = 21 \text{ }^\circ\text{C}$  onto the surface of a V(100) sample, which is thoroughly cleaned beforehand by several cycles of Ar ion sputtering and annealing to  $1000 \text{ }^\circ\text{C}$ . The sample is transferred to the mK-STM (Sec. 3.2) without breaking the vacuum and cooled down to 15 mK. For the measurements presented in the following sections, the same V STM tips used in Chap. 4 and Chap. 5 are utilized to enhance the spectral sensitivity. In Fig. 6.1(a), an STM image of the V(100) surface shows various steps along the crystal axis and rather small terraces that is attributed to the low annealing temperature of the V(100) sample. More importantly, the dark lines observed in the STM images are expected to arise from oxygen absorption sites and point to a  $5 \times 1$  reconstruction of the V(100) surface due to the influence of oxygen atoms (Fig. 6.1(b) and (c)) [159, 160]. Their different bond lengths to the V atoms induce mechanical stress, which is compensated by the surface reconstruction of the three top layers. DFT calculations reveal that the O bonds increase the distance between the first and second V layer, whereas the spacing between the second and third layers is decreased [159]. In Fig. 6.1(d), the STM image of the CuPc shows fourfold clover-shaped symmetry reflecting the four Pc rings around the Cu ion. However, there is no visible protrusion in the center of the molecules at the position of the Cu ion. This indicates that the Cu ion fits into the cavity of the surrounding Pc macrocycle forming a planar molecule on the V(100) surface. Due to the surface reconstruction, the detailed structure of the molecule depends on the preferred adsorption site.

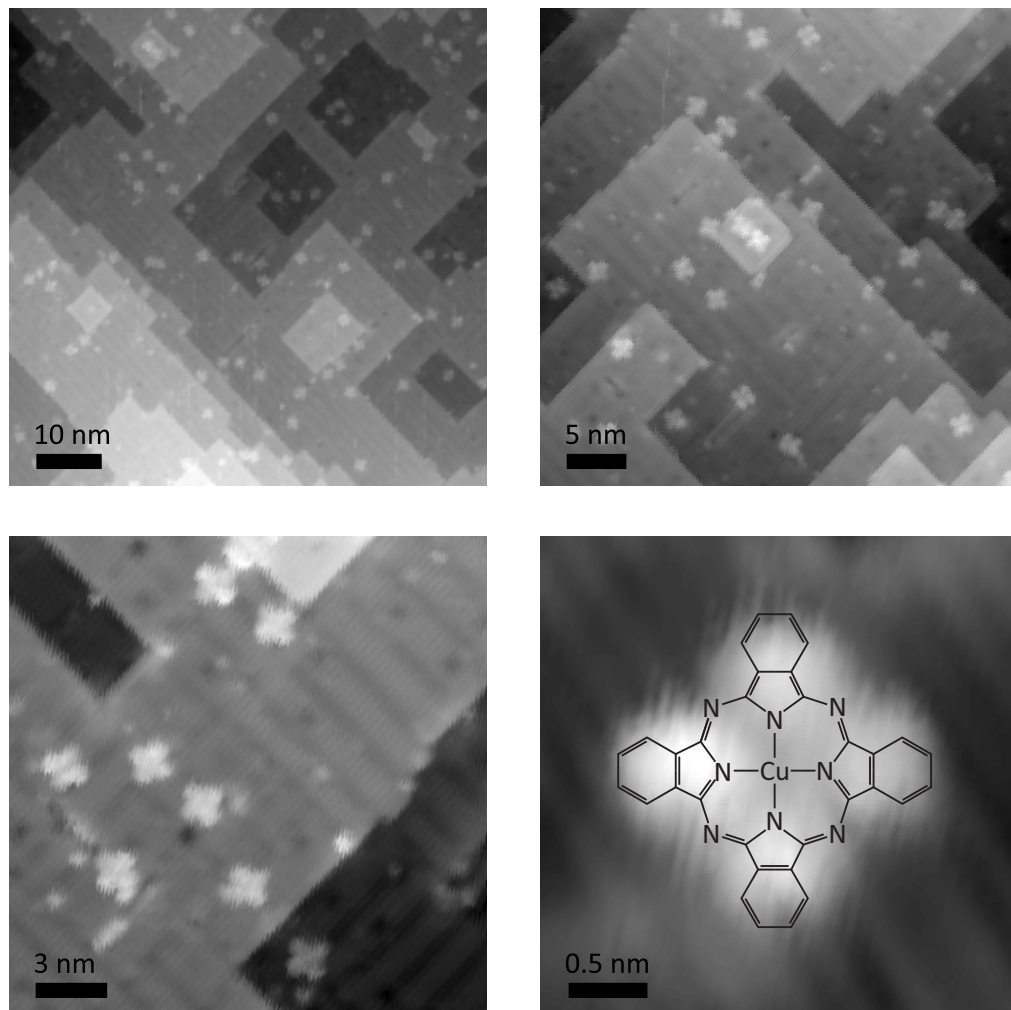


Figure 6.1: CuPc on the  $5 \times 1$  reconstruction of the V(100) surface ( $I_T = -50$  pA and  $V_T = -8.5$  mV). (a)-(c) The V(100) surface shows various steps along the crystal axis and a  $5 \times 1$  reconstruction due to the influence of oxygen atoms indicated by the dark lines [159, 160]. (d) The CuPc molecule consists of the Cu core and four ligands. Due to the specific molecular structure, the electronic coupling is reduced between the Cu ion and the V(100) surface.

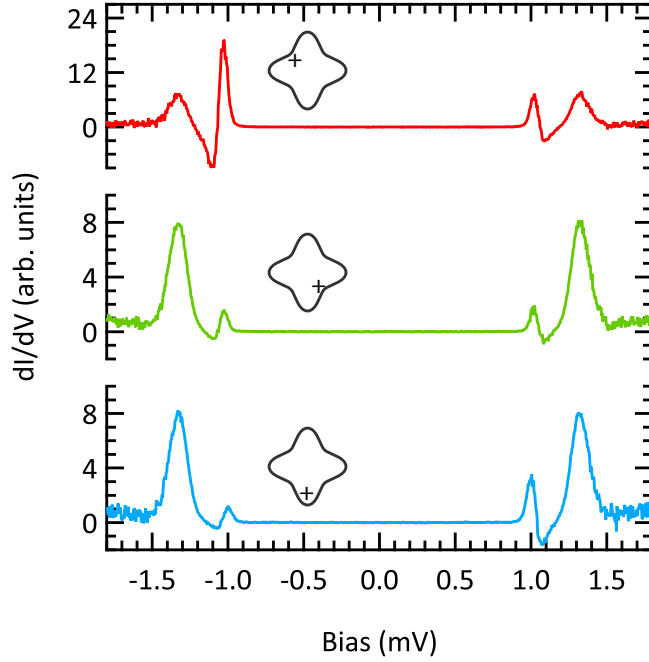


Figure 6.2:  $dI/dV$  spectra measured on three different positions of a CuPc molecule. The increased superconducting gap and the outer peaks result from the electron tunneling between the quasi-particle coherence peaks of tip and sample. Bound states within the superconducting gap are induced by the interaction of conductance electrons and the local potentials of the CuPc.

### 6.3 Observation of Local Bound States

The interaction of the CuPc molecules and the superconducting V(100) surface is probed within the energy range of the superconducting gap. For this purpose, the superconducting DOS of the V STM tip effectively increases the energy resolution and enhances the small in-gap features of the bound states [18]. In Fig. 6.2, the resulting differential conductance spectra show two pronounced peaks at  $\Delta_T + \Delta_S \approx \pm 1.3$  meV, which correspond to electron tunneling between the superconducting coherence peaks of tip ( $\Delta_T$ ) and sample ( $\Delta_S$ ). Since these features require superconductivity in both tip and sample ( $\Delta_T + \Delta_S > \Delta_{0,\text{bulk}}$ ), the measurements demonstrate that the superconducting state of the V(100) sample still exists in the presence of the CuPc molecules. In addition to the outer peaks, the  $dI/dV$  spectra show features inside the superconducting gap of asymmetric height. These bound states result from the locally weakened superconducting state because the electronic structure of the CuPc molecule is not entirely screened by the itinerant electrons of the V surface (Sec. 2.3). Within this study, no Kondo signatures have been observed for CuPc on V(100). In the quasi-particle DOS, the energy position and height of the bound state reflect the influence of the local Coulomb potential and the exchange interaction. In the case of a uniform electronic structure of the metal surface, the asymmetric height of the quasi-particle excitations of electron character

( $V < 0$ ) and hole character ( $V > 0$ ) is attributed to the local Coulomb potential. However, the strong local differences in Fig 6.2 changing from electron to hole-like states within a few angstrom indicate the influence of the substrate with its non-uniform electronic structure. The measurement has been repeated on several CuPc molecules showing a large variety of bound states with various peak numbers, positions and heights. Moreover, CuPc molecules are found that show no in-gap states at all. So far, no direct correlation between the topography and the electronic structure has been observed. The energy positions of the bound states close to the coherence peaks ( $\Delta_T + \Delta_S$ ) reveal the weak coupling of the CuPc and the superconducting conduction electrons. In this regime, the observation of the competing Kondo effect is unlikely because the screening would occur on small energy scales and require large spatial distribution [18].

#### 6.4 Spatial Distribution of Locally Induced Bound States

To obtain a better understanding of the local interaction potentials, a map consisting of 625  $dI/dV$  spectra is measured on the CuPc molecule and its close vicinity. In Fig. 6.3(a), a STM image ( $I_T = -50$  pA and  $V_T = -8.5$  mV) shows the fourfold symmetry of the CuPc molecule on the V(100) surface. The  $z$  values of the spectroscopic map (Fig. 6.3(b)) correspond to the stabilizing conditions ( $I_S = -50$  pA and  $V_S = -2$  mV) before switching off the feedback loop and demonstrates the stable spectroscopy conditions on this particular CuPc molecule. For each data point in Fig. 6.3(b), a differential conductance spectrum is measured for the bias range  $-2$  mV  $\leq V_T \leq 2$  mV. To analyze the differential conductance measurements, the bound states are fitted with Gaussian functions extracting the peak heights and energies. Although this approach provides a good overview of the measured data, it still contains the contribution of the superconducting quasi-particle DOS of tip and sample. Thus, the analysis only provides the relative local variations but no absolute values for the spectral weight and energies of the bound states. The results of the Gauss fits for the quasi-particle excitations with electron character ( $V < 0$ ) are presented in Fig. 6.3(c) and Fig. 6.3(d). Surprisingly, the distribution of the peak heights is not uniform around the Cu ion. Instead, the highest peaks are found on the upper ligand as well as on the right hand site of the CuPc molecule as shown in Fig. 6.3(c). Moreover, the bound states are not limited to the position of the CuPc molecule but also occur in its close surroundings. Outside the molecular structure, the most significant contributions are locally distributed around the part of the CuPc molecule with the highest excitation peaks. These findings indicate that the interaction between the magnetic moment of the Cu ion and the conduction electrons are not limited to the dimensions of the CuPc molecule. The energy positions of the bound states are presented for  $V < 0$  in Fig. 6.3(d). Variations mostly occur within the molecular structure, indicating the non-uniform interaction between the magnetic impurity and the superconducting V(100) surface. The quasi-particle excitations in the lower right corner are shifted to larger energies. This effect might arise from contamination found in this region of the V(100) surface (Fig. 6.3(a) and Fig. 6.3(b)). In addition, the peak height of the bound states is much smaller in this region due to the larger distance from the CuPc

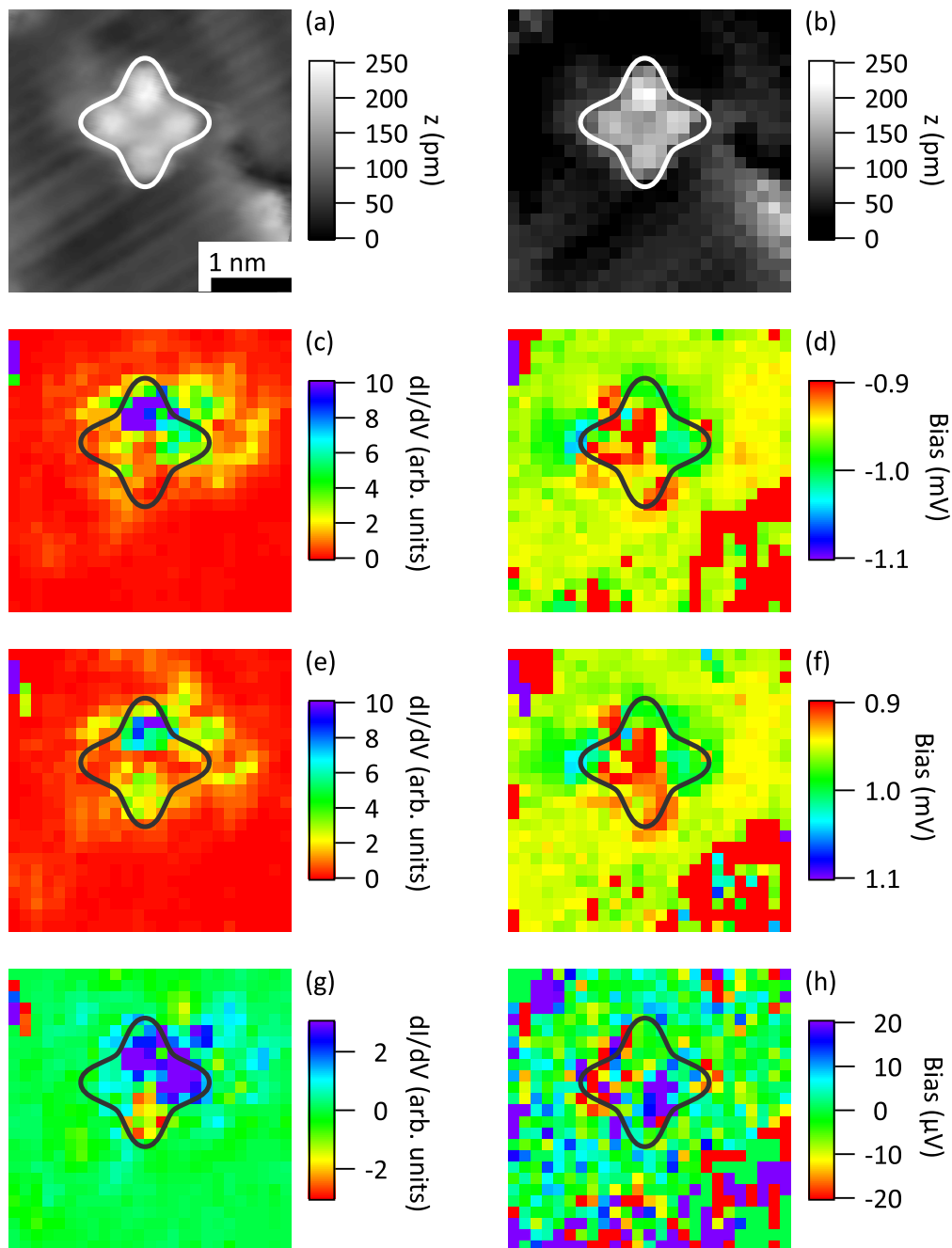


Figure 6.3: Locally resolved bound states observed on an isolated CuPc molecule and its close surroundings. (a) The STM image shows an isolated CuPc molecule on the V(100) surface. (b) The  $z$  stabilization values are presented for a spectroscopic map consisting of 625  $dI/dV$  spectra. (c) - (h) The peak heights and energies of the in-gap states are analyzed by Gaussian fits. (c) Peak heights and (d) energies for negative bias. (e) Peak heights and (f) energies for positive bias. (g) Asymmetry of the peak heights from (c) and (e). (h) The bias difference of the absolute values of (d) and (f).



molecule, which results in larger error estimations of the Gaussian fits. Correspondingly, the analysis based on Gaussian fits is carried out for the bound states with hole character ( $V > 0$ ) as shown in Fig. 6.3(e) and Fig. 6.3(f). Again, the largest peak heights are observed for the upper ligand of the CuPc molecule, however, additional excitations on the lower ligand are more pronounced than in the measurements for  $V < 0$ . As a result, the overall distribution of the hole-like bound states appears more uniform. Their energies with the minimum on the Cu ion resemble the findings for  $V < 0$ , demonstrating the symmetric appearance of the quasi-particle excitations with respect to the Fermi energy. The differences of the bound states for positive and negative bias are summarized in Fig. 6.3(g) and Fig. 6.3(h). Asymmetry peak heights of the in-gap states mostly occur on the CuPc molecule. While the bound states of electron character ( $V < 0$ ) are dominant on the top as well as on the right ligand, the hole-like states determine the electronic structure of the lower ligand (Fig. 6.3(g)). In Fig. 6.3(h), the absolute values for positive bias are subtracted from the positive energy positions after correcting small bias offsets. Within the error estimation for the energy resolution (Sec. 3.2.4), the spectroscopic features occur symmetrically around the Fermi level confirming their origin is due to quasi-particle excitations.

Locally resolving the bound states reveals three important findings. First, the peak heights of the in-gap states are not uniformly distributed on the V(100) surface. This observation might be explained by the different geometries of the fourfold CuPc structure and the  $5 \times 1$  reconstruction of the V(100) surface, which also effects the electronic properties in the normal conducting state. Depending on the adsorption site, the resulting interaction potentials might show strong anisotropies. In addition, a non-uniform Fermi surface produces anisotropic Fermi velocities, which might explain the differences in the formation of the bound states outside the molecular structure [12, 165]. Local variations of the magnetic as well as of the Coulomb potential (for example due to charging effects on the O sites) would further increase the non-uniform distribution of the bound quasi-particle states. The second observation concerning the spatially dependent asymmetry in the peak heights of the bound states also supports the assertion of non-uniform interaction potentials. As discussed in Sec. 2.3, the asymmetry is caused by the Coulomb potential, which breaks the particle-hole symmetry. Variations and sign changes in the asymmetry might occur due to charging effects locally induced within the molecular structure. The third result is that the bound states also occur on the V(100) surface at some distance to the magnetic impurity. With increasing distance from the CuPc molecule, the peak height decreases, indicating a decay on a much shorter scale than the superconducting coherence length. The spatial decay of the bound states is discussed more detailed in Sec. 6.5.

## 6.5 Distance Dependence of Bound States

The spatially resolved differential conductance measurements reveal bound states that are not limited to the dimensions of the CuPc molecules but also appear on their surroundings on the V(100) surface. For a more detailed investigation, more than 60  $dI/dV$  spectra are acquired

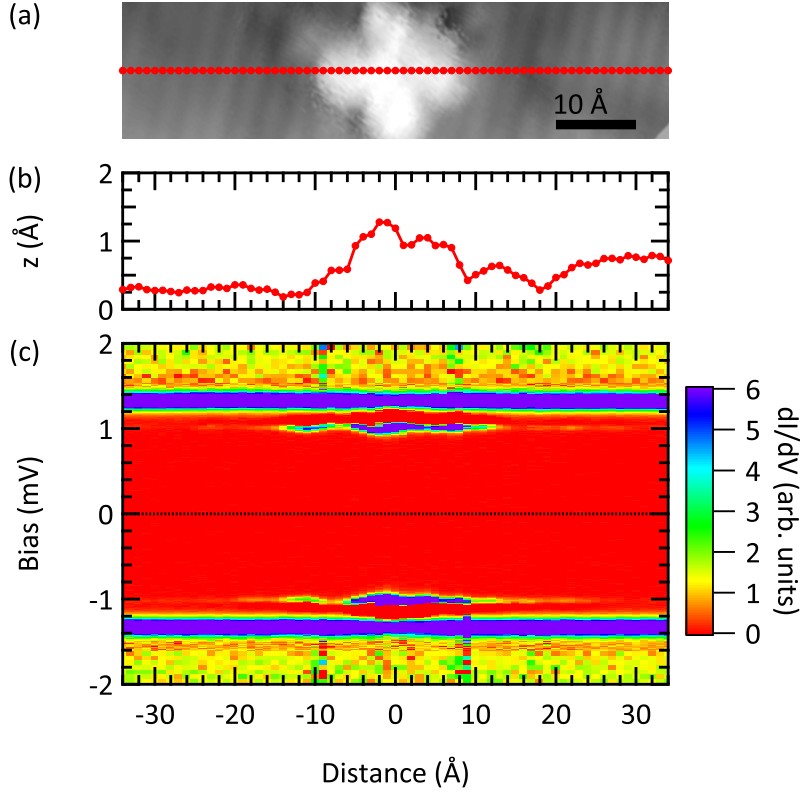


Figure 6.4: Differential conductance measurements for the distance dependence of the quasi-particle excitations. (a) The position for  $dI/dV$  measurements are shown in the STM image by the red markers forming a straight line across the isolated CuPc molecule on the V(100) surface. (b) The  $z$  values correspond to the stabilizing conditions at  $I_S = -150$  pA and  $V_S = -2$  mV. (c) The  $dI/dV$  spectra feature peaks at  $\Delta_1 + \Delta_2 \approx \pm 1.3$  meV due to the tunneling between the coherence peaks of the superconducting quasi-particle DOS of tip and sample. Quasi-particle excitations occur at smaller energies ( $V \approx \pm 1$  meV). Their decay from the center of the CuPc molecule reveals small oscillations in the peak heights.

on a line crossing the CuPc molecule, as shown in Fig. 6.4(a). At each point, the tunnel contact is stabilized at  $I_S = -150$  pA and  $V_S = -2$  mV and the feedback loop is switched off in order to measure the differential conductance with constant tip-to-sample distance. The resulting  $z$  values of the stabilization conditions show the height profile of the CuPc molecule (Fig. 6.4(b)). To optimize the recording time, the density of acquired data points is reduced in the normal conducting regime as well as in the center of the superconducting gap, where no bound states are formed on this particular molecule. The measured  $dI/dV$  spectra (Fig. 6.4(c)) arise from the convolution of the superconducting quasi-particle DOS of the V tip and the LDOS of the sample. At  $\Delta_T + \Delta_S \approx \pm 1.3$  meV, dominant features stem from electron tunneling between the coherence peaks of the quasi-particle DOS of tip and sample. On the CuPc molecule, the gap energies are not significantly effected, indicating that the superconductivity of the V(100) sample is not suppressed by the CuPc molecule. However, the heights of the coherence

peaks are reduced by approximately 30 % on the CuPc structure due to the large amplitude of the bound states and the convolution with the superconducting DOS. Furthermore, induced bound states modify the superconducting quasi-particle DOS of the V(100) surface in the close vicinity of the CuPc structure. The resulting peaks at  $V \approx \pm 1$  meV are clearly visible within the superconducting gap and even surpass the height of the outer coherence peaks. Although the intensities of the quasi-particle excitations decrease with increasing distance  $x$  from the CuPc structure, they are clearly visible within a distance of  $x \approx 30$  Å on both sides of the molecule. On the bare V(100) surface, the peak heights of the in-gap states not only decay but they also show oscillations on a much smaller scale. In addition, variations of their energies are observed in the differential conductance spectra.

For a more quantitative analysis, the intensities and energies of the bound states are extracted from the differential conductance measurements. To this end, the tunnel current is numerically calculated by Eq. 3.9, where the superconducting quasi-particle DOS is included from Eq. 3.22. The bound states are modeled by two Gaussian functions added to the superconducting DOS of the V(100) surface:

$$\rho_{\downarrow\uparrow}(E) = \frac{\rho_0}{2} \operatorname{sgn}(E) \operatorname{Re} \left( \frac{u_{\pm}}{\sqrt{u_{\pm}^2 - 1}} \right) + \sum_{i=1}^2 a_i \exp \left( -\frac{(E - E_i)^2}{2b_i^2} \right), \quad (6.1)$$

where  $u_+$  and  $u_-$  depend on pair breaking and spin-orbit coupling (Sec. 2.1.6).  $a_i$  is the height of the peak resulting from the bound state,  $E_i$  represents the center of its energy position and  $b_i$  gives the standard deviation of the Gauss function. Due to the rather large tip-to-sample separation, contributions resulting from Andreev reflections or Josephson tunneling can be neglected for the analysis. For fitting the experimental data, the differential conductance is numerically calculated from the tunnel current for the investigated bias range. The best results are obtained for small pair breaking in tip ( $\xi_{\text{tip}} = 0.005$ ) and sample ( $\xi_{\text{sample}} = 0.012$ ). The superconducting gap of the tip is kept constant at  $\Delta_{\text{tip}} = 600$  µeV and the resulting gap of the sample  $\Delta_{\text{sample}} = 744 \pm 15$  µeV shows only small variations within the error estimation of the energy resolution. In addition to the pair breaking, small values for the damping parameter  $\Gamma = 18 \pm 6$  µeV provide better fits to the experimental data.

In Fig. 6.5, the extracted energies  $E_i$  of the bound states are shown as a function of distance. While large variations occur in the central region on the CuPc molecule, the energies of the induced bound states appear rather constant on the V(100) surface. The energies are symmetrically distributed around zero-bias due to the quasi-particle nature of the bound states. In general, there are several possible explanations for these observations. First, the CuPc molecule might create multiple local charging sites on the V(100) surface, which alter the Coulomb potential within the molecular structure. Second, the magnetic coupling between the spin moment of the molecule and the conduction electrons of the V(100) surface depends on the overlap of the atomic orbitals, which is given by the characteristics of the adsorption site. In this context, it is also possible that multiple magnetic centers are formed instead of a single

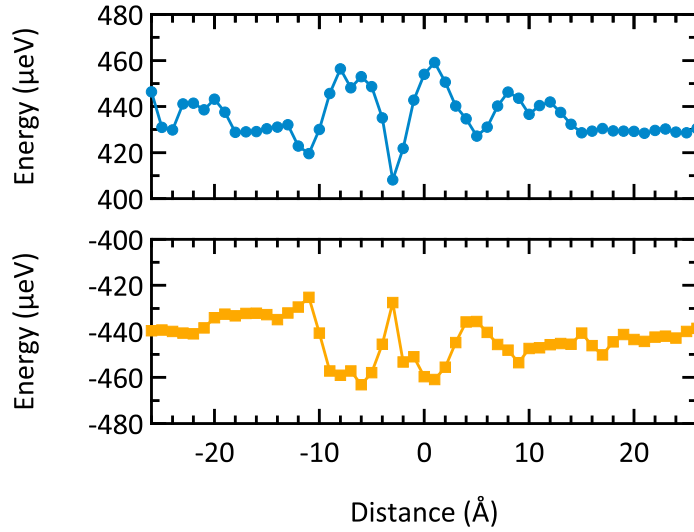


Figure 6.5: Spatially resolved distance dependence of the energies for impurity induced bound states. The energies of the bound states vary on the CuPc molecule indicating the influence of the interaction potentials. In contrast, the quasi-particle excitation energies appear rather constant on the bare V(100) surface.

magnetic moment and, as a result, the magnetic potential becomes strongly correlated with the local position. Third, the energies of the bound states depend on the Fermi surface. Due to the  $5 \times 1$  surface reconstruction of the V(100) and the interaction with the CuPc molecule, the resulting Fermi surface is most likely not uniform, which directly effects the properties of the bound quasi-particle states.

In Fig. 6.6, the intensities of the bound states are extracted from the differential conductance measurements by the fitting function based on Eq. 6.1. On the CuPc molecule, the bound states with the highest intensities are observed. However, the maximum is not directly located in the center of the molecular structure as already observed in the previous experiment (Fig. 6.3). On both sides of the molecule, the intensities of the bound states decay until the signal vanishes in the background noise at the distance  $x \approx \pm 30 \text{ \AA}$ . In addition to the decay, periodic oscillations in the intensities are observed for positive as well as negative bias. As a result, the character of the bound state frequently switches between electron-like and hole-like quasi-particle excitations. In good agreement to Eq. 2.64, the decay occurs on a much shorter length scale than the superconducting coherence length, but it is not symmetrically distributed around the molecule. Whereas the wave lengths of the oscillations are in the order of the Fermi wave length, the bound states do not periodically vanish as predicted by the sine-squared function in Eq. 2.64. Possible explanations for these deviations are the non-isotropic Fermi surface and non-uniform scattering potentials as discussed for Fig. 6.5. In this context, it is also important to mention that Eq. 2.64 describes the bound states induced by a point impurity. For the CuPc on the V(100) surface, the extent of the magnetic moment might not be negligible in comparison with the Fermi wave length or even the coherence length.

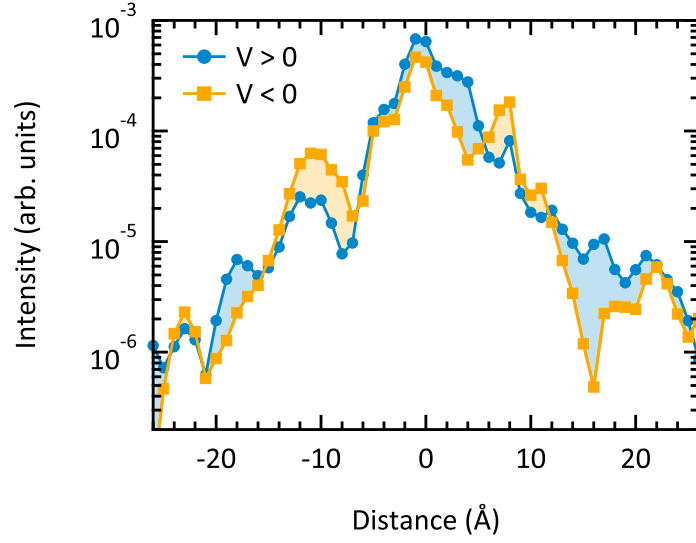


Figure 6.6: Spatially resolved distance dependence of the intensities for impurity induced bound states. With increasing distance, the intensities of the bound states decay on both sides of the CuPc molecule. In addition, periodic oscillations occur for positive as well as negative bias indicating repeated transitions between electron and hole character of the quasi-particle excitations.

For a more quantitative analysis, a simple 1D model for the impurity induced bound states is derived from Eq. 2.64. Instead of a single magnetic moment, the model assumes that the bound states are induced by two separate magnetic impurities at the positions  $x_1$  and  $x_2$ . Then, the measured differential conductance represents the superposition of quasi-particle excitations induced at these two different sites. In addition, the influence of the non-uniform Fermi surface and Fermi wave length on the quasi-particle excitations is taken into account by adding a phenomenological parameter  $\gamma$  to the phase shift in Eq. 2.64. The resulting intensity of the electron-like ( $Z^{(-)}$ ), respectively hole-like ( $Z^{(+)}$ ), quasi-particle excitations reads as a function of distance  $x$  as follows:

$$Z^{(\pm)}(x) = \sum_{j=1}^2 a_j \left( \frac{\sin(k_j x_j - \delta_j^{(\pm)} - i\gamma)}{k_j x_j - \delta_j^{(\pm)} - i\gamma} \right)^2 \exp(-2x_j/\xi_0), \quad (6.2)$$

with the amplitude  $a_j$ , the wave vector  $k_j$ , the phase shift  $\delta_j$ , the coherence length  $\xi$  of  $V$ , and the position of the magnetic point impurities  $x_i$ . The expression is employed as a global fit function to simultaneously analyze the intensities of the bound states for positive (Fig. 6.7) and negative bias (Fig. 6.8). From the fits, the spatial positions of the magnetic impurities are revealed at  $x_1 = 0.01 \text{ \AA}$  and  $x_2 = 1.42 \text{ \AA}$  as well as the corresponding wave vectors  $k_1 = 0.47 \text{ \AA}^{-1}$  and  $k_2 = 0.44 \text{ \AA}^{-1}$ . When combined, their separate contributions (dashed red and green lines) show the overall decay and periodic oscillations of the bound state intensities. However, this approach does not reproduce all of the spectral features in full detail.

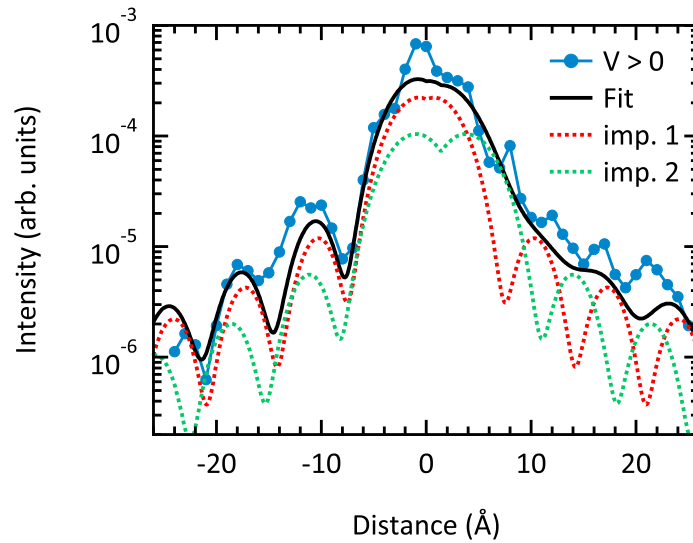


Figure 6.7: Distance dependence of quasi-particle excitations modeled by two magnetic impurities ( $V > 0$ ). The experimentally observed bound states are fitted by a model based on two independent magnetic impurities. They induce quasi-particle excitations (dashed red and green line) and their interference reproduces the measured distance dependence.

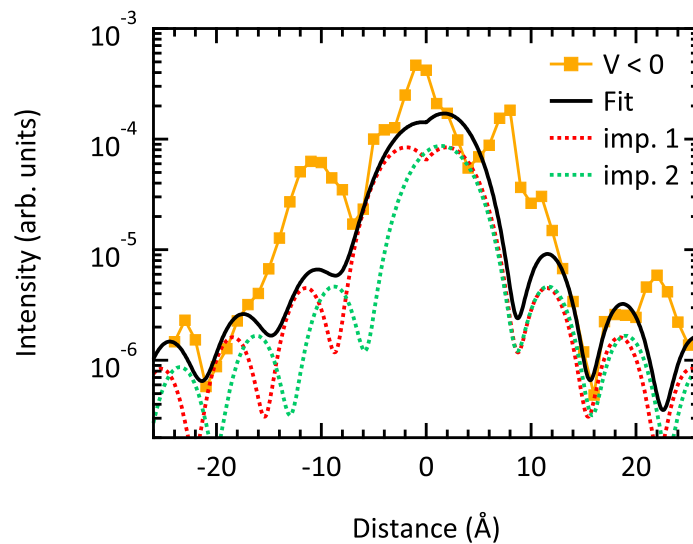


Figure 6.8: Distance dependence of quasi-particle excitations modeled by two magnetic impurities ( $V < 0$ ). The same approach as in Fig. 6.7 is applied for the bound states observed at negative bias.

Studying the interaction of isolated CuPc molecules and the superconducting V(100) surface reveals induced bound states, which are formed within the superconducting gap. Both the energy positions of the bound states close to the coherence peaks and the absence of Kondo signatures in the measured  $dI/dV$  spectra indicate weak coupling between the CuPc molecule and the superconducting conductance electrons of the V(100) sample. The peak heights of the bound states show a non-uniform distribution on the CuPc molecule and in its close vicinity. The findings can be attributed to the non-uniform Fermi surface of the V(100) surface as well as to anisotropic potentials for the magnetic exchange and Coulomb interaction. In both cases, the observed distribution can also be effected by the  $5 \times 1$  reconstruction of the V(100) surface. The quasi-particle excitations are not limited to the dimensions of the CuPc molecules but also appear in close vicinity on the V(100) surface, where the decay of their intensities is compared to a 1D model. Here, assuming two individual magnetic moments considerably improves the agreement between theory and the experimental findings. While the two point impurities used in the model only represent a simplified approximation, the result indicates that the magnetic moment of the CuPc on the V(100) surface is spatially extended over several angstroms. This means that the interaction with the CuPc considerably deviates from the simple description as a point scatterer. The agreement between the experimental data and the 1D model is further improved by the phenomenological parameter  $\gamma$ , which is attributed to the influence of the the non-uniform Fermi surface and the  $5 \times 1$  surface reconstruction of the V(100) crystal. Whereas the discussed approach only represents a simplified description of the complex system, it captures the experimental observations and explains the underlying mechanism for the impurity induced bound states.





## 7 Summary and Outlook

The thesis aims for a better understanding of the complex interplay between superconductivity and magnetism. Here, the effects of geometrical confinement, magnetic fields and isolated magnetic moments have been investigated by STM at millikelvin temperatures as well as by numerical calculations based on a 1D Usadel equation. The characterization of geometrically confined superconductors in magnetic fields has enabled the development of a novel approach to quantitatively probe the spin polarization of conduction electrons with atomic scale resolution.

### 7.1 Geometrically Confined Superconductors in Magnetic Fields

The combined effects of magnetic fields and geometrical confinement have been investigated for superconducting STM tips made from V wire. The experimentally obtained magnetic field dependence considerably differs from bulk material and the analysis based on the extended Maki model requires the additional broadening parameter  $\Gamma$ . A more quantitative description has been derived from a quasi-classical approach based on a 1D Usadel equation. To this end, the non-uniform superconducting state has been calculated for the cone geometry, which was used as a model for the V STM tips. The calculations lead to a direct correlation between the opening angle  $\alpha$  of the conical superconductor and the order of the superconducting phase transition in magnetic fields. For very sharp tips with opening angles below a critical value ( $\alpha < \alpha_c$ ), first order phase transitions occur, whereas second order phase transitions are present in blunter tips ( $\alpha > \alpha_c$ ). Furthermore, the numerically calculated magnetic field dependence has been analyzed by the extended Maki model for several opening angles with the aim of comparing the microscopic Usadel description to the experimental findings. As a result, the order of the phase transition is determined for the STM measurements and first as well as second order phase transitions are found, depending on the investigated V tip. In addition, the calculated correlation of the damping parameter and the opening angle of the superconducting geometry explains the experimentally observed broadening in the  $dI/dV$  spectra. From a fundamental point of view, this approach provides a possible microscopic explanation of the broadening parameter  $\Gamma$ , which has been used on a phenomenological

basis within the extended Maki model. In this context, the  $\Gamma$  parameter represents a formal extension to use the Maki model for non-uniform superconductors exposed to high magnetic fields.

The better understanding of the superconducting STM tips enables novel experimental concepts, such as MTF-STM [97]. In addition to probing absolute spin polarization, superconducting STM tips also play an important role for enhancing the effective energy resolution, where the limiting thermal broadening of the Fermi edge is overcome by the superconducting gap in the quasi-particle DOS [18, 99]. As a result, experimental investigations can resolve small spectral features, which lie beyond the thermal resolution limit. Furthermore, Josephson STM investigates the tunneling of Cooper pairs between superconducting tips and superconducting samples [101]. For these experiments, the external magnetic field provides an additional tuning parameter. For example in Josephson STM, junctions with a nonzero phase shift in the ground state are of interest due to their high potential in applications [166]. The current-phase relation of such junctions is sensitive to an external magnetic field, which provides direct control over the phase shifts of the ground state [167]. In return, the ground state can experimentally be determined by measuring the critical current as a function of the magnetic field [167].

In general, spectroscopic measurements greatly benefit from clearly distinguishable spectral  $dI/dV$  features, which have been correlated with small opening angles ( $\alpha \ll \alpha_c$ ). So far, the presented V tips have been mechanically cut under tension with rather random results. Electroetching represents an alternative approach offering more control over the resulting tip apex and its opening angle. First attempts with oxalic acid as the electrolyte and the polycrystalline V wire as the anode have revealed promising results, indicating that the detailed shape of the tip can be controlled by the applied voltage [168]. Therefore, future STM experiments can significantly be improved by the use of superconducting tips with small opening angles. They result in less broadening ( $\Gamma \ll \Delta$ ) of the spectral features and the (first order) phase transition is shifted to higher critical fields ( $B_c \gg B_{c,\text{bulk}}$ ) in order to increase the range of applicable fields.

### 7.2 Probing Absolute Spin Polarization at the Nanoscale

The better understanding about superconductivity in the confined tip geometry has found direct application in a novel STM technique, which quantitatively probes the spin polarization at the nanoscale. Following the approach introduced by R. Meservey, P. M. Tedrow and P. Fulde for standard thin film sandwich tunnel junctions [7–9], the Zeeman split quasi-particle DOS of the superconducting V tips has been employed as a local probe for the spin polarization of tunneling electrons. The novel MTF-STM combines the virtues of the MTF technique and STM, such as the capability for quantitatively probing the spin polarization, the resolution and control on the atomic scale as well as the well-defined vacuum tunnel barrier. The latter considerably facilitates the interpretation of experimental results because the tunnel process

## 7.2. Probing Absolute Spin Polarization at the Nanoscale

---

is neither effected by the electronic properties of the barrier nor by the influence of structural defects. In comparison to conventional SP-STM, the spin polarization is probed on an absolute scale and the tunnel process does not have to take into account the spin-dependent electron orbitals of the tip. The capabilities of MTF-STM have been demonstrated when spatially resolving the local spin structure of a Co nanoisland with negative (-56 %) as well as positive spin polarizations (65 %), depending on the local position of the tunneling electrons. In comparison to DFT calculations, the measurements carried out by MTF-STM exceed the theoretical predictions by about a factor of two. This is attributed to the influence of the tunnel barrier as variations of the spin polarization up to 65 % were found when changing the tip-to-sample distance by only 2.3 Å. The observations have been modeled by a 1D model, which correlates the distance dependence of the spin polarization to a different decay of the spin-up and spin-down wave functions into vacuum. The described spin-filtering effect is universal for spin-dependent tunneling and, in general, effects the characteristics of most ferromagnetic tunnel junctions.

From a theoretical perspective, MTF-STM not only resolves the spin polarization on the atomic scale but also provides direct access to the fundamental processes of spin-dependent tunneling. Therefore, experimental observations obtained by the novel approach are highly suitable for a direct comparison to theory in order to verify and further develop existing physical models. For example, MTF-STM can be used to determine the spin-dependent tunnel matrix employed in theoretical descriptions of electron tunneling. To this end, the spin polarization of tunneling electrons can be spatially resolved as a function of distance for isolated atoms or molecules. To obtain insight into the role of the electronic orbitals, the study could include probing different charging states, which can be controlled for isolated atoms on insulating films.

For applications, MTF-STM represents a powerful probing technique for novel magnetic materials. Since the discovery of the TMR effect, great efforts have been directed towards improving the efficiency of the magnetic tunnel junctions in order to reach higher signals. On the pursuit for novel magnetic materials for the electrode, Heusler alloys represent promising candidates with theoretical predictions of high spin polarizations up to 100 % at the Fermi level. Their ferromagnetism is attributed to the double-exchange between magnetic ions, which are incorporated in a highly ordered structure with a well-defined stoichiometry. Heusler alloys have already been used in magnetic tunnel junctions [169], however, the experimentally observed spin polarizations have not yet reached the theoretical predictions. So far, spin polarizations of around 70 % have been obtained in low temperature measurements while the values have been even lower at room temperature [170–173]. The results also depend on the choice of material for the tunnel barrier. For example, in combination with MgO, the measured magnetoresistances have not significantly improved compared to the performance of conventional ferromagnetic electrodes [174]. The origin of the differences between theory and experiments remain unclear, but possible explanations include lower spin polarizations of the Heusler alloys, the influence of the tunnel barrier or varying properties of the tunnel junctions. Here, MTF-STM can quantitatively determine the spin polarization of Heusler

alloys free from disturbing effects arising from the tunnel junction fabrication. In addition, the atomic resolution provides direct insight into the correlation between structural properties and the resulting spin polarization of the tunneling electrons.

Besides the electrode material, the properties of the tunnel barrier itself also play an important role for increasing the spin polarization of tunneling electrons. For example, magnetic tunnel junctions, which are based on epitaxial MgO as the tunnel barrier have obtained large TMR effects attributed to symmetry filtering [116, 117, 137]. While the performance of a conventional magnetic tunnel junction is determined by the combined contributions from electrode and barrier, they can be analyzed separately by MTF-STM due to the vacuum tunnel barrier. In this context, MTF-STM can provide a complementary approach to TMR measurements on planar magnetic tunnel junctions. MTF-STM can directly reveal the spin polarization of the tunneling electrons in order to evaluate the efficiency of metal oxide barriers. The atomic resolution can address open questions concerning the participating electronic wave functions or the formation of localized states [144]. Additionally, studies based on MTF-STM can include a wide range of barrier materials ranging from pristine  $\text{Al}_2\text{O}_3$  to more complex spin filters such as EuS or EuO. Such spin-selective studies cannot only reveal fundamental aspects but help to systematically improve components for real devices.

In addition to the further development of existing devices, the atomic scale resolution of MTF-STM might also facilitate the introduction of novel spintronic applications. Next generation devices might use molecular or even atomic spin states for realizing logic operations as well as data storage. First experimental demonstrations have already employed spin-dependent tunneling on the molecular and on the atomic scale [118–121, 147]. For example, phenalenyl based molecules on a Co electrode have shown magnetoresistance effects up to 20% at room temperature [121]. At first sight, the observation is rather unexpected because the utilized zinc methyl phenalenyl molecules possess no net spin moment. A model based on *ab initio* calculations has suggested the formation of a hybridized molecular layer due to the interface spin transfer [121]. This interface layer with a large magnetic anisotropy serves as spin analyzer for the spin-polarized electrons of the Co electrode and, as a result, the tunnel magnetoresistance effects are observed. For such systems, studies carried out by MTF-STM can contribute to a better quantization of the spin-filtering capability as well as to a better understanding of the underlying hybridization and spin transfer effects. Providing atomic scale control, MTF-STM can also address the coupling between the spin centers of isolated zinc methyl phenalenyl molecules, which would allow the development of future quantum memories.

### 7.3 Probing Local Magnetic Moments Interacting with a Superconductor

In the last part of the thesis, the interaction of superconductivity and magnetism has been studied on the atomic scale. Contrary to magnetic fields, the magnetic moments of the isolated

### 7.3. Probing Local Magnetic Moments Interacting with a Superconductor

---

CuPc molecules only interact locally with the superconducting V(100) surface. As a result, bound states have been observed on the CuPc structure and in its close surroundings. Here, the superconducting STM tips play an important role due to their electronic structure, which effectively enhances the sensitivity to small features, such as the induced bound states. The extracted energies of the bound states as well as the absence of Kondo signals in the  $dI/dV$  measurements imply weak coupling for the magnetic moment of the CuPc molecule and the electrons of the superconducting V(100) sample. Furthermore, when spatially resolved, the spectral properties of the bound states appear strongly non-isotropic. This finding can be attributed to the anisotropic scattering potentials as well as to the non-uniform Fermi surface. In addition, the complex  $5 \times 1$  reconstruction of the V(100) surface might also effect the formation and spatial distribution of the bound states. On the V(100) surface in close vicinity to the CuPc molecule, the intensities of the bound states decay within the distance  $x \approx \pm 30 \text{ \AA}$  while simultaneously showing periodic oscillations. The behavior has been explained by a 1D model and the best agreement to the experimental data has been obtained by assuming two magnetic moments within the molecular structure. The 1D model also considers the influence of the non-uniform electronic structure by a phenomenological parameter. While this model only represents a simplified explanation, it describes the basic mechanisms of the experimental observations.

Future studies aim for a more detailed understanding of the superconducting phase as well as the spin state of the magnetic impurities. For example, impurity induced bound states can reveal the existence of multiple scattering channels in the Coulomb and the exchange interaction in order to obtain a better fundamental description [17]. For larger amounts of magnetic impurities on the superconducting surface, the formation of electronic bands from localized bound states represents another subject for future investigations. Theoretical calculations have even predicted the formation of broader bands with properties that significantly differ from conventional superconductors [175]. In theory, behavior similar to d-wave superconductors might be observed [175]. Furthermore, impurity induced bound states provide access to the fundamental properties of the superconducting state, such as the pairing mechanism. For unconventional superconductivity, mechanisms based on magnetic interactions have been proposed over the last few years [176, 177]. Here, the effects of isolated magnetic impurities on the local quasi-particle DOS can be probed by STM in order to reveal the basic physics of unconventional superconductivity [178]. In this context, the high energy resolution provided by superconducting tips at millikelvin temperatures can provide a better understanding of the quasi-particle scattering and the underlying mechanisms of the superconducting state.

In principle, quasi-particle excitations of quantum systems can also be engineered in order to have the same fundamental properties as Majorana fermions. First predicted by E. Majorana in 1937 [179], these Majorana fermions are their own anti-particles, which implies that they are free of electric charge. Since they obey non-abelian statistics, Majorana fermions are highly promising candidates for quantum computing due to their expected high coherence. Recently, strong evidence for the presence of Majorana fermions has been observed at the interface of ferromagnetic iron chains and superconducting lead by STM [180]. In such

## Chapter 7. Summary and Outlook

---

systems, Majorana quasi-particle bound states can arise either from a spatially ordered spin structure or from the combination of ferromagnetic exchange and spin orbit coupling. Similar effects might be observed on coupled magnetic moments incorporated in isolated molecules or even molecular networks on a superconducting surface. Future studies would require detecting zero-bias peaks in the  $dI/dV$  spectra, which have to be identified as Majorana quasi-particle excitations. For this purpose, the investigation has to demonstrate the coexistence of magnetism and superconductivity, for example by measuring the resulting bound states in the superconducting gap, as well as the existence of spin orbit coupling on the superconducting surface.

# Bibliography

- [1] L. N. Cooper, *Phys. Rev.* **104**, 1189 (1956).
- [2] J. Bardeen, L. N. Cooper and J. R. Schrieffer, *Phys. Rev.* **108**, 1175 (1957).
- [3] H. Fröhlich, *P. Roy. Soc. A: Math. Phy.* **215**, 291 (1952).
- [4] W. Meissner and R. Ochsenfeld, *Naturwissenschaften* **21**, 787 (1933).
- [5] F. London and H. London, *Proc. Roy. Soc.* **A149**, 71 (1935).
- [6] D. H. Douglass and R. Meservey, *Phys. Rev.* **135**, A19 (1964).
- [7] R. Meservey, P. M. Tedrow and P. Fulde, *Phys. Rev. Lett.* **25**, 1270 (1970).
- [8] P. M. Tedrow and R. Meservey, *Phys. Rev. Lett.* **26**, 192 (1971).
- [9] P. M. Tedrow and R. Meservey, *Phys. Rev. B* **7**, 318 (1973).
- [10] R. Meservey, *Phys. Scripta* **38**, 272 (1988).
- [11] A. V. Balatsky, I. Vekhter and J.-X. Zhu, *Rev. Mod. Phys.* **78**, 373 (2006).
- [12] M. I. Salkola, A. V. Balatsky and J. R. Schrieffer, *Phys. Rev. B* **55**, 12648 (1997).
- [13] M. E. Flatté and J. M. Byers, *Phys. Rev. Lett.* **78**, 3761 (1997).
- [14] C. P. Moca, E. Demler, B. Jankó and G. Zaránd, *Phys. Rev. B* **77**, 174516 (2008).
- [15] M. I. Salkola, A. V. Balatsky and D. J. Scalapino, *Phys. Rev. Lett.* **77**, 1841 (1996).
- [16] A. Yazdani, B. A. Jones, C. P. Lutz, M. F. Crommie and D. M. Eigler, *Science* **275**, 1767 (1997).
- [17] S.-H. Ji *et al.*, *Phys. Rev. Lett.* **100**, 226801 (2008).
- [18] K. J. Franke, G. Schulze and J. I. Pascual, *Science* **332**, 940 (2011).
- [19] H. K. Onnes, *Leiden Comm.* **120b**, **122b**, **124c** (1911).
- [20] H. K. Onnes, *Leiden Comm.* **108** (1908).

## Bibliography

---

- [21] H. Ibach and H. Lüth, *Festkörperphysik*, Springer Berlin Heidelberg (2009).
- [22] M. Tinkham, *Introduction to Superconductivity*, Dover Publications (2004).
- [23] C. P. Poole, H. A. Farach, R. J. Creswick and R. Prozorov, *Superconductivity*, Academic Press (2007).
- [24] W. Nolting, *Grundkurs Theoretische Physik 4: Spezielle Relativitätstheorie, Thermodynamik*, Springer (2005).
- [25] C. P. Poole, *Handbook of Superconductivity*, Academic Press (2000).
- [26] S. T. Sekula and R. H. Kernohan, *Phys. Rev. B* **5**, 904 (1972).
- [27] A. Schilling, M. Cantoni, J. D. Guo and H. R. Ott, *Nature* **363**, 56 (1993).
- [28] A. M. Cucolo *et al.*, *J. Low Temp. Phys.* **50**, Nos. 3/4 (1983).
- [29] R. Radebaugh and P. H. Keesom, *Phys. Rev.* **149**, 209 (1966).
- [30] C. Kittel, *Introduction to Solid State Physics*, Wiley (1996).
- [31] V. L. Ginzburg and L. D. Landau, *J. Exp. Theor. Phys.* **20**, 1064 (1950).
- [32] L. P. Gor'kov, *J. Exp. Theor. Phys.* **9**, 1364 (1959).
- [33] L. V. Shubnikov, V. I. Khotkevich, Y. D. Shepelev and Y. N. Ryabinin, *J. Exp. Theor. Phys.* **7**, 221 (1937).
- [34] H. F. Hess, R. B. Robinson, R. C. Dynes, J. M. Valles and J. V. Waszczak, *Phys. Rev. Lett.* **62**, 214 (1989).
- [35] H. F. Hess, R. B. Robinson and J. V. Waszczak, *Phys. Rev. Lett.* **64**, 2711 (1990).
- [36] J. Bardeen and M. J. Stephen, *Phys. Rev.* **140**, A1197 (1965).
- [37] L. D. Landau and E. M. Lifshitz, *Statistical Physics*, Oxford: Butterworth-Heinemann (1980).
- [38] L. I. Klushin and A. M. Skvortsov, *J. Phys. A: Math. Theor.* **44**, 473001 (2011).
- [39] R. Meservey and D. H. Douglass, *Phys. Rev.* **135**, A24 (1964).
- [40] I. Giaever and K. Megerle, *Phys. Rev.* **122**, 1101 (1961).
- [41] P. Townsend and J. Sutton, *Phys. Rev.* **128**, 591 (1962).
- [42] P. S. Deo, V. A. Schweigert, F. M. Peeters and A. K. Geim, *Phys. Rev. Lett.* **79**, 4653 (1997).
- [43] A. Kanda, B. J. Baelus, F. M. Peeters, K. Kadowaki and Y. Ootuka, *Phys. Rev. Lett.* **93**, 257002 (2004).



- 
- [44] R. Benoist and W. Zwerger, *Z. Phys. B* **103**, 377 (1997).
- [45] G.-Q. Zha, S.-P. Zhou, B.-H. Zhu, Y.-M. Shi and H.-W. Zhao, *Phys. Rev. B* **74**, 024527 (2006).
- [46] B. J. Baelus, D. Sun and F. M. Peeters, *Phys. Rev. B* **75**, 174523 (2007).
- [47] D. H. Douglass, *Phys. Rev.* **132**, 513 (1963).
- [48] K. Maki, *Prog. Theor. Phys.* **32**, 29 (1964).
- [49] P. Fulde and K. Maki, *Phys. Rev.* **141**, 275 (1966).
- [50] A. A. Abrikosov and L. P. Gor'kov, *J. Exp. Theor. Phys.* **42**, 1088 (1962).
- [51] K. Maki and P. Fulde, *Phys. Rev.* **140**, A1586 (1965).
- [52] R. Meservey, P. M. Tedrow and R. C. Bruno, *Phys. Rev. B* **11**, 4224 (1975).
- [53] P. Fulde, *Tunneling in Solids*, Plenum (1969).
- [54] D. C. Worledge and T. H. Geballe, *Phys. Rev. B* **62**, 447 (2000).
- [55] J. A. X. Alexander, T. P. Orlando, D. Rainer and P. M. Tedrow, *Phys. Rev. B* **31**, 5811 (1985).
- [56] G. Eilenberger, *Z. Phys.* **214**, 195 (1968).
- [57] J. B. Ketterson and S. N. Song, *Superconductivity*, Cambridge University Press (1999).
- [58] K. D. Usadel, *Phys. Rev. Lett.* **25**, 507 (1970).
- [59] D. A. Ivanov, Y. V. Fominov, M. A. Skvortsov and P. M. Ostrovsky, *Phys. Rev. B* **80**, 134501 (2009).
- [60] A. Einstein and W. J. de Haas, *Verh. d. deut. phys. G.* **17**, 152 (1915).
- [61] S. A. Wolf *et al.*, *Science* **294**, 1488 (2001).
- [62] M. N. Baibich *et al.*, *Phys. Rev. Lett.* **61**, 2472 (1988).
- [63] G. Binasch, P. Grünberg, F. Saurenbach and W. Zinn, *Phys. Rev. B* **39**, 4828 (1989).
- [64] M. Jullière, *Phys. Lett. A* **54**, 225 (1975).
- [65] J. S. Moodera, L. R. Kinder, T. M. Wong and R. Meservey, *Phys. Rev. Lett.* **74**, 3273 (1995).
- [66] T. Miyazaki and N. Tezuka, *J. Magn. Magn. Mater.* **139**, L231 (1995).
- [67] S. Blundell, *Magnetism In Condensed Matter*, Oxford University Press (2000).
- [68] S. Maekawa and T. Shinjo, *Spin Dependent Transport in Magnetic Nanostructures*, CRC press (2000).

## Bibliography

---

- [69] W. Nolting, *Grundkurs theoretische Physik. Bd.5: Quantenmechanik*, Springer (2004).
- [70] S. Brodsky *et al.*, *Nucl. Phys. B* **703**, 333 (2004).
- [71] B. Odom, D. Hanneke, B. D'Urso and G. Gabrielse, *Phys. Rev. Lett.* **97**, 030801 (2006).
- [72] L. Yu, *Acta Phys. Sin.* **21**, 75 (1965).
- [73] H. Shiba, *Prog. Theor. Phys.* **40**, 435 (1968).
- [74] A. I. Rusinov, *J. Exp. Theor. Phys.* **9**, 85 (1969).
- [75] A. V. Balatsky, M. I. Salkola and A. Rosengren, *Phys. Rev. B* **51**, 15547 (1995).
- [76] G. Binnig, H. Rohrer, C. Gerber and E. Weibel, *Appl. Phys. Lett.* **40**, 178 (1982).
- [77] G. Binnig, H. Rohrer, C. Gerber and E. Weibel, *Phys. Rev. Lett.* **49**, 57 (1982).
- [78] G. Binnig, H. Rohrer, C. Gerber and E. Weibel, *Phys. Rev. Lett.* **50**, 120 (1983).
- [79] J. Bardeen, *Phys. Rev. Lett.* **6**, 57 (1961).
- [80] J. Tersoff and D. R. Hamann, *Phys. Rev. Lett.* **50**, 1998 (1983).
- [81] J. Tersoff and D. R. Hamann, *Phys. Rev. B* **31**, 805 (1985).
- [82] F. Schwabl, *Quantenmechanik*, Springer (2005).
- [83] L. J. Lauhon and W. Ho, *Rev. Sci. Instrum.* **72**, 216 (2001).
- [84] J. Lambe and R. C. Jaklevic, *Phys. Rev.* **165**, 821 (1968).
- [85] M. Assig, *Development of a Millikelvin Scanning Tunneling Microscope for Application in Ultra High Vacuum and High Magnetic Fields*, PhD Thesis EPFL (2011).
- [86] M. Assig *et al.*, *Rev. Sci. Instrum.* **84**, 033903 (2013).
- [87] C. R. Ast, M. Assig, A. Ast and K. Kern, *Rev. Sci. Instrum.* **79**, 093704 (2008).
- [88] E. Pobell, *Matter and Methods at Low Temperature*, Springer (2007).
- [89] R. Meservey and P. M. Tedrow, *Phys. Rep.* **238**, 173 (1994).
- [90] H. Engler and P. Fulde, *Z. Phys.* **247**, 1 (1971).
- [91] P. Fulde, *Adv. Phys.* **22**, 667 (1973).
- [92] R. C. Bruno and B. B. Schwartz, *Phys. Rev. B* **8**, 3161 (1973).
- [93] R. Meservey, D. Paraskevopoulos and P. M. Tedrow, *Phys. Rev. B* **22**, 1331 (1980).
- [94] D. N. Langenberg, *Proc. 14th Int. Conf. Low Temp. Phys.*, North-Holland (1975).

- 
- [95] R. C. Dynes, V. Narayanamurti and J. P. Garno, *Phys. Rev. Lett.* **41**, 1509 (1978).
- [96] I. Brihuega *et al.*, *Phys. Rev. B* **84**, 104525 (2011).
- [97] M. Eltschka *et al.*, *Nano Letters* **14**, 7171 (2014).
- [98] M. Eltschka *et al.*, *Appl. Phys. Lett.* in press (2015).
- [99] S. H. Pan, E. W. Hudson and J. C. Davis, *Appl. Phys. Lett.* **73**, 2992 (1998).
- [100] A. Kohen *et al.*, *Phys. Rev. Lett.* **97**, 027001 (2006).
- [101] B. Jäck *et al.*, *Appl. Phys. Lett.* **106**, 013109 (2015).
- [102] Y. Chen, M. M. Doria and F. M. Peeters, *Phys. Rev. B* **77**, 054511 (2008).
- [103] V. Kresin and Y. Ovchinnikov, *Phys. Rev. B* **74**, 024514 (2006).
- [104] A. García-García, J. Urbina, E. Yuzbashyan, K. Richter and B. Altshuler, *Phys. Rev. Lett.* **100**, 187001 (2008).
- [105] H. Olofsson, S. Åberg and P. Leboeuf, *Phys. Rev. Lett.* **100**, 037005 (2008).
- [106] S. Bose *et al.*, *Nature Mater.* **9**, 550 (2010).
- [107] W. L. McMillan, *Phys. Rev.* **167**, 331 (1968).
- [108] T. T. Chen, J. T. Chen, J. D. Leslie and H. J. T. Smith, *Phys. Rev. Lett.* **22**, 526 (1969).
- [109] M. Strongin, R. S. Thompson, O. F. Kammerer and J. E. Crow, *Phys. Rev. B* **1**, 1078 (1970).
- [110] G. A. Gibson and R. Meservey, *Phys. Rev. B* **40**, 8705 (1989).
- [111] *MATLAB R2014b The MathWorks, Inc.*
- [112] O. Naaman, W. Teizer and R. C. Dynes, *Phys. Rev. Lett.* **87**, 097004 (2001).
- [113] H. Kimura, R. P. Barber, S. Ono, Y. Ando and R. C. Dynes, *Phys. Rev. Lett.* **101**, 037002 (2008).
- [114] M. Kroner *et al.*, *Phys. Rev. Lett.* **100**, 156803 (2008).
- [115] A. V. Balatsky, M. Nishijima and Y. Manassen, *Adv. Phys.* **61**, 117 (2012).
- [116] S. S. P. Parkin *et al.*, *Nature Mater.* **3**, 862 (2004).
- [117] S. Yuasa, T. Nagahama, A. Fukushima, Y. Suzuki and K. Ando, *Nature Mater.* **3**, 868 (2004).
- [118] C. F. Hirjibehedin, C. P. Lutz and A. J. Heinrich, *Science* **312**, 1021 (2006).
- [119] A. A. Khajetoorians, J. Wiebe, B. Chilian and R. Wiesendanger, *Science* **332**, 1062 (2011).
- [120] T. Miyamachi *et al.*, *Nature* **503**, 242 (2013).

## Bibliography

---

- [121] K. V. Raman *et al.*, *Nature* **493**, 509 (2013).
- [122] R. Wiesendanger, *Rev. Mod. Phys.* **81**, 1495 (2009).
- [123] L. Diekhöner *et al.*, *Phys. Rev. Lett.* **90**, 236801 (2003).
- [124] O. Pietzsch, A. Kubetzka, M. Bode and R. Wiesendanger, *Phys. Rev. Lett.* **92**, 057202 (2004).
- [125] O. Pietzsch *et al.*, *Phys. Rev. Lett.* **96**, 237203 (2006).
- [126] L. Niebergall, V. S. Stepanyuk, J. Berakdar and P. Bruno, *Phys. Rev. Lett.* **96**, 127204 (2006).
- [127] H. Oka *et al.*, *Science* **327**, 843 (2010).
- [128] H. Oka *et al.*, *Phys. Rev. Lett.* **107**, 187201 (2011).
- [129] U. Gradmann and J. Müller, *Z. Angew. Phys.* **30**, 87 (1970).
- [130] M. T. Kief and W. F. Egelhoff, *Phys. Rev. B* **47**, 10785 (1993).
- [131] C. Rath, J. E. Prieto, S. Müller, R. Miranda and K. Heinz, *Phys. Rev. B* **55**, 10791 (1997).
- [132] P. Tedrow and R. Meservey, *Phys. Lett. A* **69**, 285 (1978).
- [133] J. S. Moodera, X. Hao, G. A. Gibson and R. Meservey, *Phys. Rev. Lett.* **61**, 637 (1988).
- [134] X. Hao, J. S. Moodera and R. Meservey, *Phys. Rev. B* **42**, 8235 (1990).
- [135] S. F. Alvarado, *Phys. Rev. Lett.* **75**, 513 (1995).
- [136] M. Münzenberg and J. S. Moodera, *Phys. Rev. B* **70**, 060402 (2004).
- [137] W. H. Butler, X.-G. Zhang, T. C. Schulthess and J. M. MacLaren, *Phys. Rev. B* **63**, 054416 (2001).
- [138] S. G. Davison and M. Steslicka, *Basic Theory of Surface States*, Clarendon Press (1996).
- [139] P. A. Tipler and R. A. Llewellyn, *Modern Physics*, W.H. Freeman (1999).
- [140] P. Ignatiev, *Theoretical study of spin-polarized surface states on metal surfaces*, Ph.D. thesis (2009).
- [141] J. C. Slonczewski, *Phys. Rev. B* **39**, 6995 (1989).
- [142] J. K. Gimzewski and R. Möller, *Phys. Rev. B* **36**, 1284 (1987).
- [143] H. F. Ding, W. Wulfhekkel, U. Schlickum and J. Kirschner, *Europhys. Lett.* **63**, 419 (2003).
- [144] K. Wang, P. M. Levy, S. Zhang and L. Szunyogh, *Philos. Mag.* **83**, 1255 (2003).
- [145] J. C. Slater, *Phys. Rev.* **36**, 57 (1930).

- 
- [146] E. Clementi and D. L. Raimondi, *J. Chem. Phys.* **38**, 2686 (1963).
- [147] C. Strunk, *Science* **306**, 63 (2004).
- [148] A. Burtzloff, A. Weismann, M. Brandbyge and R. Berndt, *Phys. Rev. Lett.* **114**, 016602 (2015).
- [149] R. J. Soulen *et al.*, *Science* **282**, 85 (1998).
- [150] S. F. Alvarado and P. Renaud, *Phys. Rev. Lett.* **68**, 1387 (1992).
- [151] K. von Bergmann, M. Ternes, S. Loth, C. P. Lutz and A. J. Heinrich, *Phys. Rev. Lett.* **114**, 076601 (2015).
- [152] W. Wulfhekel and J. Kirschner, *Appl. Phys. Lett.* **75**, 1944 (1999).
- [153] T. Martin and R. Landauer, *Phys. Rev. B* **45**, 1742 (1992).
- [154] M. A. Woolf and F. Reif, *Phys. Rev.* **137**, A557 (1965).
- [155] J. C. Phillips, *Phys. Rev. Lett.* **10**, 96 (1963).
- [156] A. J. Heinrich, J. A. Gupta, C. P. Lutz and D. M. Eigler, *Science* **306**, 466 (2004).
- [157] S. Loth, C. P. Lutz and A. J. Heinrich, *New J. Phys.* **12**, 125021 (2010).
- [158] C. Isvoranu *et al.*, *J. Chem. Phys.* **131**, 214709 (2009).
- [159] R. Koller *et al.*, *Surface Science* **480**, 11 (2001).
- [160] M. Kralj *et al.*, *Surface Science* **526**, 166 (2003).
- [161] P. H. Lippel, R. J. Wilson, M. D. Miller, C. Wöll and S. Chiang, *Phys. Rev. Lett.* **62**, 171 (1989).
- [162] M. Kuzmin, A. Kumar, B. Poelsema and H. J. W. Zandvliet, *The Journal of Chemical Physics* **138**, 114302 (2013).
- [163] A. Mugarza *et al.*, *Phys. Rev. B* **85**, 155437 (2012).
- [164] S. Stepanow *et al.*, *Phys. Rev. B* **82**, 014405 (2010).
- [165] R. D. Parker and M. H. Halloran, *Phys. Rev. B* **9**, 4130 (1974).
- [166] T. Ortlepp *et al.*, *Science* **312**, 1495 (2006).
- [167] E. Goldobin, D. Koelle, R. Kleiner and R. G. Mints, *Phys. Rev. Lett.* **107**, 227001 (2011).
- [168] A. Topp, *in preparation*, Master's thesis (2015).
- [169] W. Wang *et al.*, *Phys. Rev. B* **81**, 140402 (2010).

## Bibliography

---

- [170] S. Kämmerer, A. Thomas, A. Hütten, A. tten and G. Reiss, *Appl. Phys. Lett.* **85**, 79 (2004).
- [171] D. Ebke *et al.*, *Appl. Phys. Lett.* **89**, 162506 (2006).
- [172] Y. Sakuraba *et al.*, *Appl. Phys. Lett.* **88**, 192508 (2006).
- [173] J. Schmalhorst *et al.*, *Phys. Rev. B* **75**, 014403 (2007).
- [174] H.-x. Liu *et al.*, *Appl. Phys. Lett.* **101**, 132418 (2012).
- [175] L. S. Borkowski, *Phys. Status Solidi B* **250**, 615 (2013).
- [176] P. Monthoux, A. V. Balatsky and D. Pines, *Phys. Rev. B* **46**, 14803 (1992).
- [177] T. Moriya, Y. Takahashi and K. Ueda, *J. Phys. Soc. Jpn.* **59**, 2905 (1990).
- [178] E. W. Hudson *et al.*, *Nature* **411**, 920 (2001).
- [179] E. Majorana, *Nuovo Cimento* **14**, 171 (1937).
- [180] S. Nadj-Perge *et al.*, *Science* **346**, 602 (2014).

# Curriculum Vitae

Name: Matthias Eltschka  
Date of Birth: September 6, 1984  
Place of Birth: Freiburg, Germany  
Nationality: German

- 2011–2015     **Doctoral Studies**  
Doctoral School of Physics at  
École Polytechnique Fédérale de Lausanne, Switzerland  
Research associate in the group of Prof. Kern at  
Max Planck Institute for Solid State Research, Stuttgart, Germany
- 2011           **Research Stay**  
in the group of Dr. Moodera at  
Massachusetts Institute of Technology, USA
- 2004–2010    **Diploma Studies**  
Diploma in Physics  
at University of Konstanz, Germany
- 2009–2010    **Diploma Thesis**  
“Spin Dynamics at Finite Temperatures: Theory and Experiment“  
in the groups of Prof. Kläui and Prof. Nowak  
at University of Konstanz, Germany
- 2007           **Research Stay**  
in the group of Dr. Dunin-Borkowski  
University of Cambridge, UK
- 1995–2004    **Gymnasium (Secondary School)**  
Theodor-Heuss-Gymnasium in Freiburg, Germany

## Curriculum Vitae

---

1991–1995      **Grundschule (Primary School)**  
Schneeburgschule in Freiburg, Germany



## List of Publications

- **M. Eltschka**, M. Kläui, U. Rüdiger, T. Kasama, L. Cervera-Gontard, R. E. Dunin-Borkowski, F. Luo, L. J. Heyderman, C.-J. Jia, L.-D. Sun, and C.-H. Yan, “Correlation between magnetic spin structure and the three-dimensional geometry in chemically synthesized nanoscale magnetite rings”, *Appl. Phys. Lett.* **92**, 222508 (2008).
- C.-J. Jia, L.-D. Sun, F. Luo, X.-D. Han, L. J. Heyderman, Z.-G. Yan, C.-H. Yan, K. Zheng, Z. Zhang, M. Takano, N. Hayashi, **M. Eltschka**, M. Kläui, U. Rüdiger, T. Kasama, L. Cervera-Gontard, R. E. Dunin-Borkowski, G. Tzvetkov, and Jörg Raabe, “Large-Scale Synthesis of Single-Crystalline Iron Oxide Magnetic Nanorings” *J. Am. Chem. Soc.* **130**, 16968 (2008).
- **M. Eltschka**, M. Wötzel, J. Rhensius, S. Krzyk, U. Nowak, M. Kläui, T. Kasama, R. E. Dunin-Borkowski, L. J. Heyderman, H. J. van Driel, and R. A. Duine, “Nonadiabatic Spin Torque Investigated Using Thermally Activated Magnetic Domain Wall Dynamics” *Phys. Rev. Lett.* **105**, 056601 (2010).
- **M. Eltschka**, B. Jäck, M. Assig, O. V. Kondrashov, M. A. Skvortsov, M. Etzkorn, C. R. Ast, and K. Kern, “Probing Absolute Spin Polarization at the Nanoscale”, *Nano Lett.* **14**, 7171 (2014).
- B. Jäck, **M. Eltschka**, M. Assig, A. Hardock, M. Etzkorn, C. R. Ast, and K. Kern, “A nanoscale gigahertz source realized with Josephson scanning tunneling microscopy”, *Appl. Phys. Lett.* **106**, 013109 (2015).
- **M. Eltschka**, B. Jäck, M. Assig, O. V. Kondrashov, M. A. Skvortsov, M. Etzkorn, C. R. Ast, and K. Kern, “Superconducting STM tips in a magnetic field: geometry-controlled order of the phase transition”, *Appl. Phys. Lett.* in press (2015).
- B. Jäck, **M. Eltschka**, M. Assig, M. Etzkorn, C. R. Ast, and K. Kern, “Critical Josephson current in the dynamical Coulomb blockade regime”, *in preparation*.
- B. Jäck, J. Senkpiel, **M. Eltschka**, M. Etzkorn, C. R. Ast, and K. Kern, “Quasiparticle dissipation phenomena in Josephson junctions”, *in preparation*.